

Geoscience Laser Altimeter System (GLAS)

Algorithm Theoretical Basis Document
Version 5.0

Derivation of Range and Range Distributions From Laser Pulse Waveform Analysis for Surface Elevations, Roughness, Slope, and Vegetation Heights

Prepared by:

Anita C. Brenner⁹, H. Jay Zwally¹, Charles R. Bentley², Bea M. Csathó⁴, David J. Harding¹,
Michelle A. Hofton⁷, Jean-Bernard Minster⁵, LeeAnne Roberts³, Jack L. Saba⁸, Robert H.
Thomas⁶, Donghui Yi³

¹NASA Goddard Space Flight Center

²University of Wisconsin

³SGT, Inc/NASA Goddard Space Flight Center

⁴University at Buffalo

⁵University of California at San Diego

⁶EG&G/Wallops Flight Facility

⁷University of Maryland at College Park

⁸SSAI/Goddard Space Flight Center

⁹Sigma Space Corps

November 2011

i. *Changes from version 1.0 to 1.1*

- sec 3.1.2.1 Figure 1 replaced for clarity
- Section 3.1.2.2.5 last sentence replace) E with RMS wave height
- Section 4.1.1 – table 4.1 changes: `ngt_noise` added, `ref_range` removed, `filterwdmin` & `filterwdmax` moved from “Numerical Program Parameters” to “Instrument Parameters”
- Section 4.1.3.2

OLD:

Assuming gate 1 is farthest from the satellite, this is the time t such that $Wf(t) < \text{Noise_ob} + \text{Nsig} * \sigma_{\text{noise_ob}} < Wf(t+1)$. Given this t ,

NEW:

Assuming gate 1 is farthest from the satellite, this is the time $t(i)$ such that $Wf(t(i)) < \text{Noise_ob} + \text{Nsig} * \sigma_{\text{noise_ob}}$ for all $i' \leq i$
 $Wf(t(i+1)) > \text{Noise_ob} + \text{Nsig} * \sigma_{\text{noise_ob}}$
where i is the gate number.

- Equation changed in section 4.1.3.2 from “ $WF_range_cor_std = t * \Delta T_hires * c$ ” to “ $WF_range_cor_std = t * c/2$ ”
- Text changed in 4.1.3.4 from “the time it takes to travel to and from the ground using `Range_std`” to “the time it takes to travel to the ground using `Range_std`”
- Equation changed in section 4.1.3.4 from “ $\text{Time_gb}(i) = \text{GPSshotTime}(i) * \text{Range_std} * 2/c$ ” to “ $\text{Time_gb}(i) = \text{GPSshotTime}(i) + \text{Range_std} / c$ ”
- Section 4.1.3.7

IF `Psattm > Psat_spec` and `Psattm < Psat_stop` THEN

replaced with

`Psattm ≥ Psat_spec` and `Psattm < Psat_stop` THEN

IF `Psattm > Psat_stop` processing, SET `Flag_sat=2`

replaced with

IF `Psattm ≥ Psat_stop` processing, SET `Flag_sat=2`

IF `Psattm > 0` and `Psattm < Psat_stop`, SET `Flag_sat=1`

Replaced with

IF `Psattm > 0` and `Psattm < Psat_spec`, SET `Flag_sat=1`

- Section 4.1.3.8 Noise calculation changed
- Section 4.2 replaced
- Section 4.3.3.2 Figure 6 changed for clarity
- Section 4.3.3.2 Figure 8 reference changed to Figure 7. Figure 7 shrunk so caption fits on same page
- Section 4.3.4.2 moved 3rd bullet to after definitions for 2nd bullet
- Section 4.3.4.3 modified words of 2nd bullet

- Chapter 5 tables labeled with correct numbers and more meaningful titles, table 5.5 removed since same as 5.3
- Table 5.1 items 2, 3, 11, and 12, changed descriptions and units
- Chapter 5 sea ice and ocean output parameters put into tables instead of lists
- Added paragraph above table 5-7“‘Ocean’ data will be as determined from the global DEM, to include all regions larger than, say 1000 sq km that are at sea level. Thus, ‘ocean’ tracking will be implemented over large lakes and over sea ice, in addition to the special tracking appropriate to these areas.”

ii. *Changes from version 1.1 to 2.0*

Sec 1

- added Figure 1

Sec 2

- Added discussion of how instrument algorithm design (sec 2.7) meets the science requirements

Sec 3

- Added statement that Gaussian return is assumed for elevation algorithms
- Added section 3.1.2.3 on skewness and kurtosis

Sec 4

- Minor changes added to make the algorithms work in an operational environment
- Added figures from ATBD for clarity
- Standard range changed to preliminary range
- Threshold retracker added
- Quantitative results presented showing elevation, roughness, and slope errors expected over ice sheets

Sec 5

- Added geolocation information to level 1a waveform product
- Added discussion on product granule size distribution and archiving
- Added figures from oral ATBD presentation for clarity

iii. *Changes from version 2.0 to 3.0*

- In section 2.1, paragraph three, changed the last sentence from "There are no ice shelves around Greenland" to "There are few ice shelves in Greenland".
- In section 2.6, paragraph five (A small footprint ...), replaced entire paragraph as per Robert Thomas.
- In section 2.7, in the last paragraph changed "used solely to determine where the start of the raw digitized data" to "used solely to determine where the start of the received waveform digitized data", and changed "The data to be sent to the ground are obtained directly from the raw digitizer waveform" to "The data to be sent to the ground are obtained directly from the received digitizer waveform".
- In section 3.1.2.2.5, replaced old paragraphs 2 through 5 with new paragraphs 2 through 4 as per Robert Thomas.
- In section 3.2.2, last paragraph, remove items 1 & 2 regarding Var_mult & Var_check.
- In section 4.0, Outline Of Procedure, changed "Characterize raw" to "Characterize received".
- In section 4.1.1, removed Var_mult & Var_check from Table 4-1 and added minAmpPcnt, sigmaMinInit, minIter, minGatesNs, minNoise, and min4sat.
- In section 4.1.1.1, Table 4-2, removed Psattm, and changed "The waveform in raw units" to "The received waveform".
- In section 4.1.3.1, changed the formula for the normalized time array.
- In section 4.1.3.10, Loop Begin, second sentence, changed "the smooth value will equal the raw value" to "the smooth value will equal the received value".
- In section 4.3.2.1, after Figure 8, fourth sentence, changed "centroid of the raw waveform" to "centroid of the received waveform".
- In section 4.3.2.1, after Figure 9, first sentence, changed "centroid of the raw return" to "centroid of the received return".
- In section 4.3.3.1, third bullet, first sub-bullet, changed "centroid of the raw waveform" to "centroid of the received waveform".
- In section 4.3.3.1, third bullet, third sub-bullet, changed "fit to the raw waveform" to "fit to the received waveform".
- In section 4.3.3.1, fourth bullet, second sub-bullet, changed "fit to the raw waveform" to "fit to the received waveform".
- In section 4.3.3.1, fourth bullet, fourth sub-bullet, changed "centroid of the smoothed waveform" to "centroid of the received waveform".
- In section 4.3.3.1, fourth bullet, added the following sub-bullets and text:
 - The number of peaks in the gaussian fit
 - The maximum smoothed amplitude
 - The reflectance
 - A forward-scattering parameter TBD

For the same 100km strips (adjustable), the number of problem flags will be calculated and displayed, and the map will be marked if the surface ID (land, ocean, ice sheet, sea ice) has changed.

- In section 4.3.3.2, changed " T_c = time delay of the centroid of the raw" to " T_c = time delay of the centroid of the received".
- In section 4.3.8, replaced Psattm with Psat, and added algorithm for computing saturation.
- Replaced Figure 5 with new Figures 5 and 6. Changed reference numbers for figures 6 through 17 to 7 through 18.

- In section 5.1, table 5-1, items 16, 17, 27, and 28, changed "raw" to "received".
- In section 5.1, table 5-1, item 22, changed "as offset from first telemetered gate" to "as offset from last telemetered gate".
- In section 5.1, table 5-1, items 35 and 36, changed "raw" to "transmitted".
- In section 5.2.3, changed "The equation to scale the received energy to account for the range is TBD." to "The equation for the surface reflectivity is:", added formulas 37, and 38 for reflectance from instrument team, and added formulas 39, 40, and 41, and a procedure for determining transmitted and received energy.
- In the first paragraph in section 5.5, changed "These algorithms will be applied both to the full set of stored Gaussian fits and also to the Gaussian fit to the last (lowest) peak" to "These algorithms will be applied to the Gaussian fit to the last (lowest) peak".
- In section 5.2.5, the source for the 1 km resolution land DEM to be used for ICESat data processing is Global 30 Arc-Second Elevation Data Set (GTOPO30).
- In section 5.5, removed "Surface Roughness from Ice sheet algorithms using all fits" and "Surface slope from ice sheet algorithms using all fit" from Table 5-6.
- In section 5.2.6, Table 5-2, changed "centroid of raw" to "centroid of received".
- In Table 5-2, & Table 5-4, changed "Reflectance" to "Reflectance * round trip atmospheric transmission".
- In section 5.3, second paragraph, ninth sentence, changed "of the raw waveform" to "of the received waveform".
- In section 5.3, table 5-4, changed "Standard deviation of raw" to "Standard deviation of received", "Kurtosis of the raw" to "Kurtosis of the received", "Skewness of the raw" to "Skewness of the received", and "Range increment from reference range to centroid of raw waveform" to "Range increment from reference range to centroid of received waveform".
- In section 5.4, table 5-5, changed "Average elevation of all surfaces in the footprint from the centroid of the raw" to "Average elevation of all surfaces in the footprint from the centroid of the received", "Standard deviation of raw" to "Standard deviation of received", "Skewness of the raw return" to "Skewness of the received waveform", and "Range increment from reference range to centroid of raw" to "Range increment from reference range to centroid of received".
- 5.4.1, item a, changed "Sea-ice mask, possibly based on daily sea-ice extent charts from the National Ice Center" to "Sea-ice mask, defined from the GSFC SMMR-SSM/I ice concentration data".
- In section 5.5, first paragraph, second sentence, changed "the centroid of the smoothed" to "the centroid of the received".
- In section 5.5, table 5-6, changed "Standard deviation of raw waveform using all fits" to "Standard deviation of received waveform using all fits", "Standard deviation of raw waveform using stored fits" to "Standard deviation of received waveform using stored fits", and "Skewness of the smoothed waveform" to "Skewness of the received waveform from signal begin to signal end".
- In section 5.6, table 5-7, changed "Standard deviation of raw" to "Standard deviation of received", and "Range increment from reference range to centroid of the raw" to "Range increment from reference range to centroid of the received", "Skewness of the smoothed return" to "Skewness of the received waveform from signal begin to signal end", and "Ocean surface elevation calculated using the centroid of the last peak in the waveform" to "Ocean surface elevation calculated using the centroid of the waveform".
- In section 6.1.3, fifth paragraph, item 4), changed "centroid of the raw" to "centroid of the received".
- Added references Krabill et al., (1995) and Krabill et al., (2000).
- Corrected reference Zwally et al., (1983) to include R.H. Thomas.

iv. *Changes from version 3.0 to 4.0*

- Renumbered equations.
- Updated figures 3, 4, 17, and 18.
- Made various spelling, style, and grammar changes.
- Corrected sections 3.1.1.1, and 3.1.2.2.
- In section 4.1.2, added “Standard deviation of fit” to list.
- Added section 4.1.3.2, Calibrate the Waveform.
- Updated Equation 46.
- Updated section 4.1.3.9, Check Saturation.
- Added table 4-3, Saturation Flag Criteria.
- Updated section 4.1.3.13.1, Make An Initial Estimate For The Unknown Model Parameters.
- Updated section 4.1.3.13.2, Perform The Nonlinear Least-Squares Fit.
- Numbered and updated table 4-4, Waveform Assessment Parameters.
- Updated section 4.1.3.16, Calculate a threshold retracker correction.
- Updated table 4-5, Output parameters from the waveform characterization process.
- Updated section 4.3.2.5, Validation During The 90 Day Cal/Val Period.
- Changed last peak to maximum amplitude peak in sections 4.3.3.1., 4.3.3.2., 5.2.1., 5.2.2., 5.2.6., 5.3., 5.4., 5.6.
- Updated table 5-1, Parameters required to calculate physical properties of the surface for level 1b waveform product.
- Updated section 5.2.3, Calculation of Reflectance.
- Updated table 5-2, Parameters to be output every measurement –level 1b elevation product.
- Updated table 5-4, Parameters to be output every measurement-level 2 ice sheet product.
- Updated section 5.5, Level 2 Land Product – GLA14.
- Updated section 6.2, Instrument Effects.

v. *Changes from version 4.0 to 4.1*

- Style corrections.
- The estimated gaussian width for the maximum amplitude peak is selected in the same way for both standard and alternate parameterizations (see section 4.1.3.13.1).

vi. *Changes from version 4.1 to 4.2*

- Added section 5.2.5., Calculation of Geoid.

vii. *Changes from version 4.2 to 4.3*

- Added section 3.2.3., Development of Equations For Area Conserving Special Processing.
- In section 3.2.3., added equations 38 & 39, and renumbered the subsequent equations.
- In Table 4-1, anc07 parameters that are used to determine saturation have been made laser dependent.
- Sections 4.1.3.13.4., Special Processing For Saturated Waveforms, and 4.1.3.13.4.1, Area Conserving Special Processing were added.
- Added appendix 1, Gaussian Fit to Saturated Waveform I: Matching Area and Leading Edge.

viii. Changes from 4.3 to 4.4

- In section 3.2. 2, changed "The incremental change in each parameter is less than a given amount." to "The incremental change in each parameter is less than a given percentage."
- In section 4.1.3.1, "Normalize The Abscissa – I.E., Convert From Gate Number To Time", updated description of compression.
- In section 4.1.3.11 "Smooth The Waveform And Check For A Viable Signal", added text to make it clear that there are two smoothed waveforms.
- Updated table 4.1, "Parameters input from ancillary file".
- Updated figure 5, "Block Diagram of Waveform Smoothing Methodology", and figure 6, "Smooth WF using Gaussian filter of width filtWidth".

ix. Changes from 4.4 to 5.0

- Changed text referring to ICESat from present and future tense to past tense.
- Numerous formatting and content changes to bring the document up to date.
- Removed section 3.2.3, Development of Equations for Area Conserving Special Processing.
- Added Appendices 2, 3, 4.5, 4.6, 4.12, 4.13, 4.14, 4.15, and 5.
- Updated parameter tables.
- Removed some paragraphs on techniques that were not used.
- Removed appendix 1 on the “area method for fitting waveforms” and replaced it with a discussion on why in-footprint slope and roughness could not be computed.
- Added Table showing which offset was used in calculating latitude, longitude, and elevation before Table 5-4, "Parameters to be output every measurement-level 2 ice sheet product"

TABLE OF CONTENTS

i.	Changes from version 1.0 to 1.1	2
ii.	Changes from version 1.1 to 2.0	4
iii.	Changes from version 2.0 to 3.0	5
iv.	Changes from version 3.0 to 4.0	7
v.	Changes from version 4.0 to 4.1	8
vi.	Changes from version 4.1 to 4.2	9
•	Added section 5.2.5., Calculation of Geoid	9
vii.	Changes from version 4.2 to 4.3	10
viii.	Changes from 4.3 to 4.4	11
ix.	Changes from 4.4 to 5.0	12
TABLE OF CONTENTS		13
LIST OF TABLES		15
1.0 INTRODUCTION		16
2.0 OVERVIEW AND BACKGROUND INFORMATION		17
2.1	ICE SHEET	17
2.2	SEA ICE	21
2.3	LAND	23
2.4	OCEAN	23
2.5	EXPERIMENT OBJECTIVES	24
2.6	HISTORICAL PERSPECTIVE	24
2.7	INSTRUMENT CHARACTERISTICS	26
3.0 ALGORITHM THEORY		27
3.1	PHYSICS OF PROBLEM	27
3.1.1	<i>Introduction</i>	27
3.1.1.1	Ice Sheet Elevation	27
3.1.1.2	Ice Sheet Roughness and Slope	28
3.1.1.3	Sea Ice Elevation and Roughness	28
3.1.1.4	Land Elevation, Surface Slope and Roughness, and Vegetation Height	29
3.1.1.5	Ocean Elevation	30
3.1.2	<i>Analysis of Waveforms Obtained By Pulsed Laser Altimeters</i>	30
3.1.2.1	Analytic Expressions For Flat or Uniformly Sloping, Terrain	31
3.1.2.1.1	Diffuse Terrain Types (Land, Snow)	31
3.1.2.1.2	Ocean Surface	32
3.1.2.2	Algorithms Derived From the Analytical Expressions	33
3.1.2.2.1	Ice Sheet Elevation	33
3.1.2.2.2	Ice Sheet Roughness/Slope	33
3.1.2.2.3	Sea Ice Elevation and Roughness	34
3.1.2.2.4	Land Elevation, Surface Slope and Roughness, and Vegetation Height	35
3.1.2.2.5	Ocean Elevation	36
3.1.2.3	Skewness and Kurtosis	36
3.2	MATHEMATICAL FORMULATION	37
3.2.1	<i>Development of Equations</i>	37
3.2.2	<i>Procedure</i>	40
4.0 ALGORITHM IMPLEMENTATION		40
4.1	OUTLINE OF THE PROCEDURE	41
4.1.1	<i>Input Variables</i>	41
4.1.2	<i>Transmit Pulse Characterization</i>	42
4.1.3	<i>Received Pulse Characterization</i>	42
4.1.3.1	Normalize the Abscissa – I.E., Convert From Gate Number To Time.	43
4.1.3.2	Calibrate the Waveform	43
4.1.3.3	Determine the Reference Range, Range_ref	43
4.1.3.4	Determine the Preliminary Range (Range_pre)	43
4.1.3.5	Determine the Preliminary Range Correction	44
4.1.3.6	Time Calculation	44
4.1.3.7	Geolocate the Footprint	45
4.1.3.8	Determine Surface Identifier from Regional ID Grid	45

4.1.3.9 Check Saturation.....	45
4.1.3.10 Calculate Noise Level.....	46
4.1.3.11 Smooth the Waveform and Check For A Viable Signal.....	46
4.1.3.12 Select Region within the Waveform with Which to Continue Further Processing.....	49
4.1.3.13 Fit the Waveform to a Function.....	49
4.1.3.13.1 Make an Initial Estimate for the Unknown Model Parameters.....	49
4.1.3.13.2 Normalize The Waveform and Estimated Parameters.....	51
4.1.3.13.3 Perform the Nonlinear Least-Squares Fit.....	51
4.1.3.13.4 Un-normalize the Solution Parameters.....	51
4.1.3.13.5 Output Parameters from the Fitting Procedure:.....	52
4.1.3.14 For Multiple-Gaussian Fits, Rank the Peaks Found.....	52
4.1.3.15 Calculate General Waveform Assessment Parameters.....	52
4.1.3.16 Calculate a Threshold Retracker Correction.....	52
4.1.4 Output Parameters.....	53
4.2 VARIANCE OR UNCERTAINTY OF ESTIMATES.....	54
4.3 NUMERICAL COMPUTATION CONSIDERATIONS.....	56
4.3.1 Programmer/Procedural Considerations.....	57
4.3.2 Calibration and Validation.....	58
4.3.2.1 Ice Sheet Validation with Existing Data.....	58
4.3.2.2 Validation of Sea Ice Algorithm.....	65
4.3.2.3 Land Validation with Existing Data.....	66
4.3.2.4 Validation of Ocean Algorithm.....	66
4.3.2.5 Validation During The 90 Day Cal/Val Period.....	68
4.3.3 Quality Control and Diagnostics.....	68
4.3.3.1 Quality Control and Diagnostics for Ice Sheet Products.....	68
4.3.3.2 Quality Control and Diagnostics for Sea-Ice Products.....	69
4.3.3.3 Quality Control and Diagnostics for Ocean Products.....	70
4.3.3.4 Quality Control and Diagnostics for Land Products.....	70
5.0 WAVEFORM, WAVEFORM ANALYSIS AND ELEVATION OUTPUT PRODUCTS.....	70
5.1 LEVEL 1B WAVEFORM PARAMETER PRODUCT –GLA05.....	71
5.2 LEVEL 1B GLOBAL ELEVATION PRODUCT-GLA06.....	72
5.2.1 Region Specific Range Increments.....	73
5.2.2 Calculation of Surface Elevation.....	73
5.2.3 Calculation of Reflectance.....	75
5.2.4 Calculation of the Footprint Orientation.....	76
5.2.5 Calculation of Geoid.....	76
5.2.6 Ancillary Information.....	78
5.2.7 Quality Information.....	78
5.3 ICE SHEET PRODUCT – GLA12.....	80
5.4 LEVEL 2 SEA ICE PRODUCT – GLA13.....	83
5.4.1 Ancillary Information.....	84
5.5 LEVEL 2 LAND PRODUCT – GLA14.....	85
5.6 LEVEL 2 OCEAN PRODUCT – GLA15.....	87
5.6.1 Ancillary Information.....	88
6.0 CONSTRAINTS, LIMITATIONS, AND ASSUMPTIONS.....	88
6.1 SURFACE CHARACTERISTICS.....	89
6.1.1 Effect on Slope Calculations.....	89
6.1.2 Effect on Roughness Calculations.....	89
6.1.3 Effect on Surface Elevation.....	90
6.2 INSTRUMENT EFFECTS.....	91
6.3 ATMOSPHERIC EFFECTS.....	91
APPENDIX 1, INABILITY TO COMPUTE SLOPE AND ROUGHNESS.....	92
APPENDIX 2, REL 33 PARAMETERS INPUT FROM ANCILLARY FILE.....	93
APPENDIX 3, REL 33 ANC07, WAVEFORM CONSTANTS.....	98
APPENDIX 4.5, REL 33 WAVEFORM-BASED ELEVATION.....	106

APPENDIX 4.6, REL 33 ELEVATION.....	108
APPENDIX 4.12, REL 33 ICE SHEET ELEVATION	110
APPENDIX 4.13, REL 33 SEA ICE ROUGHNESS.....	112
APPENDIX 4.14, REL 33 LAND/CANOPY ELEVATION	114
APPENDIX 4.15, REL 33 OCEAN ELEVATION	117

TABLE OF FIGURES

FIGURE 1 - CHARACTERISTICS OF RETURNED LASER PULSE AS A FUNCTION OF SURFACE TYPE. PRESENCE OF SURFACE SLOPE AND ROUGHNESS BOTH BROADEN THE PULSE.....	16
FIGURE 2 - GENERALIZED GEOMETRY OF THE TERRAIN	31
FIGURE 3 - CHARACTERIZATION OF TRANSMITTED AND RECEIVED PULSE WAVEFORMS.....	42
FIGURE 4 - DEFINITION OF REFERENCE AND PRELIMINARY RANGES.....	44
FIGURE 5 - BLOCK DIAGRAM OF WAVEFORM SMOOTHING METHODOLOGY	47
FIGURE 6 - SMOOTH WF USING GAUSSIAN FILTER OF WIDTH FILTWIDTH	48
FIGURE 7 - BIGFOOT WAVEFORMS OVER GREENLAND FIT WITH A GAUSSIAN FUNCTION.....	58
FIGURE 8 - SLA02 DATA FIT WITH A GAUSSIAN FUNCTION	59
FIGURE 9 - FORWARD SCATTERING EFFECT ON THE LASER RETURN WAVEFORM	60
FIGURE 10 - BIAS IN NS FROM SURFACE ELEVATION; STAR - CENTROID OF THE RETURN, DIAMOND - CENTROID OF THE GAUSSIAN FIT	61
FIGURE 11 - COMPARISON OF SIMULATED AND ACTUAL SURFACE AND RESULTANT GLAS ELEVATION ALGORITHM ERROR	62
FIGURE 12 - COMPARISON OF ACTUAL VS CALCULATED SURFACE ROUGHNESS AND SLOPE (NO LONGER CALCULATED).	62
FIGURE 13- SIMULATED ELEVATION AND CORRESPONDING WAVEFORM USING REAL ICE SHEET PROFILE.....	63
FIGURE 14 - SIMULATED ELEVATION AND CORRESPONDING WAVEFORM USING REAL ICE SHEET PROFILE	64
FIGURE 15 - SIMULATED LASER ALTIMETRY WAVEFORMS.....	65
FIGURE 16 A) COMPARISON OF SURFACE ROUGHNESS COMPUTED FROM LASER-ALTIMETER WAVEFORMS (SOLID LINE WITH DIAMONDS) AND FROM SURFACE ELEVATION (DASHED LINE WITH TRIANGLES), B) SURFACE ELEVATION PROFILE FROM AIRBORNE LASER-ALTIMETER DATA (REFLECTIVITY = 0.8).....	67
FIGURE 17 – CALCULATE RANGE CORRECTIONS AND TIDES	74
FIGURE 18 – CORRECT RANGE AND CALCULATE PRECISE GEOLOCATION AND ELEVATION	74

LIST OF TABLES

TABLE 4-1 THRESHOLD FOR SATURATION INDEX	45
TABLE 4-2 WAVEFORM ASSESSMENT PARAMETERS	52
TABLE 4-3 OUTPUT PARAMETERS FROM THE WAVEFORM CHARACTERIZATION PROCESS	53
TABLE 5-1 PARAMETERS REQUIRED TO CALCULATE PHYSICAL PROPERTIES OF THE SURFACE FOR LEVEL 1B WAVEFORM PRODUCT	71
TABLE 5-2 PARAMETERS TO BE OUTPUT EVERY MEASUREMENT –LEVEL 1B ELEVATION PRODUCT.....	79
TABLE 5-3 PARAMETERS TO BE OUTPUT ONCE PER SECOND LEVEL 1B ELEVATION PRODUCT.....	80
TABLE 5-4 OFFSET USED FOR LATITUDE, LONGITUDE AND ELEVATION CALCULATIONS.....	81
TABLE 5-5 PARAMETERS TO BE OUTPUT EVERY MEASUREMENT-LEVEL 2 ICE SHEET PRODUCT.....	81
TABLE 5-6 LEVEL 2 SEA-ICE PARAMETERS TO BE OUTPUT EVERY MEASUREMENT	83
TABLE 5-7 PARAMETERS TO BE OUTPUT EVERY MEASUREMENT FOR LEVEL 2 LAND PRODUCT	85
TABLE 5-8 LEVEL 2 OCEAN PARAMETERS TO BE OUTPUT EVERY MEASUREMENT.....	87

1.0 Introduction

The primary purpose of the GLAS instrument on the ICESat mission was to detect ice elevation changes that were indicative of changes in ice volume (mass balance) over time. GLAS did this by precision profiling of ice surface elevations over the Greenland and Antarctic ice sheets. Other objectives included measurements of sea ice, ocean, and land surface elevations; ice, water, and land surface roughness; multiple near-surface canopy heights over land; and cloud and aerosol layer heights.

The GLAS instrument used a laser altimeter to measure the range to the surface. Ranges were determined from the measured time between transmission of the laser pulse and detection of the photons reflected from the surface and received by the instrument. The laser footprint diameter on the surface was nominally 70 m, and the width of the transmitted pulse was 4 ns, equivalent to 60 cm in surface elevation. The returned laser pulse was broadened by the distribution of surface heights within the footprint as depicted in Figure 1. The surface height distribution was characterized by a mean surface

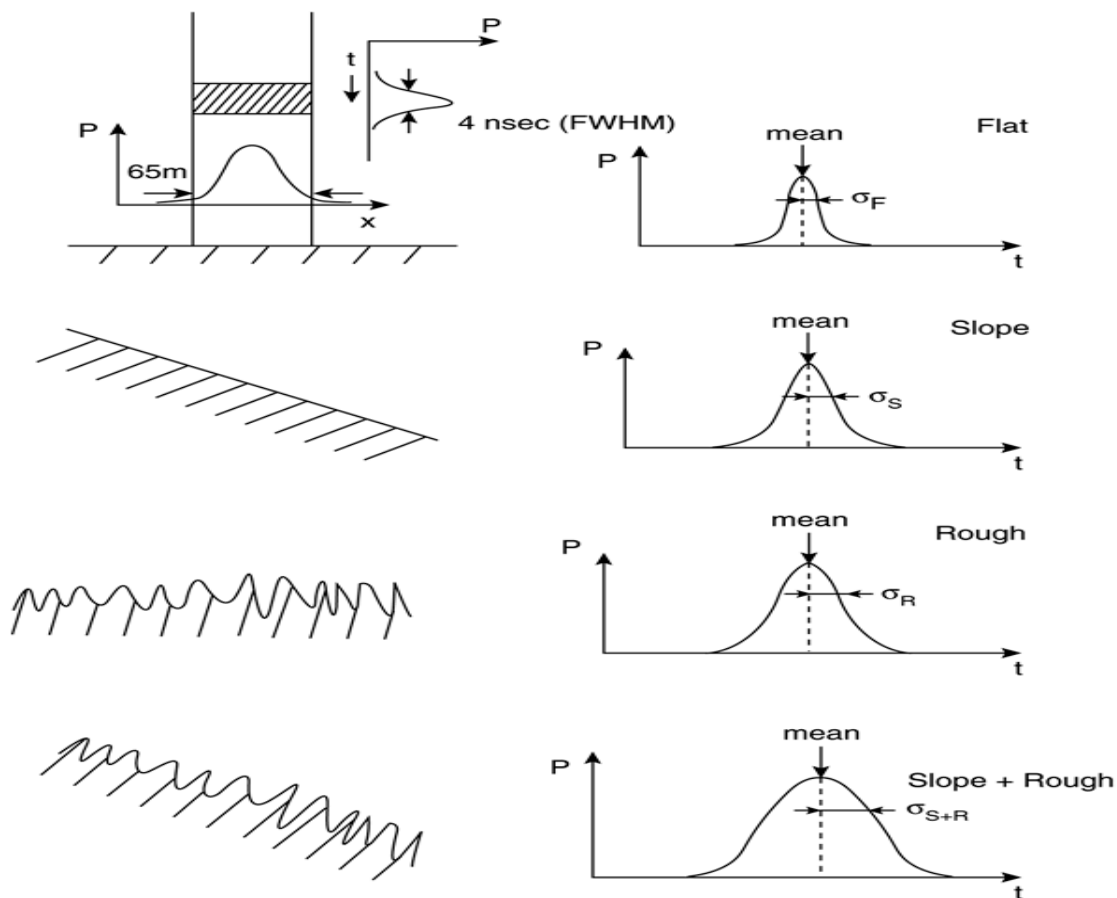


Figure 1 - Characteristics of returned laser pulse as a function of surface type. Presence of surface slope and roughness both broaden the pulse.

slope and a surface roughness within the footprint. The detected pulse corresponding to the reflections from the surface was selected by an instrument algorithm and digitized in 1 ns (15 cm) range bins. From a total of 1000 selected range bins, a smaller number, 544 over ice sheets and land and 200 over oceans and sea ice regions, was selected for transmission. The corresponding range widths of the transmitted bins were 81.5 m over ice sheets and 30 m over oceans and sea ice.

This document describes the analysis of the waveform of the laser pulse returned from the ground. The derived parameters are:

- average range (equivalent to the average surface elevation) within the laser footprint
- ranges (elevations) to multiple reflecting surfaces
- pulse width and other waveform shape parameters related to surface slope and roughness

Other GLAS ATBDs describe the orbit and attitude calculations, corrections for atmospheric path-length delays, and corrections for changes in the surface elevations due to tidal effects; these other data are needed to convert ranges into absolute surface elevations with respect to the geoid.

2.0 Overview and Background Information

GLAS is the Geoscience Laser Altimeter System consisting of both lidar and altimetry subsystems that flew on the dedicated platform comprising the mission referred to as ICESat, the Ice, Cloud, and Land Elevation Satellite. The following subsections talk to the properties of ice sheet, sea ice, land, and ocean, and what quantitative measurements will help us understand global climate warming and the interactions with these ecosystems and our environment.

2.1 Ice Sheet

There are only two major ice sheets in the world, one on Antarctica and one on Greenland. A good general description of the Antarctic ice sheet can be found in a book by Fifield (1987), from which the following paragraph is adapted.

The Antarctic ice sheet is composed of two unequal parts. The larger portion (10.35 million km²) lies in East Antarctica, where it reaches a maximum central elevation of just over 4000 m. This part of the ice sheet is mostly terrestrial, that is, it rests on a bed that would be mostly above sea level if the ice were removed and isostatic rebound allowed to take place. The massive Transantarctic Mountain chain, which stretches from Atlantic to Pacific across the continent, separates East Antarctica from West Antarctica (the two portions lie principally in the Eastern Hemisphere and the Western Hemisphere, respectively). The West Antarctic ice sheet itself comprises three very different provinces: the "inland ice", the ice shelves, and the Antarctic Peninsula. The inland ice, which is the main part of the ice sheet, 2 million km² in area, is mostly marine (i.e. it rests on a bed that would be sea floor in the absence of the ice) and attains a surface height of 2300 m. Abutting it on the Atlantic and Pacific sides are two large floating ice shelves, each about 0.5 million km² in area. The Antarctic Peninsula (also about 0.5 million km²), which stretches far northward from the main body of Antarctica toward South America, is an area of extensive mountainous terrain and complex ice cover, with several merging small ice caps, ice shelves, and outlet glaciers, and many ice-covered offshore islands.

The Antarctic ice sheet is in places over 4000 m thick; it contains 91% of the world's ice and 70% of the world's store of fresh water. Much of Antarctica is technically a desert - each year more than half of its surface receives in snowfall less than the equivalent of 100 mm of water. Essentially no melting of the snow occurs (except close to the more northerly margins) even in summer and each year a new layer is added. As the snow layers are added, deeper layers become compressed, eventually being transformed into ice. Gravity forces the ice to flow downwards and outwards towards the coast, where it is eventually lost to the ocean, principally by calving of icebergs.

The Greenland ice sheet (1.73 million km²) is a single, bowl-shaped unit whose bed in the interior of Greenland lies more or less at sea level. The ice flows outward through the mountains that ring the island in a series of outlet glaciers, most of which reach the ocean either directly, or, more often, through fjords that connect to the ocean. Snowfall rates in the interior and melt rates around the periphery are greater than in Antarctica. As it is eight times smaller than the East Antarctic ice sheet it has approximately an

eight-fold larger perimeter: area ratio. Because of this and the relatively high melt rates surface melting is a much more important component of the overall ice-mass balance in Greenland than in Antarctica. There are few ice shelves in Greenland.

Slope Characteristics: The speed of outward ice flow from an ice sheet is sufficient large to balance the incoming snowfall (when averaged over many centuries). In this way, ice sheets are able to maintain approximately parabolic profiles. The central regions are consequently very flat, with gradients on the order of 1:1000. Toward the ice margin, surface slopes and flow speeds are higher, the ice is thinner, and stresses from flow over the irregular sub-glacial bed makes the ice surface more undulating. Within 200-300 km of the coast, the ice may become channeled, either through peripheral mountains where outlet glaciers develop, or through ice streams, fast-flowing zones within the ice sheet. Here the slopes are highly variable, from as much as 1:10 where the ice is flowing slowly to as little as 1:1000 on the fast-flowing, low-gradient ice streams. The coastal regions, with their widely variable slopes, are of particular importance in the context of global change, because it is here that any reaction of the ice sheets to changes in climate will first appear. More than half of Antarctica has gradients less than 1:300 and 90% has gradients less than 1.5%. Only 3% of the ice sheet, in the marginal areas, exhibits gradients larger than 3% (Drewry et al, 1985). Greenland has a similar distribution of slopes, except that the ratio of the marginal areas to the total is several times larger.

Most of the ice discharging from the Antarctic ice sheet flows into the sea. In many places it floats and continues to move outward in the form of ice tongues and coalescing ice shelves, which spread out under their own weight. The largest ice shelves are hundreds of kilometers across and exhibit changes in ice thickness on the order of 1 m per kilometer. Since the ice shelves float in hydrostatic equilibrium, this produces surface slopes on the order of 1: 10,000.

Roughness Characteristics: At first glance the surfaces of the ice sheets appear smooth, but in reality they are roughened in three fundamentally different ways. On the smallest scale there is the roughness caused by the wind and variations in the rate of snow accumulation, which comprises irregular features called "sastrugi" and "snow dunes" (Kotlyakov, 1966; Doumani, 1967). Sastrugi are erosional or erosional/depositional features that vary widely in size, both vertically and horizontally, depending on the wind characteristics and history in a particular region. In many areas the irregularities of the surface are 0.1 m or less in height, with typical horizontal wavelengths on the order of several meters. Over parts of the interior of Antarctica, however, the sastrugi can reach heights as great as a meter (e.g. Endo and Fujiwara, 1973); horizontal wavelengths are larger, although not necessarily proportionally larger. Snow dunes are accumulative features that are somewhat larger than sastrugi - they can be up to several meters in amplitude and tens of meters in wavelength. (N. B. These physical features are larger than the meteorologically defined "surface roughness parameter," which is the height above the mean surface, at which the wind speed is zero and it typically has a value of 0.01 m, so over a snow surface with sastrugi (Paterson, 1994, p. 62-63), because of the streamlined shapes of the sastrugi and dunes.)

Roughness due to sastrugi is anisotropic; sastrugi ridges are elongated in the direction of the wind, so the roughness characteristics are different along, and normal to, that direction.

An absence of surface roughness can also be an important characteristic of the ice-sheet surface. In particular, a smooth, glazed surface probably represents a region that has been free of snow accumulation for several years or more (Watanabe, 1978).

The second type of roughness has much longer wavelengths and has two different causes. First, there are the undulations of the surface that result from the flow of the ice over topographic irregularities in the bed. Although the flow characteristics of the ice are such that the vertical scale of the relief of the surface is much less than that of the bed, surface relief nevertheless exists and in many places is pronounced. Amplitudes of this relief are commonly a few meters to tens of meters, with horizontal wavelengths of hundreds of meters to many kilometers. The thickness of the ice sheet modulates the surface relief in two ways - the thicker the ice, the smaller the amplitude of the surface relief and the greater its dominant

horizontal wavelengths. The ice sheet acts like a band pass filter - subglacial relief of wavelengths short compared to the ice thickness is damped by the strength of the ice sheet, whereas very long wavelengths are attenuated by the plastic flow of the ice. Second are the megadunes, identifiable on AVHRR and SAR images, which are comparable in size to the flow-produced undulations but more regularly sinusoidal in form. Megadunes, which are believed to be produced by atmospheric standing waves, cover about 20% of the Antarctic ice sheet (K. C. Jezek, pers. Comm., 1999). They have not been recognized in Greenland. It is the long-wavelength roughness, which grows more pronounced in the coastal regions where the ice is thinner and moving faster, that causes one of the most serious problems for radar altimetry, with its wide beam. The surface undulations are such that often the nearest point on the surface to the satellite carrying the altimeter is displaced substantially from the nadir point on the surface, or even from the nearest point on the mean sloping surface. Furthermore, the radar altimeter commonly records overlapping returns from two or more topographic high points. Under most circumstances the surface relief is far too complex, and the sampling from the radar altimeter too sparse, for it to be possible to deconvolve the radar returns to extract the real surface topography.

The third type of roughness stems from cracks in the surface - crevasses. These develop anywhere that the stresses in the ice from variations in flow exceed the breaking strength of the ice in tension. They are caused by lateral variations in flow speed and/or direction as the ice flows over basal topography, around bends in a subglacial channel, or through regions of rapid acceleration (longitudinal or transverse). Crevasses vary widely in scale, from millimeters to tens of meters across and from tens of meters to kilometers long. Spacings between crevasses are characteristically on the order of one or two hundred meters. Like the undulations, crevassing has a strong tendency to be more pronounced in locations nearer to the coast. In extreme cases, (e.g. the Jakobshavn ice tongue in Greenland) the crevassing is so severe that the surface becomes a jumbled series of pinnacles - seemingly more crevasse than ice.

Even a moderately crevassed surface will destroy the coherence of a back-scattered pulse from a satellite radar altimeter if the crevasses are open, because even a single crevasse can provide a multitude of reflecting (or diffracting) points. Furthermore, much of the strength of the signal is lost by being scattered out of the return beam.

Surface and Airborne Observations: In view of the extensive oversnow traverses that have been conducted in Antarctica and Greenland it is perhaps surprising that so little quantitative information has been published on surface roughness. Comments often appear in traverse reports, but they are typically qualitative and subjective, relating principally to the difficulty caused to travel by large and hard sastrugi.

A few studies of small-scale roughness from surface measurements do exist, principally from work of the Japanese Antarctic Research Expedition. The most comprehensive is that of Watanabe (1978) in central Queen Maud Land, Antarctica; that work was extended eastward to Enderby Land by Furukawa et al, 1992. The emphasis of these analyses has been on the categorization of the wind systems, particularly of the katabatic winds that dominate the East Antarctic slope region and control the orientation of the sastrugi.

Measurement of the undulations related to the subglacial topography were limited to two-dimensional profiles when the only source was the surface traverses. Analyses and theoretical studies led to various quantitative relationships between surface and basal topography (Robin, 1967; Budd, 1970; Budd and Carter, 1971; Hutter, 1981; Whillans and Johnsen, 1983; Reeh et al, 1985). When the results of extensive airborne radio-echo sounding became available, McIntyre (1986) showed the importance of extending the study into three dimensions. He found that wavelengths of two to ten times the ice thickness tend to predominate and that the energy of the surface-relief spectra increases markedly towards the coast.

Measurement Objectives: There are two principal reasons for measuring the small-scale roughness (the first type). In the first place, the interaction between the rough surface and the wind moving over it is an important aspect of boundary-layer meteorology. Furthermore, the size and time-history of the surface

roughness of the first type discussed above is a measure of the magnitude and history of strong winds. Secondly, the roughness is an important limiter on the accuracy of the surface-height measurements. Roughness on this scale will be reflected in the broadening of the pulse and will be indistinguishable, by that measure alone, from a mean surface slope within the footprint. For research purposes the roughness will have to be separated from the slope after the fact, when the surface elevations (and hence slopes) have been mapped.

The second type of roughness is important for the information it will reveal about ice dynamics and the subglacial topography. Those longer-scale irregularities of the surface will be revealed by the main surface-elevation mission.

It is unlikely that any quantitative measurement of crevasse characteristics (the third roughness type) will result from the GLAS measurements. Nevertheless, the occurrence of multiple returns from the ice sheet will provide a warning of the presence of crevasses, which affect the accuracy of the basic height measurements.

Radar Altimetry: Many of the characteristics of satellite laser altimetry over ice sheets carry over from radar altimetry, which has a 30-year history. The basic measurement is the same in principle - the determination of the time of flight of an electromagnetic pulse from the satellite to the surface and back. For both types of altimeter the shape of the return pulse is modified by irregularities in the ice-sheet surface. There are, however important differences that arise from the different wavelengths and beam widths and that affect both the height and the surface roughness calculations. Before discussing those, however, we will review briefly the effect of surface slope and roughness on the radar pulse.

Because of the wide radar beam, the surface slope has a fundamental effect on the radar return - the return will come, not from nadir, but from the nearest point on the surface that lies within the beam. There is no immediate information in the return on the location of that point - it can only be determined using knowledge of the surface topography generated from the measurements themselves. Several schemes have been devised for doing this that differ in where the corrected height point is taken to be relative to the sub-satellite point (Brenner et al, 1983, Rémy et al, 1989; Bamber, 1994). All schemes suffer from the lack of detailed slope information in the direction normal to the sub-satellite track on the surface. This problem will be alleviated but not eliminated as digital elevation models of the surface are improved (Bamber and Huybrechts, in press).

The roughness of the surface will affect the shape of the back-scattered pulse - the greater the roughness (of the first type cited above) the broader the received pulse will be, other things being equal. The problem with using this characteristic to evaluate surface roughness is that the dominant effect on the radar pulse shape is often the undulations of the surface (roughness of type 2, above) (e.g. Martin et al, 1983). McIntyre (1986) showed that the amplitude of undulations at wavelengths less than 10 km is significant, even in the central part of the ice sheet. Distortion of the returned pulse can be exacerbated by crevassing (roughness of type 3).

Another complicating factor is that a significant portion of the incident signal may penetrate the firn to a depth of some meters before being scattered back (e.g. Partington et al, 1989). Nevertheless, by averaging a large number of waveforms and taking penetration into account, Partington et al, 1989 were able to calculate average roughness values on the plateau of Wilkes Land, Antarctica - they found the rms roughness to be about 1 m. This is significantly larger than the estimates from surface measurements, which suggests that the effects of volume scattering and/or type 2 surface undulations have not been taken fully into account. Davis and Zwally (1993) and Yi and Bentley (1994) made similar calculations from similar models, also for the East Antarctic plateau. Davis and Zwally found roughnesses ranging from 0.05 m to 0.15 m, substantially less than found by Partington et al, 1989, whereas Yi and Bentley (1994) calculated values in the 0.5 to 1 m range, closer to those of Partington et al, 1989.

Another approach is to use the total returned power, averaged over a large number of returns, as a measure of the mean surface roughness. In this way Rémy et al, 1990 calculated variations in roughness that agreed well with the expected katabatic wind variations on the East Antarctic plateau. This method, however, does not yield any quantitative estimate of the absolute roughness.

Other Satellite Studies. Variations in surface roughness have also been estimated from passive microwave data. Seko et al, 1991 related small differences in brightness temperature to band-shaped undulations of the surface with amplitudes of a few tens of meters and spacings of tens of kilometers. Rémy and Minster (1991) employed the fact that the difference between the brightness temperatures (or emissivities) for horizontally and vertically polarized microwaves radiated from the surface diminishes as the surface roughness increases. These differences showed a remarkably good correlation with the variations in returned power over an extensive portion of East Antarctica. Further support for the association of roughness with katabatic wind speed was found from an analysis of SEASAT scatterometer data over the same region (Rémy et al, 1992; Ledroit et al, 1992).

Comparison With Radar Altimetry: There are two crucial ways in which the laser altimeter differs from the radar altimeter - it has a much smaller footprint and it operates at a much higher electromagnetic frequency. The small footprint means that returns will come from only one spot on the surface at a time and that the position of that spot will be known. The high frequency means that the signal will not penetrate deeply below the surface. These characteristics simplify greatly the determination of the surface geometry. On the other hand, clouds and aerosols in the atmosphere affect the laser beam, so

- Heavy clouds (optical depth >2 or so) will completely block ground returns
- Thinner clouds and aerosols cause forward scattering, which distorts the waveform, thereby shifting the centroid of the return pulse (and of fitted Gaussians) to later times.

2.2 Sea Ice

The polar oceans are, at least seasonally, covered by a thin, uneven sheet of sea ice. Although its thickness is small (a few centimeters to a few meters), sea ice has a profound influence on the physical, chemical, and biological characteristics of the oceans and the global climate system (e.g. Comiso, 1995). Because of the huge area, hostile weather conditions and long period of darkness, satellite remote sensing systems have been the major tools for mapping and monitoring the sea ice, with emphasis on microwave sensors, both active and passive (e.g. Carsey, 1992; Comiso, 1995; Perovich, 1996).

Sea ice is a complex material consisting of an ice matrix with inclusions of air, brine, solid salt and contaminants. It varies, spatially and temporally in thickness, composition, snow cover, wetness, and surface roughness. Sea ice can be classified by age (typically new ice, first-year ice, and multi-year ice), by structure (e.g. frazil, grease ice, nilas, pancake, columnar etc), or by the degree of deformation. During the winter, the surface is generally covered by snow, which in summer may melt to form slush and melt ponds. Particularly in the Antarctic, where the ice is thin, heavy snow loads can depress the ice sufficiently to permit flooding of seawater above the ice/snow interface.

Sea ice affects both the overlying atmosphere and the underlying oceans in several ways. It is a strong insulator, limiting heat exchange between ocean and atmosphere, it modulates the exchange of momentum between atmosphere and ocean, and with its high albedo it strongly affects the absorption of radiant energy by the Earth. During formation, sea ice rejects salt, and it produces fresh water when melting, thus affecting the salinity structure of the ocean with important ramifications for deep convection, bottom-water formation, and blooms of ocean biological productivity associated with the ice edge in spring. In addition to these characteristics that influence weather and climate in ways that are still poorly understood, sea ice obstructs shipping, modifies submarine acoustics, and provides an environment essential to the survival of a wide variety of polar animals.

Sea-Ice Surface Characteristics: The most notable sea-ice deformation features are ridges, rubble fields, ice rafts, and open-water leads. Ridges can be long quasi-linear features extending for several kilometers, but they generally are sinusoidal and extend for several hundred meters. Repeated ridging causes rubble fields. Ridges usually are a meter to a few meters high and their appearance depends on their age. First-year ridges are composed of piles of very angular ice blocks, while multi-year ridges are typically well rounded, hummocky features with few, if any, voids.

On a somewhat smaller scale are the broken and rafted ice fields. Broken ice fields are formed from refrozen ice blocks and their characteristic vertical roughness ranges from a few centimeters to a meter. Rafting occurs when convergence causes one sheet of ice to override another, causing linear or sinusoidal features sometimes extending several kilometers, with vertical relief of less than a meter. Often, however, finger rafts occur, which have a distinctive square wave appearance. Wind-induced snow dunes and snowdrifts also frequently occur on snow-covered sea ice. These typically have vertical dimensions of a few cm to tens of cm.

On a very small scale, roughness is determined by the crystal structure of the surface snow or ice layer. Tucker et al, 1992 summarize the standard deviation and correlation length values published in the literature. The surface roughness usually ranges from 0.05 to 2 cm over a correlation length of 0.5 to 20 cm.

Perovich (1996) provides the most recent and comprehensive summary of sea ice optical properties. Albedo values quoted in this section are from Grenfell and Perovich, 1984. The spectral albedo of snow and sea ice is characteristically highest at visible wavelengths, decreasing strongly in the infrared because of increasing absorption by ice and water. Variations are due primarily to differences in the air bubble density, crystal structure, and fresh water content of the upper layer of the ice.

For sea ice, which is covered by fresh, cold snow, albedo is generally high. For sea ice covered by cold snow near-infrared (NIR) albedo can be as high as 0.7¹. The aging of snow results in an albedo decrease at all wavelengths, because of the increase of grain size and rounding of the grains. This decrease is especially pronounced in the infrared (albedo for melting snow = 0.5), where absorption by ice and water is very large and the upward scattered radiation is very sensitive to the scattering properties of individual grains at the surface.

Bare sea ice has lower albedo values and exhibits more pronounced specular behavior than that of ice covered by snow. Drained white sea ice, which is located above the local freeboard level, has only slightly smaller albedos (about 0.4) than melting snow. Blue ice occurs when the surface becomes saturated with meltwater, which fills in near-surface irregularities so that backscattering is reduced. When blue ice develops into melt ponds, it can reduce the infrared albedo down to the specular reflection limit of 0.05, and it remains constant for the ponds until they refreeze or drain completely. The absorption coefficient of sea ice is very close to that of seawater, therefore the light penetration is negligible at NIR wavelengths.

Multiyear ice has survived a summer melt season, with the attendant surface melting and brine drainage to form a well-developed surface-scattering layer with many air bubbles. Consequently, albedos are typically larger than first-year ice values (Perovich, 1996).

Most sea ice can be regarded as a nearly horizontal, rough surface. The roughness is an indication of the history of the ice, and strongly influences its drag coefficient and hence its response to winds. The surface elevation of flat regions is a close approximation to local sea-surface elevation, but slightly biased upwards, depending on the ice thickness. Sea-ice covered ocean also contains icebergs, with surface elevations significantly higher than that of the sea ice. The algorithms described in this document will be applied to GLAS data to provide estimates of sea-ice elevation and roughness, and of iceberg elevations.

¹ All albedo values in this section are at the wavelength of the GLAS system, i.e. 1.064 microns

2.3 Land

The Earth's land surface is a complex mosaic of geomorphic units and cover types resulting in large variations in elevation, slope, roughness, vegetation height and reflectance, often with the variations occurring over very small spatial scales. The spatial variations of these land surface properties are important in a host of scientific applications encompassing all Earth science disciplines. These properties are the product of a diverse set of lithospheric, cryospheric, hydrospheric, ecologic, and atmospheric processes acting on multiple time scales whose integrated effects generate the landscape seen today. Documentation of these landscape properties is a first step in understanding the interplay between the formative processes. Characterization of the landscape is also necessary to establish boundary conditions for models which are sensitive to these properties, such as predictive models of atmospheric change that depend on land-atmosphere interactions. Adequate knowledge of these characteristics is also critical to proper utilization of the land as a resource. Current descriptions of these land properties are in many respects deficient. The best publicly available global representation of the Earth's topography is a Digital Elevation Model (DEM) with a spatial resolution of 1 km, too coarse for the needs of most land process studies. This product is also an amalgam of many disparate topographic sources with inconsistent, and often poorly known, methods of production and a diversity of horizontal and vertical datum. Furthermore, on a global basis, there is no product presently available that characterizes the variation of the Earth's surface roughness and vegetation height at the short spatial scales necessary for many process studies and models. ICESat's contribution was to provide a global sample of land topography and vegetation height data of value in their own right for characterization of landscape properties but also of great value as a reference for calibration and validation of topographic and vegetation products generated by other means. In particular, high-resolution, land topography DEMs and, to some extent, vegetation height images derived from spaceborne optical stereo photogrammetry and interferometric synthetic aperture radar techniques are becoming more readily available. The ICESat products, inherently defined in a consistent, Earth-centered reference frame established globally distributed geodetic control for these products.

Because of the complex variations in land surface properties at short spatial scales, the interpretation of GLAS land waveforms was less certain than is the case for the simpler cases of ice sheets, sea ice, and ocean. Within any one GLAS laser footprint, multiple targets distributed in height can contribute to the received backscatter signal. For the land, sloped and/or rough ground, vegetation, and cultural features (e.g., buildings, vehicles, etc.) may all be contributing to a waveform. The purpose of this document with respect to land waveforms is to document methods for processing and analysis that account for the potential complexities of the surface-height distribution within land footprints.

2.4 Ocean

ICESat spent most of its lifetime over the ocean acquiring a vast amount of information on sea-surface characteristics. The shape of the GLAS return-pulse waveform was determined primarily by the surface-height distribution within the footprint, which was small enough to be affected by individual large waves.

Over distances of cm to a few hundred meters, the sea surface is roughened by waves and ocean swell, but over distances of many km, the sea surface is almost flat and horizontal. Nevertheless, surface slopes and long-wavelength undulations are present, caused by variations in Earth's gravity field, associated for instance with seamounts, ocean currents, and variations in atmospheric pressure and seawater density. Satellite radar altimeters have shown remarkable success in measuring sea-surface elevation and significant waveheight, and will continue to be the prime tool for this purpose. Because of its large effective footprint, a satellite radar altimeter averages the effect of the small-scale roughness in the information contained within the composite, 0.05 -0.1 second return pulse from which estimates of surface elevation and roughness are inferred. Consequently, the resulting sea-surface elevations can be used to study the longer-wavelength variability, and estimates of surface roughness are a statistical indication of the wave height. Errors are primarily associated with orbit uncertainty, atmospheric effects,

and noise in the instrument system. The noise effects require averaging of several return pulses (at least 1 second's worth) for highest accuracy, which limits along-track spatial resolution. There may also be a range-measurement bias, associated with asymmetry in the shape of ocean waves, which increases with increasing wave height.

2.5 Experiment Objectives

The objectives of GLAS surface elevation measurements are stated in detail in the *Geoscience Laser Altimeter System (GLAS) Science Requirements* document available online at http://www.csr.utexas.edu/glas/Science_Objectives/. In summary, they are:

- Measure elevation changes of the Greenland and Antarctic ice sheets for the purpose of assessing:
 - a. mass balance,
 - b. seasonal and interannual elevation variability,
 - c. elevation trends, and
 - d. contribution to sea level rise
- Determine precise elevation topography of ice sheets and sea ice.
- Conduct global topographic measurements to contribute to topographic maps and digital elevation models as well as detect land elevation changes in excess of 1 meter per year in certain selected regions.

In order to achieve these objectives, accurate and consistent interpretation of the waveforms is necessary. Toward that end, the goals of the waveform surface elevation algorithm development are:

1. Define and determine the surface elevation from the laser waveforms
2. Identify and interpret multiple returns
3. Determine slope based on waveform characteristics (See appendix 1 for an explanation for the removal of slope and roughness from the products).

2.6 Historical Perspective

The idea of using an altimeter in a space orbit to measure the earth's surface was first shown as feasible when a radar altimeter was flown on Skylab in 1974. In 1975 GEOS-3 became operational with a radar altimeter that was designed to measure the ocean surfaces. GEOS-3 covered latitudes of +/- 65 deg that included the southern tip of the Greenland ice sheet. Brooks et al, 1978 showed the feasibility of using these radar altimeter measurements to get topographic measurements over Greenland. Two other U.S. missions, SEASAT in 1978 and GEOSAT (1985-89), flew radar altimeters also designed to measure ocean surfaces. These covered latitudes to +/- 72 deg and could only maintain track over slopes less than 1 deg giving coverage of 40% of Greenland and 24% of Antarctica. NASA developed algorithms (Martin et al, 1983) to post-process the return pulse energy waveform to calculate surface elevations of the ice sheets, and topographic maps were produced (Zwally et al, 1983). Methods were also developed to calculate elevation changes using information from crossing arcs from measurements at different times (Zwally et al, 1989).

The launching of the ERS-1 radar altimeter and its successor ERS-2 have given us continuous ice sheet measurements since 1991 that extended coverage up to +/- 81 deg. These newer altimeters were also designed with a special ice mode capability to extend coverage of tracking into the more sloping regions of the ice sheets and land. Elevation change estimates have been calculated from the radar measurements giving change histories from 1978 to present day (Wingham et al, 1998, Davis et al, 1998). However, due to limitations of radar altimetry these have large error bounds. Radar altimeter data have also been applied to measurement of land elevations in a few cases. (Frey and Brenner 1990, Brenner et al, 1990, Koblinsky et al, 1993, Bamber and Muller 1998).

There are several limitations in measuring ice sheet and land elevations using radar altimetry:

1. The footprint is very large 10-20 km in diameter, increasing with the surface slope.
2. The measurement is a mean elevation over the footprint surface for flat surfaces with small undulations.
3. Over sloping surfaces, the measurement is to the higher elevations that are not necessarily at the sub-satellite location, and topographic knowledge is inadequate to properly geolocate the measurement.
4. Tracking can only be maintained over small slopes, ~ 1 deg

A spaceborne laser altimeter can overcome many of these limitations. The footprint for GLAS was ~ 70 m so that the effect of sloping surfaces is reduced greatly. GLAS was able to track surfaces on slopes up to 3 deg, which included the majority of the continental ice sheets. The main problem with the small footprint is the accuracy to which the off-nadir angle must be known in order to precisely geolocate it. This was addressed by the use of a precise Laser Reference System (LRS).

A small footprint (1m), scanning laser altimeter, the Airborne Topographic Mapper (ATM) has been flown successfully over the past 20 years on aircraft over the Greenland ice sheet (Thomas et al, 1994,) with the objective of measuring the rate of change of surface elevations towards assessing ice-sheet mass balance. As with all laser altimeters, major limitations are the accuracy of the aircraft position in inertial space and atmospheric interference in the form of clouds or ice fog. Nevertheless, 10-cm accuracy is achieved over flight lines of several hundred km (Krabill et al., 1995), yielding data that have been used to infer rates of ice thickening and thinning over much of the ice sheet (Krabill et al., 2000). The scanning ability of the ATM provides highly detailed surface topography within the 140-300m surveyed swath, which can be used to help simulate GLAS waveforms and, after launch, to validate GLAS-derived surface elevations and roughness.

The predecessor of GLAS, the Mars Orbiting Laser Altimeter, MOLA, uses algorithms similar to those that GLAS used and demonstrated the feasibility of using a spaceborne laser to map a planet surface (Zuber et al, 1998). The accuracy of MOLA was limited by its tracking algorithm (post-processing was not feasible since there are no waveforms telemetered) and the orbit accuracy that is driven by the precision of the gravity models available. Orbit determination with the advent of GPS, more accurate force models, and sophisticated computer techniques gave us the position of the earth-orbiting ICESat satellite to an accuracy of 5 cm in inertial space. This satellite position accuracy, combined with the very accurate attitude knowledge, altimeter measurements, and models to account for the atmospheric delays and earth dynamic effects, allowed us, in ideal conditions, to measure the ice sheets to within 10 cm. The Shuttle Laser Altimeter (SLA) experiment provided space-based heritage for the ICESat mission. SLA was a pathfinder experiment devoted to: (1) evaluating engineering and algorithm techniques for high-resolution, orbital laser altimeter observations of terrestrial surfaces, and (2) providing pathfinder scientific datasets of value in addressing global Earth System science issues (Garvin, et al, 1998). The first and second flights of SLA characterized ocean, land, and cloud top elevation and vertical roughness in 100-meter diameter laser footprints spaced every 700 meters along a nadir profile. SLA was a hybrid instrument combining ranging electronics modified from the MOLA design (Zuber, et al, 1992), with a high-speed digitizer used to record the backscatter return amplitude as a function of time (i.e., waveform). Processing methodologies developed from the Shuttle Laser Altimetry, SLA, missions (Garvin et al, 1998) and radar altimetry (Zwally et al, 1994) laid a good background from which to produce operational algorithms to process the GLAS measurements and allowed us to meet our science requirements.

Airborne laser altimeter heritage also provided experience in utilizing lidar waveforms for characterizing surface elevation and vegetation canopy height. Several implementations of airborne surface lidars have adapted bathymetric water depth sounding lidars in order to assess their ability to measure forest canopy height using green wavelength backscatter waveforms (Aldred and Bonnor 1985, Nilsson 1996). A near-infrared, Nd:YAG lidar system developed at Goddard Space Flight Center was specifically optimized to measure canopy vertical structure and the elevation of the underlying ground (Bufton et al, 1991, Blair et al, 1994). A scanning version of this system, the Scanning Lidar Imager of Canopies by Echo Recovery

(SLICER), has been used to measure canopy structure of Eastern U.S. deciduous forests (Lefsky 1997, Lefsky et al, 1999) and Pacific Northwest fir stands (Harding et al, 1994, Harding 1998, Lefsky et al, 1998, Means et al, 1999). The SLICER waveform measurements of canopy height and structure showed strong correlations with ecologically important forest stand attributes such as above ground biomass and stem basal area. The waveform data used to date to characterize canopy structure and ground topography beneath canopies were acquired using laser footprints on the order 10 m in diameter. Airborne lidar waveform measurements with footprints in a variety of sizes and configurations have been used to monitor topographic change at Long Valley Caldera, California (Hofton et al, in press). The Goddard airborne lidar system has also been used in a large-footprint profiling mode (Bigfoot) to collect data over the Greenland ice sheet and vegetated terrains of North America that emulate the waveform data to be acquired by ICESat.

2.7 Instrument Characteristics

The GLAS instrument used an Nd:YAG laser with 1064 and 532 nm output. The elevation measurements are determined from the round-trip pulse time of the infrared pulse, while cloud and aerosol data are extracted from the green pulse. The instrument was nadir-viewing with a pointing accuracy of 20 arc seconds. The post-processed pointing knowledge was 1.5 arc seconds. At a nominal altitude of 600 km, the 375 microradian field-of-view telescope had a spot-size of 70 ± 10 m in diameter. The pulse frequency was 40 Hz, which resulted in spots that were separated by 175 meters center-to-center on the ground. The requirement for knowledge of post-processed position was better than 5 cm in the radial direction, and better than 20 cm horizontally.

The platform was placed in a 91 day ground track repeat cycle (except in the initial 90-day verification phase) which yielded 30 km spacing between repeat tracks at the equator, and 5 km spacing at 80 degrees latitude. This allowed for adequate measurements to be able to calculate the required accuracy of mean elevation changes after averaging over 100 km².

The GLAS instrument algorithms are described in detail in McGarry et al. The following excerpts give enough information so that the reader can understand the algorithms described in this ATBD. The laser altimeter on ICESat collected about 4,500,000 1-ns samples for each transmitted laser pulse. It was not possible to telemeter this entire data stream to Earth, so on-board processing of the GLAS waveforms was essential to retrieve the desired data. 544 samples were telemetered over ice sheet and land surfaces and 200 samples over sea ice and ocean surfaces. The GLAS on-board altimetry algorithm was developed to maximize the chance that the telemetered data would include the ground return. That met the science requirement of being able to maintain measurements over 3 deg slopes and gave a large enough range window (81.6m over land and land ice and 30 m over sea ice and ocean) to measure all levels of expected roughness.

The algorithm did not include an acquisition or tracking phase, but relied on a simpler scheme using a Digital Elevation Model (DEM) to select the region of the echo waveform to be searched for the ground return.

The altimeter algorithm bounded the search area of the digitized waveform using apriori information stored in an onboard Digital Elevation Model (DEM). The DEM was interrogated once per second to determine min and max values of the range window and the type of surface (ocean, sea ice, land, or ice sheet), which would determine the number of elements in the returned waveform and the vertical range it covers.

The digitized waveform information within this DEM bounded region (called the Range Window) was filtered through 6 matched filters (in the hardware electronics) to maximize the probability of finding echoes from sloped or rough terrain and minimize the probability of selecting cloud returns. A separate threshold was determined for each of the filtered waveforms to distinguish the signal level from that of the noise. The thresholds were set as a function of the noise using a 1 km region of the digitized waveform

beyond the end of the Range Window where we are sure that no laser light was reflected back to affect the calculation.

Because the echo from the ground was expected to be the last local maximum in the Range Window, the algorithm searched for the surface echo backward in time from the end of the Range Window towards the start. The pulse defined by the first threshold crossing (from below the threshold to above) to the next corresponding threshold crossing (from above the threshold to below) was selected for each filter (providing that such a pulse existed for each filter). A weighting factor that was a function of pulse attributes was used to determine which filtered output was most likely to contain the surface echo.

Once the filter was selected, it was used solely to determine where the start of the received waveform digitized data sampling would be. The data to be sent to the ground was obtained directly from the received digitizer waveform. 1000 one ns samples were stored on-board from which to select the telemetered return. The samples were sent at full resolution or compressed to enlarge the measured range span to cover tall trees and large topographic relief. Two different compression ratios were used, one for the beginning and one for the end of the waveform. The sample at which the compression ratio changed was also input. The compression ratio allowed one to increase the range window over land if requested in order to assure that all canopy heights were included. Nominally the 81.6m range window was adequate, but for special requirements the compression option was turned on.

3.0 Algorithm Theory

This section presents the physics behind the problem and how to parameterize the altimeter return pulse to obtain physical results.

3.1 Physics of Problem

3.1.1 Introduction

The GLAS system used a pulsed laser to measure the precise range from the satellite to the terrain and to provide clues of the surface elevation distribution within the laser footprint. Average reflectivity of the surface at the monochromatic laser wavelength was also obtained from the ratio of the transmitted and received energy.

This chapter summarizes the background on the waveform and timing of the backscattered laser signal. Assuming that the effect of forward scattering by clouds and aerosols is negligible the shape of the received signal is determined by the range distribution inside the laser footprint modulated by the local reflectivity and the incident beam pattern. Gardner (1982, 1992) and Tsai and Gardner (1982) have developed detailed analytical expressions (see Section 3.1.2.1) to describe the received pulse for simple ground target geometry. These expressions have been used to evaluate the performance of satellite laser altimeter systems (Gardner, 1992 and Harding et al, 1994) and to develop algorithms for GLAS data processing (Csathó and Thomas, 1995). For complex terrain the received waveform can be computed by using the Goddard Laser Altimetry Simulator Software (Abshire et al, 1994).

3.1.1.1 Ice Sheet Elevation.

The satellite laser altimeter made three basic measurements: the range between the satellite and the surface footprint, the shape of the return waveform after reflection from the earth surface, and the laser power returned from the surface. The ice sheet elevation for GLAS was measured as the mean surface height of the laser footprint, which is the difference between the satellite height and the range between the satellite and the surface. The satellite height was determined from the orbit and is independent of the laser measurement. The range was measured by calculating the laser pulse travel time to the surface, correcting for atmospheric and instrument effects. The shape of the return waveform was affected by: the

transmitted pulse; the surface height distribution within the footprint; atmosphere scattering; and the receiver. If the transmitted pulse is close to a Gaussian, the surface is a mean slope plus random height variations, and there is no atmospheric forward scattering, the return pulse shape will be very close to a Gaussian. Our test results show that fitting a Gaussian pulse to the waveform and then using the centroid of the Gaussian helped to diminish the effects of non-ideal conditions including irregular surfaces and forward scattering when the fitting used only the gates near the pulse center.

3.1.1.2 Ice Sheet Roughness and Slope.

Our approach is based on the assumption that there is a spectral minimum in surface roughness that lies in the range of a few hundred meters and separates the wind-generated roughness at shorter wavelengths from the undulation generated by basal topography at longer wavelengths. That being the case, we can consider the surface within the footprint as characterized by a mean slope, which is a short segment of the long-wavelength undulations; superimposed on that slope is a large number of wind-generated bumps of short wavelength. Correspondingly, we make two calculations, based on the alternate assumptions of a smooth, linearly sloping surface and a rough flat surface. After more quantitative knowledge is gained of the slope from GLAS, we may be able to calculate the roughness using this.

We assume that the surface is a diffuse (Lambertian) reflector. That is, the emerging radiance is constant for all directions in a hemispherical solid angle. The surface reflectivity is also assumed to be uniform within the 70 m footprint.

Effect of Roughness: We assume that small-scale roughness has a Gaussian distribution, which also implies that there are a sufficient number of bumps within the footprint to justify a statistical approach. Although there is no reason to suppose that this distribution of heights is realistic for the snow dunes and sastrugi that roughen the surface, since they tend to have a regularity of form and size within a small area (Doumani, 1967), there is no quantitative basis for any other assumption. It will require ground-truth experiments to provide a quantitative correlation between surface conditions and the roughness calculated from the GLAS algorithm.

Effect of Slope: For the purposes of algorithm development we assume a linear slope. Because the dominant wavelengths of surface undulations are generally over 10 km (McIntyre, 1986), this should be a good approximation across the 70 m footprint.

Combined Effect: There is no realistic way to ascertain from the shape of a single returned pulse to what extent the pulse-broadening has been caused by the roughness and to what extent by the mean slope, even though the pulse shapes are slightly different in the idealized, theoretical cases, because the distortion caused by deviations from our idealized assumptions will surely be large compared to that slight difference. We therefore made no attempt to separate the two effects; our data product has two numbers stemming from alternate analyses of the same pulse. One will give $\text{Var}(\Delta x)$, calculated on the assumption of roughness alone, and the other will give the mean slope, calculated on the assumption of a tilted, planar surface. Which is more nearly appropriate in a given situation is a matter that can only be determined by reference to ancillary information about the nature of the region observed. See section 3.1.2.2.2. Also see appendix 1 for an explanation for the removal of slope and roughness from the products.

3.1.1.3 Sea Ice Elevation and Roughness

Within each 70-meter GLAS footprint, incident near infrared (NIR) laser energy was reflected to the receiving telescope with a time delay determined primarily by surface elevation and surface roughness (for the moment, we neglect the effect of forward scattering by clouds and aerosols), and intensity determined primarily by reflectivity of the surface and the energy beam pattern incident upon the surface. The average time delay of the return energy gave the average range to surfaces within the footprint, and the temporal variation of return-pulse intensity was a measure of the range distribution within the footprint modulated by local reflectivity and the incident beam pattern. The shape of the return pulse was smoothed by the detection

system, limiting the information that could be retrieved. Moreover, forward scattering of laser energy in transit through the atmosphere increased return-pulse spreading beyond that caused by surface roughness. Consequently, little was to be gained by overly sophisticated algorithms, and our objective was to extract the least ambiguous sets of information, and to identify them as objectively as possible.

The major sea-ice parameters determined from GLAS waveforms include elevation, surface slope and roughness, and surface reflectivity. Surface roughness is a statistical description of the surface, representing its deviation from a smooth reference surface (Ogilvy, 1991). The standard deviation of surface elevations from their mean was a good way to characterize the surface roughness of horizontal surfaces. The reflectance (ratio of reflected energy flux to the incident flux) measured by GLAS can be related to the spectral albedo of the surface (ratio of total upwelling irradiance and the total downwelling irradiance). See appendix 1 for an explanation for the removal of slope and roughness from the products.

3.1.1.4 Land Elevation, Surface Slope and Roughness, and Vegetation Height

Interpretation of land properties from GLAS return pulse waveforms is complicated by the diverse nature of land constituents and the small spatial scale over which these constituents can vary. The possibility of steep surface slopes, large roughness and the potential presence of vegetation and/or cultural features (e.g., buildings, vehicles, structures) within a laser footprint leads to ambiguity in waveform analysis. For the purpose of this document, land slope is considered to be the mean planar slope of the surface across the laser footprint and land roughness is random height deviations of the surface from that mean plane. Land surface relief is the minimum to maximum elevation within the footprint caused by slope and roughness. The land surface is considered to be the surface absent any overlying vegetation (living or dead) or cultural features. The land surface may be composed of solid Earth components (e.g., rock, sand, soil), water (e.g., inland lakes, rivers, inundated areas), snow, or ice.

For footprints lacking vegetation or cultural features, the interpretation of the land surface elevation is like that for ice sheets, sea ice, and oceans. The time history of backscatter energy is a measure of the vertical distribution of intercepted surface area (projected in the direction of the laser vector) weighted by the reflectance of the surfaces at the monochromatic laser wavelength and the spatial distribution of laser energy across the footprint. The recorded waveform is the product of this measure convolved with the temporal character of the transmit pulse, the receiver electronics, and atmospheric scattering. These convolved effects are ideally removed by waveform processing yielding a reflectance- and illumination-weighted surface height distribution. The centroid of that distribution is taken to be the measure of the footprint elevation. As is the case for ice sheets, lacking independent information the slope versus roughness contributions to the surface height distribution cannot be distinguished within the ICESat footprint. End-member, model measures of slope and roughness can be derived assuming no roughness and slope contribution to the pulse spreading, respectively.

For footprints containing vegetation and/or cultural features, the surface height distribution created by slope and/or roughness will be combined with the height distribution of canopy components (living or dead foliage and woody tissue) and cultural features. In areas of low to moderate slope and roughness, experience with small footprint (on the order 10 meter diameter) airborne lidar data have shown that vegetated or urbanized landscapes typically yield multi-modal waveform returns. Each mode, or peak, of the waveform corresponds to footprint constituents differentiated in height. Where sufficient laser energy penetrates the canopy and reaches the underlying ground, a last peak corresponding to the ground surface is acquired in the waveform. Higher peaks correspond to discrete vegetation layers and/or the tops of cultural features. The initial return corresponds to the upper-most detected canopy surface or highest cultural feature. Maximum vegetation or building height within the footprint is readily derived from the time delay between the initial and last returns, where maximum refers to the height at which there is return energy sufficient to be detected (dependent on intercepted area, reflectance and laser spatial energy).

The ability to differentiate the height of discrete components within the footprint decreases as the surface relief, due to slope and roughness, increases and as the footprint size increases. With increasing relief the height distribution of the surface becomes mixed with the height distribution of vegetation or cultural features. This effect is compounded by increasing footprint size. For 70 m ICESat footprints, moderately sloping and/or rough terrain can have surface relief commensurate with the height of overlying vegetation or cultural features, causing these contributions to be unresolvable in the waveform. Furthermore, the canopy height distribution becomes less resolved at larger footprint scales as multiple vegetation layers at various heights become spatially averaged. Finally, the meaning of maximum vegetation height, which pertains to the highest vegetation above the ground at a specific location, becomes ambiguous for large footprints where ground relief can be of the same magnitude as vegetation height. Experience with 100 m diameter SLA footprints and 70 m diameter airborne lidar footprints demonstrates that multi-modal returns are common but it is difficult, without independent knowledge of land cover and surface relief, to confidently assign returns within the waveform to specific terrain components.

As is the case with atmospheric forward scattering, multiple scattering from canopy components will cause increased path length and thus delayed return energy in waveforms from footprints containing vegetation. Multiple scattering of optical energy in canopies is a complex process dependent on wavelength, the amount of transmission through foliage, and the three-dimensional distribution of canopy components. The published literature to date evaluating airborne lidar and SLA canopy waveforms has not incorporated models of multiple scattering, considering the effect on canopy height derivation to be small. Consideration of canopy multiple scattering is beyond the scope of operational ICESat waveform processing, and is more appropriately treated as a research issue.

3.1.1.5 Ocean Elevation

Each clear-weather GLAS return pulse provided estimates of average surface elevation and of surface-height distribution within the corresponding 70-meter footprint, at a rate of 40/second. However, these footprints, in general, covered less than one of the longer ocean waves, and it was necessary to include information from many consecutive footprints to infer sea-surface elevation and wave height. Surface elevation was obtained by averaging the elevation of these many footprints, and the maximum wave height was given by the highest and lowest surface elevations inferred from the all the pulse widths for wavelengths less than twice the footprint diameter. The length of orbit track over which this “averaging” must be done depended on the sea state, and it was possible to calculate this length from the sea-state information that GLAS provided.

3.1.2 Analysis of Waveforms Obtained By Pulsed Laser Altimeters

Pulsed laser altimeters estimate the range to the terrain surface by measuring the round trip time-of-flight of a laser signal. The received signal is spread in time, in part due to the variation of range between the laser firing point and the surface features. For statistically uniform, diffuse surfaces with uniform reflectivity the expected signal at the receiver output can be expressed as the convolution of the surface profile probability density with the flat diffuse target response (Gardner, 1982). For returns from the ocean surface the shape of the backscattered signal is closely related to the height probability density of the specular points within the footprint (Tsai and Gardner, 1982). The following description of the analytic expressions is adapted from (Gardner, 1992).

3.1.2.1 Analytic Expressions For Flat or Uniformly Sloping, Terrain

The geometry of the model is illustrated in Figure 2. The coordinate system is defined by the optical axis of the altimeter and the line from the altimeter (A) to the center of the Earth, which determines the direction of the z-axis. The x-axis lies in the plane defined by z and the optical axis and it is perpendicular to z, and y completes the right hand system. The origin of the coordinate system is at the intersection of the optical axis and the terrain surface (F).

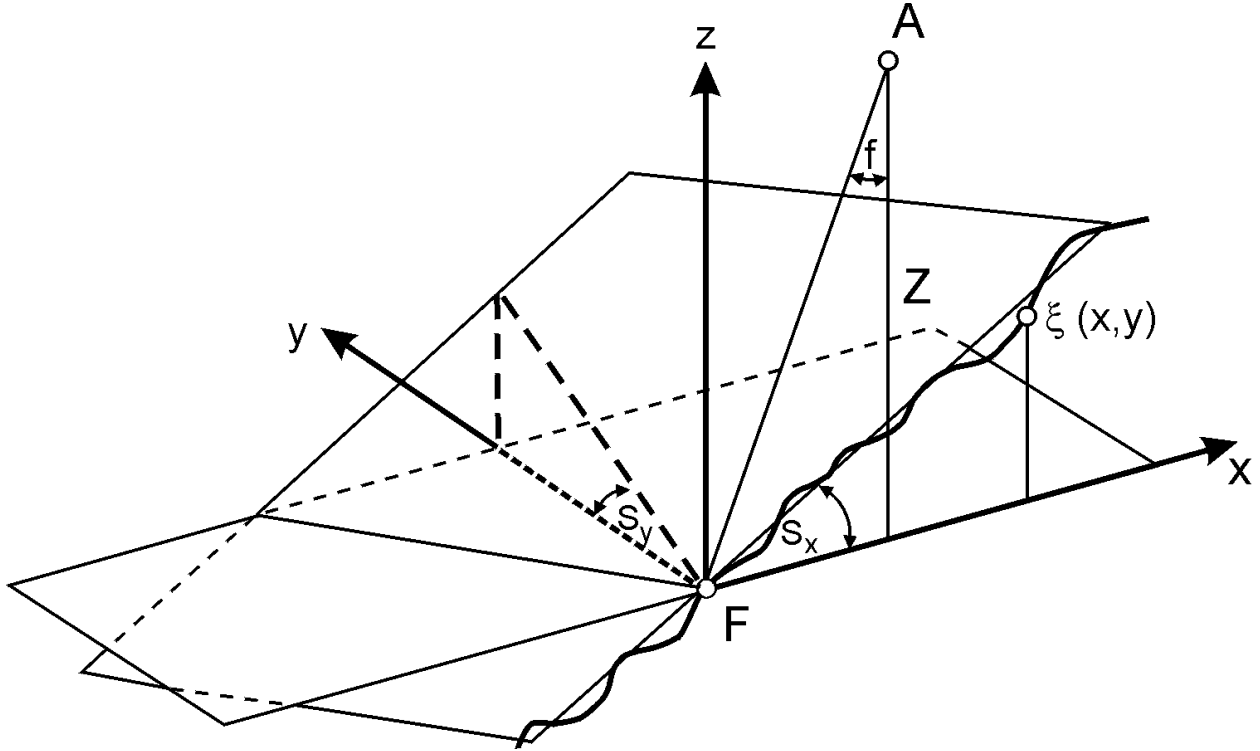


Figure 2 - Generalized geometry of the terrain

The surface profile within the laser footprint is modeled as

$$\xi(\vec{r}) = \xi_0 + \vec{S} \cdot \vec{r} + \Delta\xi(\vec{r}) \quad [1]$$

where $\vec{r} = (x, y)$ is the horizontal position vector on the ground, ξ_0 is a constant offset, $\vec{S} = (S_x, S_y)$ is the mean surface slope within the footprint, and $\Delta\xi(\vec{r})$ is the random microstructure of the surface.

3.1.2.1.1 Diffuse Terrain Types (Land, Snow)

Gardner (1982, 1992) has analyzed the performance of pulsed laser altimeters for sloping, Lambertian (diffuse) terrain with quasi-random surface roughness and uniform reflectivity. He neglected the effect of the forward scattering by clouds and aerosols. By assuming a Gaussian laser beam cross-section he obtained the following analytical expressions for the mean pulse delay and for the RMS pulse width.

The expected mean pulse delay is composed from the propagation delay along the center from the laser beam, the additional delay resulting from the phase front curvature of the diverging laser beam, and the biases caused by the pointing jitter, that is

$$E(T_p) = \frac{2z(1 + \tan^2 q_T)}{c \cos f} \left[1 + \left(1 + 2 \tan^2(f + S_x)\right) \frac{\text{Var}(\Delta f_x)}{2} + \cos^2 f \left(1 + \frac{2 \tan^2 S_y \cos^2 S_x}{\cos^2(f + S_x)}\right) \frac{\text{Var}(\Delta f_y)}{2} \right] \quad [2]$$

where T_p is the propagation delay measured by the pulse centroid time, c is the effective velocity of light (m/s), f is the off-nadir pointing angle of laser beam, S_x is the surface slope in (xz) plane, S_y is the surface slope in (yz) plane, z is the altimeter height above the terrain (m), q_T is the halfwidth divergence angle of the laser beam measured at the $1/\sqrt{e}$ point (rad), Δf_x is the pointing error parallel to the pointing direction, and Δf_y is the pointing error perpendicular to the pointing direction.

The mean-square pulse width is the sum of the effects of the system, surface roughness, beam curvature, off-nadir angle, and surface slope, that is

$$E(s_p^2) = (s_l^2 + s_h^2) + \frac{4\text{Var}(\Delta \xi) \cos^2 S_x}{c^2 \cos^2(f + S_x)} + \frac{4z^2 \tan^2 q_T}{c^2 \cos^2 f} \left[\tan^2 q_T + \tan^2(f + S_x) + \frac{\tan^2 S_y \cos^2 S_x}{\cos^2(f + S_x)} \right] \quad [3]$$

where s_p is the RMS received pulse width(s), s_l is the RMS transmitted pulse width(s), s_h is the RMS width of receiver impulse response(s), $\Delta \xi$ is the surface roughness (m). See appendix 1 for an explanation for the removal of slope and roughness from the products.

3.1.2.1.2 Ocean Surface

The ocean surface is a specular (non-diffuse) reflector. Tsai and Gardner (1982) have derived expressions to compute the mean pulse delay and the RMS pulse width over specular surfaces. To simplify the analysis they assumed Gaussian transmitted laser pulse shape and laser cross section. If the altimeter points at nadir ($f=0$, $\Delta f_x=0$, $\Delta f_y=0$), and Gaussian ocean surface statistics are assumed, the statistics of the returned pulse can easily estimated. Although for large beam divergence angles (larger than 10^{-2} rad) the received waveform is highly asymmetrical, for the small divergence angles used on satellite laser altimeters the waveform is nearly Gaussian. For small beam divergence angles the expected pulse delay is:

$$E(T_p) = \frac{2z}{c} + \frac{2z}{c} (\tan^{-2} q_T + 2S^{-2})^{-1} \quad [4]$$

where $S = \text{magnitude of } \vec{S}$.

Equation 4 differs from the reflection from the diffuse surface (equation 2) only by the presence of the S^{-2} term. Upon reflection from the ocean surface, the laser cross section is modified by the distribution of the surface slopes and the S^{-2} term accounts for this modification. This additional delay will introduce a small error into the ocean surface elevation. More research needs to be undertaken to determine the size of this error and its effect.

The RMS width of the received pulse is:

$$E(s_p^2) = (s_l^2 + s_h^2) + \frac{4}{c^2} \Delta \xi^2 + \frac{4z^2}{c^2} (\tan^{-2} q_T + 2S^{-2})^{-2} \quad [5]$$

If the beam divergence is of the order of 10^{-3} rad or smaller, the last term will be approximately $(4z^2/c^2)\tan^4 q_T$. Then the surface roughness can be computed from the RMS pulse width of the return signal and known system parameters. Tsai and Gardner also derived expression for non-Gaussians ocean surface using the skewness coefficient to describe the non-Gaussian behavior. Due to the complex nature of the ocean returns the errors in the mean elevation and the significant wave height computed from individual returns can be quite large. To reduce the errors several waveforms should be averaged or “stacked” as it is recommended in 3.1.1.5.

3.1.2.2 Algorithms Derived From the Analytical Expressions

Algorithms were derived from the analytical expressions to compute parameters describing the changes in surface elevation within the laser footprint (for example roughness, slope). See appendix 1 for an explanation for the removal of slope and roughness from the products.

3.1.2.2.1 Ice Sheet Elevation

As expected, the return closely resembled a Gaussian and therefore a Gaussian pulse was used to fit the waveform. The centroid of the Gaussian pulse was used to calculate the range to the mean surface. This range was then corrected for atmospheric delays using algorithms defined in the GLAS atmospheric correction ATBD, and the effect of time-varying tides removed using algorithms in the GLAS tide ATBD. Using this corrected range, the satellite position above the ellipsoid, and the off-nadir pointing angle; the surface elevation was calculated using the algorithms defined in the GLAS laser location and surface profile ATBD.

3.1.2.2.2 Ice Sheet Roughness/Slope

Rough, Flat Surface: For horizontal surfaces $\vec{S} = \vec{0}$ and equation 1 becomes

$$\xi = \Delta\xi + \xi_0 \quad [6]$$

With $S_x = 0$ and $S_y = 0$ from equation 3 we get

$$E(s_p^2) = (s_l^2 + s_h^2) + \frac{4Var(\Delta\xi)}{c^2 \cos^2 f} + \frac{4z^2 \tan^2 q_T}{c^2 \cos^2 f} (\tan^2 q_T + \tan^2 f) \quad [7]$$

Satellite laser altimeters have a small off-nadir pointing angle and beam divergence. Therefore the third term in equation 7 can be neglected and we obtain

$$E(s_p^2) = (s_l^2 + s_h^2) + \frac{4Var(\Delta\xi)}{c^2} \quad [8]$$

From equation 8 we finally have

$$sdev(\xi) = [Var(\Delta\xi)]^{1/2} = \frac{c}{2} (E(s_p^2) - s_l^2 - s_h^2)^{1/2} \quad [9]$$

By using this formula the RMS surface roughness of a horizontal surface can be estimated from the received pulse width and from the known system parameters of the GLAS altimeter.

Sloping, Smooth Surface:

Set $Var(\Delta\xi) = 0$, and $f = 0$, from equation 3, we have

$$E(s_p^2) = (s_l^2 + s_h^2) + \frac{4z^2 \tan^2 q_T}{c^2 \cos^2 f} (\tan^2 q_T + \tan^2 S_x + \tan^2 S_y) \quad [10]$$

Since,

$$\tan^2 S_x + \tan^2 S_y = \tan^2 S \quad [11]$$

and for GLAS, q_T is on the order of 10^{-5} radians, we can ignore the $\tan^2 q_T$ term and write,

$$E(s_p^2) = (s_l^2 + s_h^2) + \frac{4z^2 \tan^2 q_T}{c^2} \tan^2 S \quad [12]$$

Then,

$$\tan S = \frac{c}{2z \tan q_T} \left(E(s_p^2) - (s_l^2 + s_h^2) \right)^{1/2} \quad [13]$$

or,

$$S = \tan^{-1} \left[\frac{c}{2z \tan q_T} \left(E(s_p^2) - (s_l^2 + s_h^2) \right)^{1/2} \right] \quad [14]$$

3.1.2.2.3 Sea Ice Elevation and Roughness

Sea ice can be modeled by horizontal, randomly rough Lambertian (diffuse) surfaces, so equation 9 of the previous section applies.

In general, a sea-ice footprint will contain either a mixture of rough and smooth ice (or open water) or predominantly smooth ice (or open water). Less frequently, an entire footprint could be occupied by rough ice, or an iceberg, glacier, land ice, or land could occupy all or part of the footprint. In general, the average elevation of smooth or randomly rough ice (or open water) will be represented by the centroid of the latest, approximately Gaussian peak in the return pulse. Other surfaces in the footprint will have shorter ranges and their effect on return-pulse shape will be determined primarily by their surface height distribution. In some cases, such as when the smooth top of an iceberg fully occupies the footprint, the latest peak will not be smooth sea ice. However, this should be readily identifiable by its height above the geoid.

The key products to be derived for each GLAS "sea-ice" footprint were:

- a. Average elevation of sea ice or open water
- b. Average elevation of features such as ice bergs that partly or entirely occupy a footprint
- c. Average reflectance

The sea-ice elevations will help improve the geoid, and surface roughness strongly influences both heat and momentum exchanges between the atmosphere and the ice. The reflectance is indicative of sea-ice albedo, which also affects energy exchange. Recent work with satellite radar-altimeter data (Peacock et al, 1998) indicates the possibility of estimating sea-ice freeboard, a proxy indicator of thickness, by comparing elevations of open-water leads with those of the intervening ice. Data from GLAS was better suited to this application because of their small footprint. Even if identification of open-water waveforms is difficult, it might be possible to identify leads by the abrupt change in elevation between lead and sea ice. This is a research area, and is beyond the scope of a sea-ice algorithm, but if successful it would represent a major enhancement to our ability to monitor sea ice.

3.1.2.2.4 Land Elevation, Surface Slope and Roughness, and Vegetation Height

Due to the potential complexity of land returns, the waveform processing methodology uses an approach that characterizes the return by fitting Gaussian distributions to each mode (i.e., peak) identified within the waveform. Each Gaussian distribution is described following the methodologies defined in 3.1.2.2.1 and 3.1.2.2.2 for ice sheets, with the centroid equivalent to the mean reflectance- and illumination-weighted elevation and the variance a measure of pulse spreading. Interpretation of those fitted distributions in terms of elevation, surface slope and roughness, and vegetation height then depends on the character of the return (uni-modal or multi-modal) and an assumption, or independent knowledge, of land cover type within the footprint. For uni-modal returns thought to be from footprints lacking vegetation or cultural features the interpretation is straightforward. The centroid is the mean surface elevation and the variance is due to the combined effects of surface slope and roughness that can be modeled as end-member cases as for ice sheets. Uni-modal returns thought to be from footprints containing vegetation or cultural features are more ambiguous since the contributing components can not be differentiated in height. The centroid in this case is the mean elevation of all intercepted components and its relationship to the surface elevation depends on the unknown density and spatial organization of overlying vegetation and cultural features. Similarly, the Gaussian variance is due to the height distribution of all intercepted components, not just surface slope and/or roughness. For multi-modal returns an assumption is made that the last peak in the waveform corresponds to the surface and that earlier peaks correspond to overlying vegetation and/or cultural features. The centroid and variance of the Gaussian distribution fit to the last peak are then used to define the mean surface elevation and the pulse spreading due to surface slope and/or roughness. The maximum height of overlying vegetation, or cultural features, is then taken to be the distance from the leading edge of the initial return in the waveform to the centroid of the last return.

The assumption that the last peak in multi-modal land returns corresponds to the surface is useful for operational processing of the waveforms, but it is recognized that the assumption is in error in a variety of circumstances:

- a multi-modal return can result if the surface within the footprint is composed of multiple discrete surfaces separated in elevation, as would be the case with surfaces offset by a scarp or cliff for example; the last peak in this circumstance corresponds to the lowest of the discrete multiple surfaces,
- dense vegetation everywhere across a footprint may prevent sufficient laser illumination from reaching the surface causing there to be no detectable surface return; the last peak in this circumstances corresponds to the lowest illuminated vegetation layer,
- the last peak may be a composite of low vegetation and the surface (e.g., a low-lying under story or shrub layer), causing the same ambiguities as described above for composite uni-modal returns, and
- a footprint could fall entirely on a large, complex cultural feature (e.g., large building with multi-level roof); the last peak in this circumstance corresponds to the lowest part of the cultural feature.

Such circumstances are likely to be rare. Assessment of the correspondence between last peaks and the surface is beyond the scope of operational ICESat waveform processing, and is more appropriately treated as a research issue.

The approach defined for land assumes that all the reflecting components within the footprint behave as Lambertian (diffuse) scatterers. Water surfaces, foliage, and some cultural features violate the assumption of Lambertian scattering. However, lacking complete knowledge of the proportion and distribution of components in the footprint, the effects of non-Lambertian scattering cannot be established. The assumption of Lambertian scattering is a practical approximation of the potentially

complex character of land footprints. See appendix 1 for an explanation for the removal of slope and roughness from the products.

3.1.2.2.5 Ocean Elevation

The algorithm for ocean products infers the average elevation (E) of a footprint, and the return-pulse width (above some threshold - initially the noise floor, but to be adjusted after launch) as the elevation spread ($E_{\max} - E_{\min}$) inside the footprint. In general, the 70-m footprint covers very few waves, often one or less. Consequently, it was necessary to average many values of E to obtain the mean sea-surface elevation over the corresponding length of orbit track. As an example: Assume that E varies by plus or minus H meters because of the waves. $H=1$ would probably correspond to either a high sea state or longer waves or swell with amplitude of about one meter. If the variability of E is random, then the average elevation of 100 consecutive footprint elevations has wave-induced errors, $\Delta E = 0.1$ meters, appropriate to 2.5 seconds of data, or about 16 km of orbit track. Although this capability is poorer than that of satellite radar altimeters, it may offer improved information over specific regions, such as coastal regions and at high latitudes, and for geodesy. Moreover, it may be useful in assessing radar-altimetry errors associated with wave shape. One concern is the possibility of waves of appropriate length being aliased with the footprint spacing to introduce a bias to the average value of E .

Average elevation of the footprint (E) will be obtained from the centroid of the best-fit Gaussian to the return waveform (Section 4.1.3.11). E_{\max} and E_{\min} will be inferred from the timing of the start and end thresholds of the return waveform, with the option of using similar information from the best-fit Gaussian if actual GLAS data reveal significant problems with forward scattering amplifying the tail of the return waveform. Section 4.1.3.4 provides details of threshold tracking.

The total area beneath the return waveform between the start and end thresholds (A) will be used to infer the reflectivity of the surface. Values of E , E_{\max} , E_{\min} , and A will be archived for each footprint location, and they will be strongly affected by local sea state. A mean elevation (E_m) over 1 full second will also be calculated as an average of all N values of E acquired during the second, and both E_m and N will be archived at the full GLAS data rate. The value of N will indicate regions of patchy cloud cover.

Within the one-second window, the extreme values of E_{\max} and E_{\min} give the full range of wave amplitudes for short wavelengths. However, a better representation of waveheight, and one more comparable to that derived from radar-altimeter data, could be obtained from the width of a composite return pulse formed by stacking many adjacent waveforms. Consequently, after the launch of GLAS, the science team will investigate a level 3 OCEAN product derived from many ($N+1$) footprints to take account of the wave height. Average values of E will be determined for orbit segments of fixed length, say 10 km, with final selection based on experience with actual data. The averaging process will require temporary storage of ($N+1$) waveforms: the current waveform plus those for the preceding and subsequent $N/2$ footprints. The waveforms will be "stacked" to yield a composite waveform appropriate to the 10-km segment of orbit track. This composite waveform will be used to provide an alternate estimate of average elevation (from the centroid of its best-fit Gaussian) and an estimate of RMS wave height from equation 9 in Section 3.1.2.2.2. From the RMS wave height the Significant Wave Height (SWH) can be computed. The SWH is defined as the average of heights (from crest to trough) the highest one-third of the waves observed at a point. It is approximately equal to four times the RMS wave height (Tsai and Gardner, 1982). This would yield values of average E at the full rate of 40/sec, each with its own value of RMS wave height depending on sea state.

3.1.2.3 Skewness and Kurtosis

Skewness characterizes the degree of asymmetry of a distribution around its mean and kurtosis measures the relative peakedness and flatness of a distribution (Press et. al., 1992). Skewness and kurtosis values can indicate the shape of a waveform.

Skewness and kurtosis are defined by the following equations (Leon-Garcia, 1989, p148 and Press et. al. 1992, p612)

$$skewness = \frac{1}{\sigma^3} \frac{\sum_{i=start}^{i=end} (i - mean)^3 w[i]}{\sum_{i=start}^{i=end} w[i]} \quad [15]$$

$$kurtosis = \frac{1}{\sigma^4} \frac{\sum_{i=start}^{i=end} (i - mean)^4 w[i]}{\sum_{i=start}^{i=end} w[i]} - 3 \quad [16]$$

Where $w[i]$ is the power of the i th gate of a waveform. Start and end are the start and end gate of the signal in a waveform. Mean and σ are the mean and standard deviation of the waveform,

$$mean = \frac{\sum_{i=start}^{i=end} i w[i]}{\sum_{i=start}^{i=end} w[i]} \quad [17]$$

And

$$\sigma^2 = \frac{\sum_{i=start}^{i=end} (i - mean)^2 w[i]}{\sum_{i=start}^{i=end} w[i]} \quad [18]$$

For a normal distribution, the skewness and kurtosis are equal to zero. Skewness and kurtosis were calculated from the portion of the waveform between signal begin and signal end, which were found by using a threshold determined by n times the standard deviation of the noise (see `beg_nsig` and `end_nsig` in appendix 2).

3.2 Mathematical Formulation

3.2.1 Development of Equations

Since the transmitted pulse is Gaussian, if the surface topography is Gaussian, the return should also be Gaussian. We can represent the return mathematically as a sum of Gaussians plus a bias. Over the oceans, sea ice, and most of the ice sheets, the return is a single Gaussian. Over land and more complicated ice sheet regions, there may be multiple distinct peaks within the footprint (such as a tree), that will show up as multiple peaks in the return. Therefore the modeled waveform is defined as

$$w(t) = \varepsilon + \sum_{m=1}^{N_p} W_m, \quad W_m = A_m e^{-\frac{(t-t_m)^2}{2\sigma_m^2}} \quad [19]$$

where

$w(t)$ is the amplitude of the waveform at time t
 W_m is the contribution from the m th gaussian

- N_p is the number of gaussians found in the waveform
- A_m is the amplitude of mth gaussian
- ε is the bias (noise level) of the waveform
- t_m is the gaussian position
- σ_m is the 1/e half-width (standard deviation) of the mth gaussian

Nonlinear least squares was used to compute the model parameters (the ε , A_m , t_m , and σ_m in equation 19) by fitting the theoretical model to the observed waveform. This is a standard procedure detailed in many references (Bevington and Robinson, 1992, Menke 1989, Press et al, 1986, Zwally et al, 1990). The development here follows Menke 1989, modified to include weights and a priori error estimates on the parameters as in Zwally 1990.

The measured waveform, consisting of N samples, is

$$\mathbf{p} = [p_1, p_2, \dots, p_N]^T \quad [20]$$

The model waveform, written in discrete form, is

$$\mathbf{w} = [w_1, w_2, \dots, w_N]^T \quad [21]$$

The vector of the M model parameters (the ε , A_m , t_m , and σ_m in equation 19) is

$$\mathbf{c} = [c_1, c_2, \dots, c_M]^T \quad [22]$$

where $M = 3N_p + 1$.

The matrix of derivatives of the model waveform with respect to the parameters is

$$\frac{\partial \mathbf{w}}{\partial \mathbf{c}} = \begin{bmatrix} \frac{\partial w_1}{\partial c_1} & \frac{\partial w_1}{\partial c_2} & \dots & \frac{\partial w_1}{\partial c_M} \\ \frac{\partial w_2}{\partial c_1} & \frac{\partial w_2}{\partial c_2} & \dots & \frac{\partial w_2}{\partial c_M} \\ \vdots & \vdots & \ddots & \vdots \\ \frac{\partial w_N}{\partial c_1} & \frac{\partial w_N}{\partial c_2} & \dots & \frac{\partial w_N}{\partial c_M} \end{bmatrix} \quad [23]$$

Given an estimate of the M parameters, C^i , the first-order Taylor series expansion of w around w^i is

$$w_n^{i+1} = w_n^i + \sum_{m=1}^M \frac{\partial w_n^i}{\partial c_m} \delta_m \quad [24]$$

where superscript i refers to the i^{th} iteration and

$$\delta_m = c_m^{i+1} - c_m^i \quad [25]$$

If we also define the difference between the measured and i^{th} estimate of the waveform,

$$\mathbf{B} = \mathbf{p} - \mathbf{w}^i \quad [26]$$

and the matrix \mathbf{A} by

$$A_{nm} = \partial w_n^i / \partial c_m \quad [27]$$

then we can write

$$\mathbf{A}\Delta = \mathbf{B} \quad [28]$$

Since \mathbf{A} may not be square, we cannot simply multiply both sides of this equation by \mathbf{A}^{-1} to get Δ . Instead, multiply both sides first by \mathbf{A}^T :

$$\mathbf{A}^T \mathbf{A} \Delta = \mathbf{A}^T \mathbf{B} \quad [29]$$

and then by $[\mathbf{A}^T \mathbf{A}]^{-1}$, to get

$$\Delta = [\mathbf{A}^T \mathbf{A}]^{-1} \mathbf{A}^T \mathbf{B}. \quad [30]$$

We can rewrite this equation as

$$\Delta = [\mathbf{A}^T \mathbf{W} \mathbf{A} + \mathbf{V}_0]^{-1} \mathbf{A}^T \mathbf{W} \mathbf{B} \quad [31]$$

to incorporate weights and a priori values. Here the weight matrix is

$$\mathbf{W}_{ij} = w_{t_i} \delta_{ij} \quad [32]$$

and the a priori matrix is

$$[\mathbf{V}_0]_{jk} = w_{t_{c_k}} \delta_{jk} \quad [33]$$

where w_{t_i} is the weight for the i^{th} observation, $w_{t_{c_k}}$ is the a priori weight for the k^{th} parameter c_k , and δ_{ij} is the Kronecker delta,

A new set of parameters can then be calculated from

$$\mathbf{c}^{i+1} = \mathbf{c}^i + \Delta \quad [34]$$

The covariance matrix, $\text{cov}(s_{ij}^2)$ and the variance s^2 can be calculated from

$$\text{cov}(\sigma_{ij}^2) = [\mathbf{A}^T \mathbf{W} \mathbf{A} + \mathbf{V}_0]^{-1} \quad [35]$$

and

$$s^2 = \frac{\sum_{n=1}^N (w_n - p_n)^2}{N - M}, \quad [36]$$

where M is the number of parameters.

The derivatives of the modeled waveform with respect to the parameters:

$$\begin{aligned} \frac{\partial w}{\partial \varepsilon} &= 1 \\ \frac{\partial w}{\partial A_m} &= \exp\left[-\frac{(t - t_m)^2}{2\sigma_m^2}\right] \\ \frac{\partial w}{\partial t_m} &= \frac{A_m(t - t_m)}{\sigma_m^2} \exp\left[-\frac{(t - t_m)^2}{2\sigma_m^2}\right] = \frac{A_m(t - t_m)}{\sigma_m^2} \frac{\partial w}{\partial A_m} \\ \frac{\partial w}{\partial \sigma_m} &= \frac{(t - t_m)}{\sigma_m} \frac{\partial w}{\partial t_m} \end{aligned} \quad [37]$$

3.2.2 Procedure

The symbols used in this section are defined in appendix 2.

The fitting steps used are as follows:

1. Estimate the model parameters
2. Compute a new value for w using the first order Taylor expansion, Eq. 24
3. Compute a correction to the current estimate of the parameters, Eq. 31
4. Update the parameter estimate, Eq. 34
5. Repeat steps 2-4 until some exit criterion is satisfied
6. Compute the covariance matrix and variance, Eq.s 35 and 36

The capability to use in the fitting procedure only that portion of the waveform within $n * \sigma_m$ of the peak(s) needs to be allowed for.

For each iteration step, the following constraints apply:

1. $\sigma_m > 0$ and $|\delta\sigma_m| < \delta\sigma_{m,max}$
2. $\delta t_m < \delta t_{m,max}$
3. $A_m > 0$ and $\delta A_m < \delta A_{m,max}$
4. $\varepsilon > 0$, $\delta\varepsilon < \delta\varepsilon_{max}$

where

$$\begin{aligned}\delta\varepsilon_{max} &= \text{anc07\%D_MAXDELTAS_Nn} * \text{CurrentNoiseParameter} \\ \delta A_{m,max} &= \text{anc07\%D_MAXDELTAS_An} * \text{CurrentAmplitudeParameter} \\ \delta t_{m,max} &= \text{anc07\%D_MAXDELTAS_Ln} \\ \delta\sigma_{m,max} &= \text{anc07\%D_MAXDELTAS_Sn} * \text{CurrentSigmaParameter}\end{aligned}$$

Two fits were performed for each waveform: one for land referred to as alternate, and the other for ice, seaice, and ocean referred to as standard. The maximum number of peaks (N_p) allowed for the standard fit is two, and for the alternate fit is six.

The criteria for ending the fitting loop are:

1. Number of iterations ≥ 3 , $|\delta\varepsilon_{mean}| < \delta\varepsilon_{check}$, $|\delta t_m| < \delta t_{m_check}$, $|\delta\sigma_m| < \delta\sigma_{m_check}$, and $|\delta A_m| < \delta A_{m_check}$.
The incremental change in each parameter is less than a given percentage.
or
2. Number of iterations $> \text{MaxIter}$.

4.0 Algorithm Implementation

The waveform processing algorithms were adapted from methods developed for the analysis of waveforms acquired from

- the first and second flight of the Shuttle Laser Altimeter
- satellite radar altimeters
- aircraft laser altimeters over land and ice sheet surfaces.

The major goals of the algorithm are to

- characterize the surface reflectivity, roughness, variability, and slope
- calculate the surface elevation

The GLAS instrument recorded signals from four types of surfaces – ice sheets, sea ice, land, and ocean. The science requirements differ for these different surfaces. Except for normalization, the algorithms

described here are the same for all surface types; the differences in the final results come from use of different sets of parameters to drive these algorithms. Two sets of parameters were used, one that satisfied the land processing requirements and one that satisfied the ice sheets, sea ice, and ocean requirements. Under normal mode of operation the algorithms are run twice, once with each set of parameters. The processing software has the option of processing all data, only ice sheet, sea ice, and ocean data, or only the land data using just the appropriate parameter set(s).

There are four regional level 2 elevation products; one each for ice sheet (GLA12), sea ice (GLA13), land (GLA14) and ocean (GLA15). Four different surface masks are used to define what data goes on each level 2 elevation product. It is possible for these masks to overlap, so the data will be on more than one level 2 product. The definition of each of the parameters on the level 2 products, as defined in section 5.0, is dependent on the surface type.

4.1 Outline of the Procedure

- Characterize the transmitted pulse and calculate time for beginning of range calculation
- Characterize the received waveform to determine if there is a signal and to determine the point on the waveform to be used to estimate the range and the preliminary footprint location on the Earth.
- Interrogate the database to determine the type(s) of surface at the footprint location.
- Smooth the waveform and determine initial estimates for the waveform parameters.
- Normalize the waveform, and the estimated noise and peak amplitudes for ice sheet, sea ice, and ocean data processing.
- Fit the waveform using the procedure developed in section 3.2 and described below.
- Un-normalize the solution noise and peak amplitudes for ice sheet, sea ice, and ocean data processing.
- Calculate range to mean surface and surface elevation distribution
- Calculate atmospheric delay and tidal values
- Calculate a corrected range to the mean surface correcting for atmospheric delay and instrument effects
- Correct time for travel time
- Calculate precise geolocation and mean surface elevation
- Apply the tides to the mean surface elevation
- Calculate region specific parameters

The results of this waveform processing will then be used to calculate the global level 1b elevation product and the level 2 region-specific products defined in section 5.

4.1.1 Input Variables

Parameters input from ancillary file

Unless noted each parameter has two values – one for land processing, and one for ice sheet, sea ice and ocean processing (parameters used only for the transmitted pulse have only one value). Recognizing the potential complexity of land returns, land processing parameters were designed to achieve waveform fitting that preserved all peaks inherently present in the waveform. In particular, criteria was established that minimized removal of waveform peaks by smoothing, editing, or merging.

For tables defining parameters input from ancillary files and from the data stream, see appendix 2.

Variables from ancillary sources

- POD: precision orbit data
- PAD: precision attitude data
- Surface identifier grid

Figure 3 depicts the overall characterization of the transmitted and received pulse waveforms.

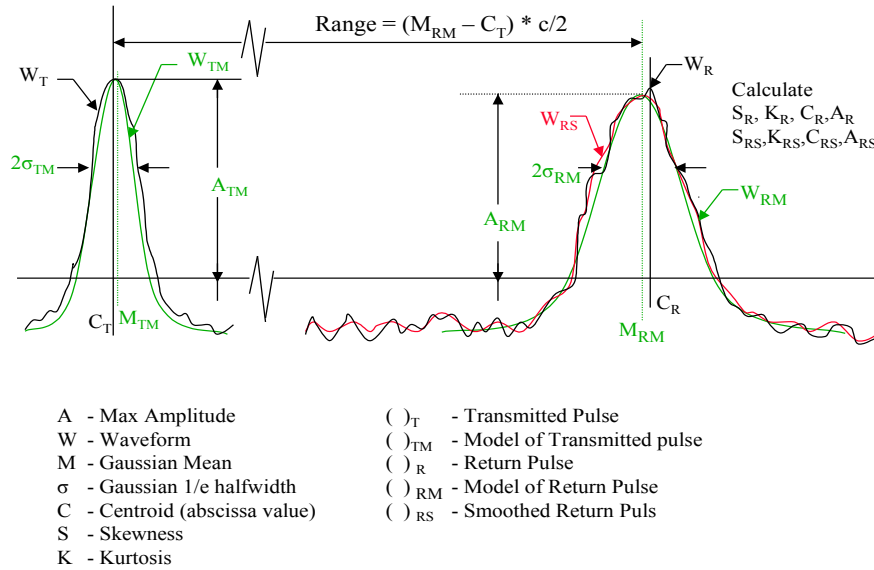


Figure 3 - Characterization of transmitted and received pulse waveforms

4.1.2 Transmit Pulse Characterization

The transmitted pulse is well represented by a single Gaussian with a nearly zero baseline, and its characteristics were calculated along with the parameters from a single-peak Gaussian fit. All abscissa values are calculated relative to the laser fire command time. This is time that the digitizer is started.

- Transmitted Pulse
 - Centroid, C_T
 - Skewness, S_T
 - Max Amplitude, A_T
 - Area under the pulse
- Gaussian Fit to transmitted pulse
 - Mean, M_{TM} , in ns from the beg of the digitizer
 - Pulse 1/e halfwidth (σ_{TM}), (e =base of natural logs)
 - Amplitude of the peak, A_{TM}
 - Standard deviation of fit

The time from which the range will be calculated is the time corresponding to M_{TM} , T_{TM}

$$T_{TM} = T_p + (M_{TM} - T_p) \quad [41]$$

4.1.3 Received Pulse Characterization

This characterization will be done using two sets of input parameters, one for land and one for other regions.

4.1.3.1 Normalize the Abscissa – I.E., Convert From Gate Number To Time.

For gates 1 to Ngates-N:

$$t(n) = \Delta T_{\text{hires}} * ((Q-1)/2 + Q * (n-1)) \text{ where } n = \text{gate number.} \quad [42]$$

For gates Ngates-N+1 to Ngates:

$$t(n) = \Delta T_{\text{hires}} * (Q * (Ngates-N) + (P-1)/2 + P * (n-Ngates+N-1)) \quad [43]$$

N = number of gates using the P compression ratio

Q = first compression ratio

P = second compression ratio

ΔT_{hires} = resolution in ns of the highest resolution gate possible (nominally 1 ns)

note: at the end of this normalization, the time array is referenced to 0 at gate 1 of the digitized waveform before compression. When R type compression is used, it is the same as P=Q and N=Ngates.

4.1.3.2 Calibrate the Waveform

The waveform amplitudes are converted from raw counts to volts using a conversion table (from anc07 - see appendix 3). This table is recorded in the file header of the product.

4.1.3.3 Determine the Reference Range, Range_ref

The reference range, Range_ref, is defined as the time difference in ns between the center of the transmitted pulse, T_{TM} , and the last gate of the received pulse telemetered (farthest from the spacecraft).

$$\text{Range_ref} = T_{\text{ngates}} - T_{\text{TM}}$$

Where T_{ngates} = time in ns from the beginning of the digitizer to the gate, ngates.

4.1.3.4 Determine the Preliminary Range (Range_pre)

The preliminary range is defined as the range value associated with the threshold crossing farthest in range from the spacecraft. First find the index, i, that corresponds to the first time, $t(i)$ the waveform crosses a threshold value from the far end such that

$$Wf(t_i) > \text{Noise_ob} + \text{Nsig} * \sigma_{\text{noise_ob}} \quad [44]$$

Then linearly interpolate between $t(i)$ and $t(i-1)$ to calculate the exact time in ns from the beginning of the waveform for this threshold crossing, t_{th} . Then calculate T_{TH} , the value in ns from the beginning of the digitizer of this threshold crossing,

$$\begin{aligned} T_{\text{TH}} &= T_{\text{ngates}} - (t(\text{ngates}) - t_{\text{th}}) \\ \text{Range_pre} &= T_{\text{TH}} - T_{\text{TM}} \end{aligned} \quad [45]$$

Note - t is measured from the beginning of the received waveform, and T is measured from the start time of the digitizer. Figure 4 shows these definitions graphically.

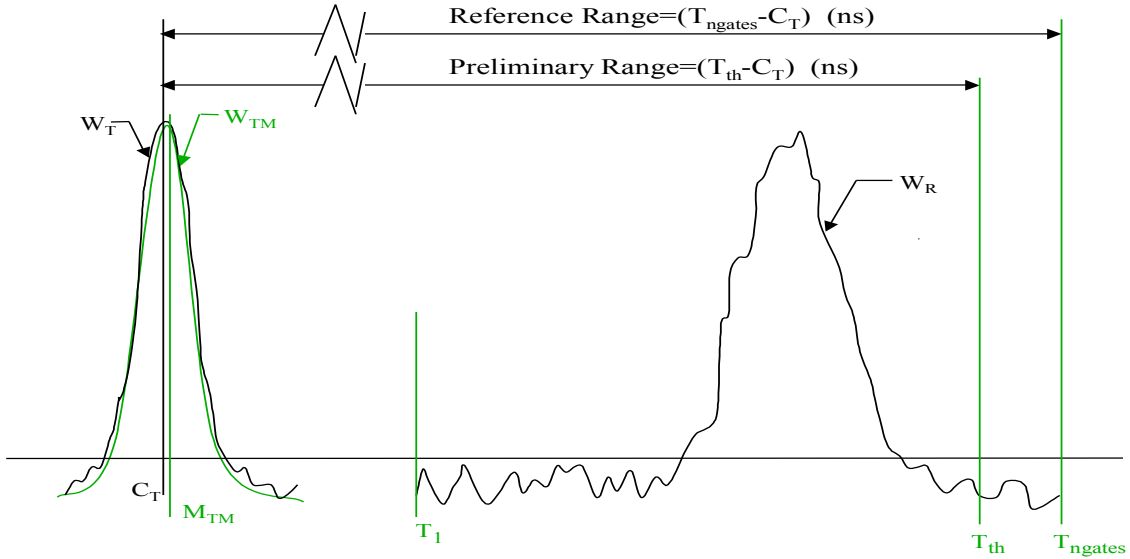


Figure 4 - Definition of Reference and Preliminary Ranges

4.1.3.5 Determine the Preliminary Range Correction

$$\text{Range_pre_cor} = \text{Range_ref} - \text{Range_pre} \quad [46]$$

4.1.3.6 Time Calculation

Each shot is uniquely time tagged using the fire command time (FireAck), the GPS time (GPSt), and GPS acknowledge time(GPSAck).

There is a unique FireAck time for each shot i telemetered with the associated waveform. The GPS time, GPSt, is sampled once every 10 seconds and at the GPS sample time the same clock that is linked to the FireAck time is latched to provide a GPSAck tag. So the basic time tag equation is for each shot:

$$\text{GPSshotTime}(i) = \text{GPSt}(j) + (\text{FireAck}(I) - \text{GPSAck}(j)) \quad [47]$$

Where:

- GPSshotTime(i) is the GPS time for shot i .
- GPSt(j) is the GPS time for the smallest positive (FireAck(I) - GPSAck(j)). i.e. the last GPS time just before shot i .

The time at which we need to evaluate the orbit and attitude is referred to as the ground-bounce time, T_G , or the time at which the signal reached the ground. This is calculated by correcting GPSshotTime (i) for the time it takes to travel to the ground using Range_pre.

$$T_G(i) = \text{GPSshotTime}(i) + \text{Range_pre} / 2 \quad [48]$$

The times on the data products as discussed in section 5.0 are UTC times. These are calculated from the GPS times by correcting for the leap seconds using a table to be supplied by the science team. The times on the data products, T_{out} , of GLA05, 06, and 12-15 are the transmit time in the UTC time frame.

$$T_{out}(i) = \text{GPSshotTime}(i) + T_{cor_gps_to_utc} \quad [49]$$

Where $T_{cor_gps_to_utc}$ is the time correction from GPS to UTC

4.1.3.7 Geolocate the Footprint

Determine the geodetic latitude and longitude of the center of the laser footprint. The footprint location is a function of the spacecraft orbit and attitude and the range. The exact equations used to do the geolocation are found in the Precision Attitude Determination (PAD) Algorithm Theoretical Basis Document (ATBD), the Precision Orbit Determination (POD) ATBD, and the Footprint Location and Surface Profile ATBD.

The attitude data will be at the shot rate (40/sec). A unique index number will be on each attitude record that will correspond to the same index number on each of the GLAS standard products. The attitude data need to be merged using that index number. The POD file gives the sub-satellite (nadir) location of the laser in GPS time. The orbit needs to be interpolated from the POD file at T_G . Range_pre is then used in the geolocation algorithms to determine the location (Lat_pre_uncor and Long_pre_uncor), and the surface elevation (elev_pre_uncor). Range_pre is a preliminary range - it is not corrected for atmospheric delays.

4.1.3.8 Determine Surface Identifier from Regional ID Grid

Find the region ID grid nodes surrounding the footprint geolocation.

If any of the nodes indicate land	THEN $I_{land} = 1$
If any of the nodes indicate ocean	THEN $I_{ocean} = 1$
If any of the nodes indicate ice sheet	THEN $I_{icesheet} = 1$
If any of the nodes indicate seaice	THEN $I_{seaice} = 1$

4.1.3.9 Check Saturation

In order to quantify the degree of saturation, we provide two parameters, called the saturation index and the percent saturation. The saturation index is equal to the number of 1 nsec waveform samples above a saturation threshold, which is a function of receiver gain. The percent saturation is computed by the saturation index times 100 divided by the total number of 1 nsec waveform samples within the received pulse waveform (its duration). This is essentially the percentage of the echo pulse width that is distorted. For ice sheet, sea ice and ocean products the duration used is the time interval between the standard fit signal begin and signal end. For the land product the duration is the time interval between the alternate fit signal begin and signal end. i_{satNdx} is the count of gates that are greater than or equal to a threshold (i_{sat_th} , see table 4-1) that is determined by the received gain.

Table 4-1 Threshold for saturation index

gain _{rec}	i_sat_th	gain _{rec}	i_sat_th	gain _{rec}	i_sat_th
<= 8	30	14	218	20-22	234
9	109	15	224	23-24	235
10	149	16	228	25	236
11	177	17	231	26	237
12	196	18	232	27	238
13	209	19	233	>= 28	239

4.1.3.10 Calculate Noise Level

If noisecal is set then:

Calculate mean value of the whole waveform $Wf(t)$ (Wf_mean) Calculate the noise as the mean of $Wf(t)$ for an input number of gates, ngt_noise , that are below Wf_mean starting at the end of the waveform farthest from the satellite. Calculate σ_noise as the standard deviation in $Wf(t)$ for these same gates.

If noisecal is not set then:

$\sigma_noise = \sigma_{noise_ob}$
Noise = Noise_ob

4.1.3.11 Smooth the Waveform and Check For A Viable Signal

Two smoothed waveforms are produced: one for alternate parameters, and one for standard parameters.

Input: $wf(t)$

Filter_ob: the filter at which the instrument algorithm found the signal
anc07

Start at the filter width given in anc07, but no smaller than the width of the smallest on board filter, Filter_1 (4 ns) and redo this step incrementing the filter size through filter_ob until a signal region is found. If no signal region is found then stop processing the waveform and set flag_signal=1, otherwise set flag_signal=0.

Loop Begin

Smooth the waveform using a Gaussian filter with sigma equal to 1/2 of the two-sigma filter width given in anc07 (fltrWdMin). For samples where the time between contiguous abscissa values is greater than the filter width the smooth value will equal the received value. This can occur if different compression ratios were used for the waveform.

Determine the time of the beginning of signal (sig_beg) which is the first time t such that $wfsm(t) > Noise + Nsig * \sigma_noise$, and the time of the end of the signal (sig_end) which is the last time t such that $wfsm(t) > Noise + Nsig * \sigma_noise$.

IF (sig_beg-sig_end) > sig_width THEN set flag_signal=0. get out of loop

Loop End.

Block diagrams showing the smoothing logic are shown in Figures 5 and 6.

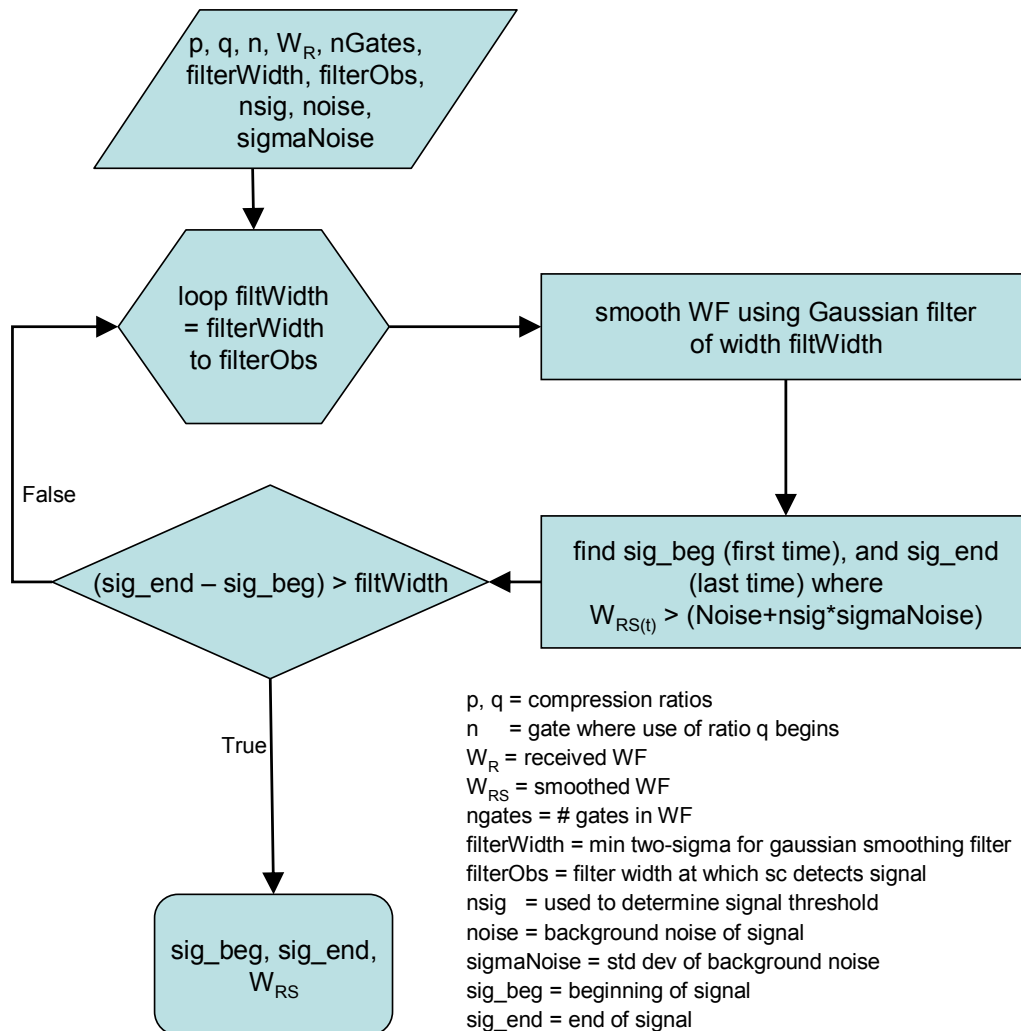


Figure 5 - Block Diagram of Waveform Smoothing Methodology

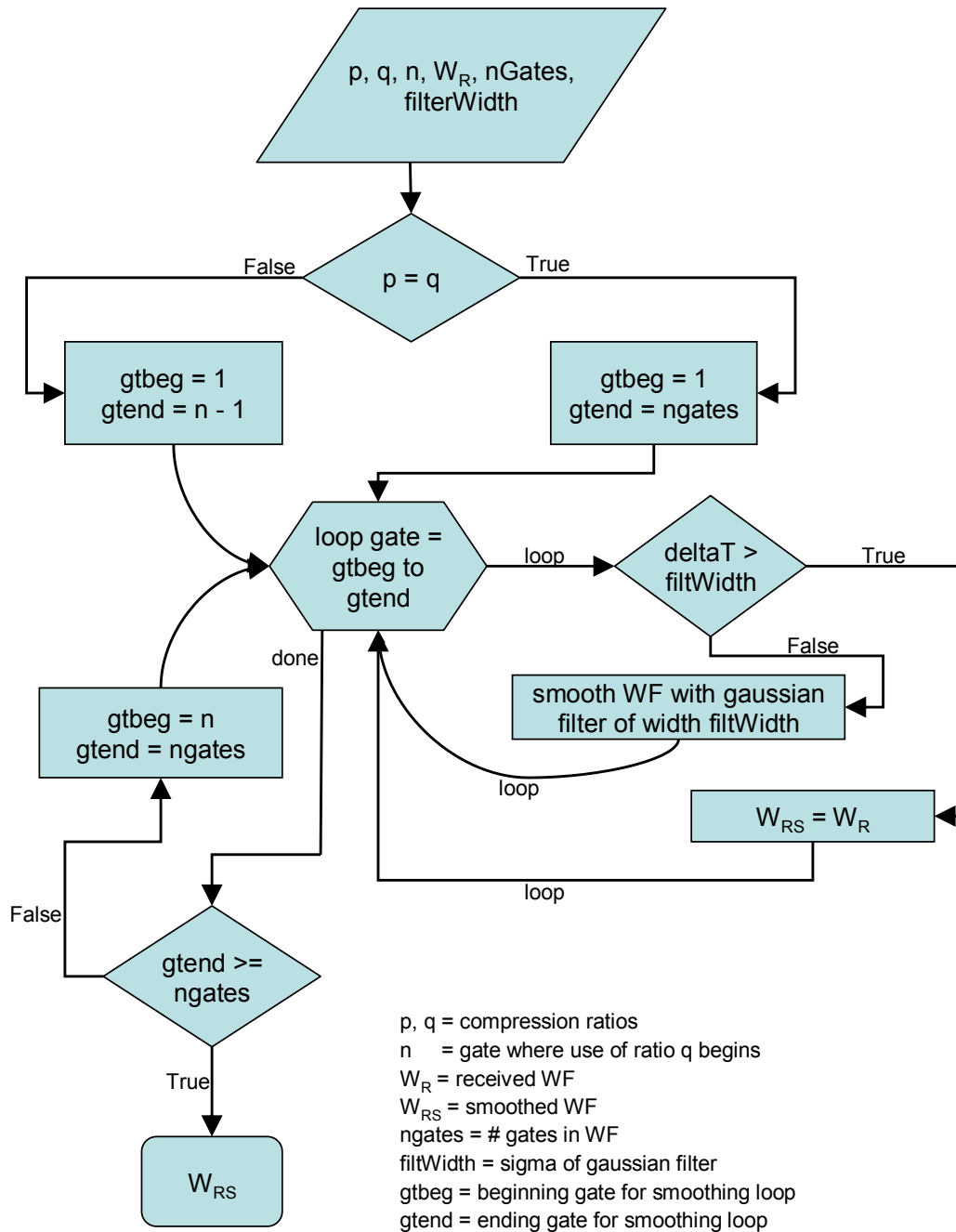


Figure 6 - Smooth WF using Gaussian filter of width filtWidth

4.1.3.12 Select Region within the Waveform with Which to Continue Further Processing

IF slctregn is set THEN

Time_beg = beginning time of selected region = MAX [sig_beg - offsetb, t(1)]

Time_end = end time of selected region = MIN [sig_end + offsete, t(Ngates)]

These values will default to t(1) and t(ngates) respectively if slctregn is not set.

4.1.3.13 Fit the Waveform to a Function

4.1.3.13.1 Make an Initial Estimate for the Unknown Model Parameters

Calculate the second derivative of the smoothed waveform, WFsm(t), using contiguous first forward differences to calculate the first derivative and then contiguous first forward differences of the first derivative results to calculate the second derivative.

The first and second derivatives of the waveform are:

$$\frac{\partial W_m}{\partial T} = -A_m \frac{(T - T_m)}{\sigma_m^2} e^{-\frac{(T - T_m)^2}{2\sigma_m^2}} = -W_m \frac{(T - T_m)}{\sigma_m^2} \quad [50]$$

$$\frac{\partial^2 W_m}{\partial T^2} = W_m \left(\frac{(T - T_m)^2}{\sigma_m^4} - \frac{1}{\sigma_m^2} \right) \quad [51]$$

$$\text{When } \frac{\partial^2 W_m}{\partial T^2} = 0, \quad \frac{(T - T_m)^2}{\sigma_m^4} = \frac{1}{\sigma_m^2} \text{ or } \sigma_m = |T - T_m| \quad [52]$$

where

W_m is the contribution from the mth gaussian

A_m is the amplitude of mth gaussian

T_m is the gaussian position

σ_m is the 1/e half-width (standard deviation) of the mth gaussian

The minimum gaussian amplitude is:

$$A_{\min} = \varepsilon + \sigma_{\text{noise}} \cdot d_nPeak_min \quad [53]$$

where

ε is the bias (noise level) of the waveform

σ_{noise} is the standard deviation of the noise

d_nPeak_min is a value from anc07

The second derivative of the smoothed waveform is used to find the initial peaks. $d_wf2ndDer$ is positive between the peaks, negative at the peaks, and zero at the inflection points. When $d_wf2ndDer$ goes from positive to negative (1st inflection point T_1), a new gaussian has been found. When $d_wf2ndDer$ goes from negative back to positive (second inflection point T_2), the end of the current gaussian has been found. The estimated gaussian amplitude is the maximum smoothed waveform amplitude within $[T_1, T_2]$. The estimated gaussian width is the smaller of $|T_1 - T_m|$ and $|T_2 - T_m|$ (see equation 51) for all but the maximum amplitude gaussian. The gaussian width for the maximum amplitude gaussian is found in a different way.

The gaussian width estimated with the inflection points is inaccurate when the waveform is deformed due to saturation or forward scattering. Because of this the value of σ_m for the maximum amplitude gaussian is calculated by finding T_{1_80} and T_{2_80} (the times before and after T_m at which W_m is 80% of A_m), and T_{1_61} and T_{2_61} (the times before and after T_m at which W_m is 60.653% of A_m).

From equation 19 at time T where $W_m = 0.8 A_m$:

$$|T_{80}-T_m| = 0.668047 * \sigma_{m_80} \text{ or } \sigma_{m_80} = |T_{2_80} - T_{1_80}| / 1.33609d0$$

$$T_{m_80} = (T_{2_80} - T_{1_80})/2.0d0 \quad [54]$$

And at time T where $W_m = 0.60653 A_m$:

$$|T_{61}-T_m| = \sigma_{m_61} \text{ or } \sigma_{m_61} = |T_{2_61} - T_{1_61}| / 2.0d0$$

$$T_{m_61} = (T_{2_61} - T_{1_61})/2.0d0 \quad [55]$$

The gaussian location is changed to T_{m_80} . A second estimate (σ_{m_61} and T_{m_61}) of the location and gaussian width for the maximum amplitude gaussian is calculated and saved for the fitting process in case the first estimate does not yield a good standard deviation of fit.

After all gaussians have been identified, the gaussians with amplitudes less than the minimum peak amplitude (A_{min}) are removed from the list, and all gaussians that are closer than d_intv_min (in anc07) to a neighboring gaussian are combined with their closest neighbor. The resulting number of initial peaks is stored on the product ($i_nPeaks1$ and $i_nPeaks2$). The gaussians are ranked according to their area and the gaussians with the smallest areas are combined with their closest neighbors until the number of gaussians is less than or equal to i_maxfit (Most releases set two for standard, six for alternate).

Gaussians are combined in the following way. If the area of one gaussian is less than or equal to 5% of the area of the other gaussian, then the smaller gaussian is removed. Otherwise, the gaussians are combined either by weighting them by area ($anc07\%d_cmb=[0,1]$), or by averaging them ($anc07\%d_cmb=[1,0]$).

$$Area_{new} = Area_1 + Area_2 \quad wt_1 = \frac{Area_1}{Area_{new}} \quad wt_2 = 1 - wt_1 \quad [56]$$

$$A_{new} = MAX(A_1, A_2)$$

$$\sigma_{new} = wt_1 \cdot \sigma_1 + wt_2 \cdot \sigma_2 \quad [57]$$

$$T_{new} = wt_1 \cdot T_1 + wt_2 \cdot T_2$$

where

wt_1 and wt_2 are the weights either calculated from equation 56 (by area) or both equal to 0.5

A_{new} is the amplitude of the combined gaussian

σ_{new} is the gaussian width of the combined gaussian

T_{new} is the location of the combined gaussian

4.1.3.13.2 Normalize The Waveform and Estimated Parameters

It was determined that the exit (from the fitting iteration) for goodness of fit based on the magnitude of the rms of the differences of the estimated shape fit and the actual return waveform, was inconsistent between low signal and high signal waveforms. For low signal, any fit differences from non-normalized waveforms yields a small error estimate. Also, for varying signals, the quality of fit for non-normalized waveforms is not consistent if the exit rms is compared to a constant. On a normalized waveform, the exit based on magnitude of the rms is consistent for all waveforms.

For alternate (land) processing, the waveform, and the estimated noise and amplitude parameters are normalized as follows:

$$y_{norm_noise} = \frac{(y_{noise} - y_{min})}{(y_{max} - y_{min})}$$

$$y_{norm_amp} = \frac{(y_{amp} + y_{noise} - y_{min})}{(y_{max} - y_{min})}$$
[58]

Where

- y_{noise} = Noise parameter before normalization
- y_{amp} = Waveform amplitude parameter before normalization
- y_{min} = Minimum waveform amplitude before normalization
- y_{max} = The maximum amplitude of the un-normalized waveform.
- y_{norm_noise} = Normalized waveform noise
- y_{norm_amp} = Normalized waveform amplitude parameter

4.1.3.13.3 Perform the Nonlinear Least-Squares Fit

The methodology described in section 3.2.2 was used. All calculations were performed in double precision arithmetic. Based on the input parameter maxGoodSDev, the standard fit may have been performed twice.

After the first fit, if stdDevFit > maxGoodSDev, then a check was made to see if a second estimate (σ_{m_61} and T_{m_61}) existed. If there was a second estimate, the results of the first fit were saved, and the fit was performed a second time using the second estimate. After the second fit, stdDevFit_fit1 and stdDevFit_fit2 were compared and the fit with the best stdDevFit was kept.

If the fitting procedure stopped because it took too many iterations to converge, then l_mxiter=1.

If the fitting procedure stopped because the normal matrix became singular, then l_noFit=1.

During the fitting procedure, some peaks may be thrown out if their amplitude becomes less than a minimum amplitude ($d_minAmp = noise + (4.5) * (standard\ deviation\ of\ the\ noise)$), if the peak width becomes too narrow ($d_sigmaMinit = 2.5ns$ for release 33), or if the peak becomes too close to another peak ($d_intv_min = 15ns$ for land or $30ns$ for ocean, ice sheet, or sea ice for release 33).

4.1.3.13.4 Un-normalize the Solution Parameters

For alternate (land) processing, the waveform, and the noise and amplitude parameters are un-normalized as follows:

$$y_{noise} = y_{norm_noise} * (y_{max} - y_{min}) + y_{min}$$

$$y_{amp} = (y_{norm_amp} + y_{norm_noise}) * (y_{max} - y_{min}) + y_{min} - y_{noise}$$
[59]

Where

- y_{min} = The minimum amplitude before normalization
- y_{max} = The maximum amplitude before normalization
- y_{norm_noise} = Normalized waveform noise after the fit
- y_{norm_amp} = Normalized waveform amplitude parameter after the fit
- y_{noise} = Un-normalized solution noise parameter
- y_{amp} = Un-normalized solution waveform amplitude parameter

4.1.3.13.5 Output Parameters from the Fitting Procedure:

1. Npeak_init: the number of peaks found in the initialization procedure. This can be greater than 6.
2. Npeak_soln: the number of peaks solved for.
3. The amplitude, σ , and position of each Gaussian in the fit
4. The noise value, signal_noise
5. The χ^2 of the fit
6. l_noFitAlt, l_noFitStd: flags in wfQual indicating if the fit was unsuccessful (numerical instabilities occurred).
7. l_mxiterAlt, l_mxiterStd: flags in wfQual indicating the fit ended without meeting convergence criteria.

4.1.3.14 For Multiple-Gaussian Fits, Rank the Peaks Found

The number of peaks found by the Gaussian fitting may exceed the available space for storing the fit parameters in the final data structure, which is limited to a total of 6 Gaussian peaks. This may in particular occur for complex land returns. Peaks will be ranked based on the area of each Gaussian fit.

4.1.3.15 Calculate General Waveform Assessment Parameters

The waveform assessment parameters are based on the portion of the waveform above noise level. This step therefore begins by calculating

$$wf(t)_{signal} = wf(t) - signal_noise$$

$$wf(t)_{sm_signal} = wf(t)_{sm} - signal_noise \tag{60}$$

From these, compute:

Table 4-2 Waveform Assessment Parameters

maxamp	Maximum amplitude of wf(t) from time_beg to time_end
centroid	Centroid of wf(t)_signal from time_beg to time_end
Total area under received pulse signal	Total Area under wf(t)_signal from sig_beg to sig_end
skewness	Skewness of wf(t)_signal from time_beg to time_end
kurtosis	Kurtosis of wf(t)_signal from time_beg to time_end
Maxamp_sm	Maximum amplitude of wf(t)_sm from time_beg to time_end

4.1.3.16 Calculate a Threshold Retracker Correction

Calculate the value, the time in ns from the beginning of the waveform to the location on the waveform where it first crosses a threshold power value based on the threshold level defined on the input parameter file, thresh_lvl. This thresh_lvl is given as a percentage of the maximum amplitude of the smoothed

waveform above the noise. Find the index i within the array $t(n)$, where $wf(i)$ is $> \text{thresh_lvl} * \text{maxamp_sm}$. Then linearly interpolate between $wf(i)$ and $wf(i-1)$ to obtain the exact value of t that corresponds to $wf(t) = \text{thresh_lvl} * \text{maxamp_sm}$, ($t_{\text{TH_RET}}$). Calculate the threshold retracker offset to the ref range as $\text{thRtkRngOff} = t_{\text{TH_RET}} - \text{Range_ref}$.

4.1.4 Output Parameters

This table lists the output parameters from the waveform characterization process.

Table 4-3 Output parameters from the waveform characterization process

preRngOff	range offset to be added to reference range based on location on the waveform defined as the preliminary correction location (ns) ($i_preRngOff1$ & $i_preRngOff2$)
Lat_pre_uncor	geodetic latitude associated with the preliminary range uncorrected for atmospheric delays, no tides applied (deg N) (GLA05%i_lat)
Long_pre_uncor	geodetic longitude associated with the preliminary range uncorrected for atmospheric delays, no tides applied (deg E) (GLA05%i_lon)
Elev_pre_uncor	surface elevation relative to the reference ellipsoid uncorrected for atmospheric delays, no tides applied (mm) (GLA05%i_elev)
Noise, stdDev_noise	Noise level and corresponding standard deviation of the waveform either calculated or set from instrument (counts) (GLA05%i_parm1(1,:) & GLA05%i_parm2(1))
Maxamp	Maximum amplitude of $wf(t)$ from time_beg to time_end (counts) (GLA05%i_maxRecAmp)
Sig_beg, Sig_end	$t(n)$ of beginning and ending signal in waveform in ns from gate 1 – closest gate to the spacecraft (GLA05% i_minRngOff1, GLA05% i_preRngOff1, GLA05% i_minRngOff2, & GLA05% i_preRngOff2)
Time_beg, Time_end	Beginning and end time within which to process signal in ns from gate 1 – closest gate to the spacecraft
Npeak_init	Number of peaks found in waveform during initialization procedure
Npeak_soln	Number of peaks solved for during final functional fit (GLA05%i_nPeaks1 & GLA05%i_nPeaks2)
Amp, location, and σ	Parameters of each Gaussian peak in the functional fit (GLA05%i_parm1 & GLA05%i_parm2)
wfFitSDev	Standard deviation of fit (GLA05%i_wfFitSDev_1 & GLA05%i_wfFitSDev_2)
Covariance Diagonals	Standard deviation of each parameter solved for in the functional fit (GLA05%i_solnSigmas1 & GLA05%i_solnSigmas2)
Centroid	Offset to be added to the reference range to give the centroid of $wf(t)$ from time_beg to time_end in ns from gate 1 (GLA05%i_centroid1 & GLA05%i_centroid2)

centroidInstr	Offset to be added to the reference range to give the centroid of wf(t) from the times before and after the maximum amplitude where wf(t) crosses the retracker threshold. (GLA05%i_centroidInstr)
thRtkRngOff	Range offset to be added to the reference range to give the range based on the threshold retracker in ns (GLA05%i_thRtkRngOff1 & GLA05%i_thRtkRngOff2)
Total_area	Total area under wf(t) from time_beg to time_end (GLA05% i_areaRecWF1 & GLA05% i_areaRecWF2)
ReflectUncorr, ReflectUncMxpk	Reflectance (not corrected for atmospheric effects) using the signal between signal begin and signal end, and for the maximum amplitude gaussian. (GLA05% i_reflectUncorr & GLA05% i_reflectuncmxpk)
WfQual flags	Flags for each shot indicating: the fitting procedure ended because the number of iterations exceeded maxiter (both standard and alternate); no leading, or trailing edge (both standard and alternate); the laser footprint is on possible land, ocean, ice sheet, or sea ice surface; the waveform is invalid; no transmitted pulse; the fitting process was not successful (both standard and alternate); the noise and standard deviation of noise were calculated (both standard and alternate); no signal was found (both standard and alternate); the fitting procedure used the entire waveform, or a selected region (both standard and alternate); the first gate was above threshold for both alternate and standard; the waveform was fit (either standard or alternate), and the signal width was too narrow, or the maximum peak was too short; alternate parameterization was used; standard parameterization was used; r type compression or pqn type compression was used; the waveform was clipped (the number of gates with amplitude in counts of 255 is greater than I_MIN4CLIP). (see online documentation at http://glas.wff.nasa.gov/glas_pv/ for description of flags).

4.2 Variance or Uncertainty Of Estimates

The estimation procedure gives quantitative values for the uncertainties in the parameters being estimated. However there are many surface, instrument, and atmospheric characteristics that will affect the shape of the return waveform. Our algorithms are based on several assumptions. This section examines the uncertainties in the physical quantities being calculated when these assumptions do not hold, and their effect on the ice sheet, sea ice, land, and ocean products.

The anticipated ranging error of single laser pulses comprises the time of flight measurement error and the clock frequency estimation error. Gardner (1992) developed analytic expressions to compute the variance of the centroid time and the received laser pulse width for the simple terrain surface pictured in Figure 2. Gardner (1992) and Harding et al., (1994) used these expressions to determine the RMS range and pulse width errors to evaluate the expected performance of different satellite laser altimeter designs.

The analytic expression (adapted from Harding et al., 1994) separates the sources of the received pulse centroid time variance into five components (impulse response, surface roughness, beam curvature, nadir angle and slope, and pointing uncertainty):

$$\begin{aligned}
\text{var}(T_p) = & F\text{var}(s_i)/N_r + (FN_B + N_D)T^3/(N_s^2 \cdot 12 \cdot \Delta t) + \Delta t^2/12 + \\
& + (F/N_r + 1/K_s) \frac{4\text{var}(\Delta\text{var}(s(S_x)))}{c^2 \cos^2(f + S_x)} + \\
& + (F/N_r + 1/(2 \cdot K_s)) \frac{4z^2 \tan^4 q_T}{c^2 \cos^2 f} + \\
& + (F/N_r + 1/(2 \cdot K_s)) \frac{4z^2 \tan^2 q_T}{c^2 \cos^2 f} \cdot \left[\tan^2(f + S_x) + \frac{\tan^2(S_y) \cos^2(S_x)}{\cos^2(f + S_x)} \right] + \\
& + \frac{4z^2 (1 + \tan^2 q_T)^2}{c^2 \cos^2 f} \left[\tan^2(f + S_x) \text{var}(\Delta v_x) + \frac{\tan^2(S_y) \cos^2(S_x) \cos^2 f}{\cos^2(f + S_x)} \text{var}(\Delta a_y) \right]
\end{aligned} \tag{61}$$

where T_P is the propagation delay measured by the pulse centroid time as it is introduced in 3.1.2.1.,
 F is the avalanche photodiode excess noise factor,
 $\text{var}(s_i)$ is the variance of transmitted laser pulse width,
 N_r is the mean signal photoelectrons,
 N_B is the mean solar background photoelectrons,
 N_D is the mean detector dark counts,

T is the detector integration time,

Δt is the time-interval-unit resolution,

K_S is the speckle signal-to-noise ratio $= \pi A_r [2 \cdot \tan(q_T/\lambda)]^2$, A_r is the receiver area, and λ is the laser wavelength,

$\text{var}(\Delta\xi)$ is the variance of the surface roughness,

c is the effective velocity of light,

f is the off-nadir pointing angle of laser beam,

S_x is the surface slope in (xz) plane, S_y is the surface slope in (yz) plane,

z is the altimeter height above the terrain,

q_T is the halfwidth divergence angle of the laser beam measured at the $1/SQRT(e)$ point,

Δf_x is the pointing error parallel to the pointing direction, and Δf_y is the pointing error perpendicular to the pointing direction.

The first four components in equation 61, that is the impulse response, the surface roughness, the beam curvature, and the geometric component dependent on the off-nadir angle of the laser beam and the slope of the surface, account for effects that cause pulse spreading in time of the received pulse. Note, however, that equation 61 does not include the effects of pulse spreading by forward scattering of the laser pulse by thin clouds and aerosols. With increased spreading of the pulse, range errors are increased because the centroid of the broad pulse is less accurately determined than that of a narrow pulse, given the same total energy, due to a lower peak signal to noise ratio.

These pulse spreading components are dominated by the photon noise. The photon noise contributions are inversely proportional to the mean signal photoelectrons (N_r), which is the number of photoelectrons detected per laser pulse:

$$N_r = \left(\frac{E_r \eta}{h \nu} \right) \left(\frac{A_r}{z^2} \right) \tau_{\text{sys}} \tau_{\text{sys}}^2 \left(\frac{r_{\text{surf}}}{\Omega_{\text{surf}}} \right) \tag{62}$$

where E_r is the transmitted laser energy,
 η is the quantum efficiency of the detector,
 $h\nu$ is the photon energy
 A_r is the telescope area,
 z is the range from the spacecraft to the Earth surface,
 τ_{atm} is the atmospheric transmission,
 τ_{sys} is the system transmission,
 Ω_{surf} is the surface scattering angle, and
 r_{surf} is the surface diffuse reflectivity.

For GLAS values the average number of photoelectrons received is expected to be typically 5,000-40,000. Link margin calculations indicate high SNR for the GLAS system. For example, in the case of moderately sloping ice/snow terrain (slope=3°, reflectivity=0.6), the estimated link margin is 14.5 dB at night and 13 dB in the daytime. This SNR is high enough to obtain reliable range and surface roughness measurements even in case of large changes in surface albedo and roughness, and atmospheric transmission variability due to aerosol and cirrus cloud scattering process (Bufton, 1989).

The pulse spreading components also include the speckle noise contributions. The speckle noise effects are inversely proportional to K_s , which is the ratio of the receiver aperture area to the speckle correlation area. According to Bufton (1982), speckle noise is negligible for the GLAS system because of the large number of spatial and temporal speckle cells averaged during each individual range measurement.

The final component in equation 61 is sensitive to laser pointing angle uncertainties. For small pointing uncertainties Bufton (1982) approximated the range error due to this component by

$$\Delta Z = Z \Delta f \tan(S + f) \quad [63]$$

For the GLAS system both the pointing uncertainty (1.5 arcsec) and the normal off-nadir pointing angles (< 1 deg) are small and therefore the ranging error due to the pointing uncertainty will be dominated by the effect of surface slope.

Gardner (1992) also derived an analytical expression similar to equation 61 for estimating the variance of the received pulse width.

To evaluate the performance of the waveform algorithms the analytical expressions and laser altimetry simulations will be used to compute the RMS range error and RMS pulse width errors of the GLAS system. These errors will be estimated over different types of ice sheet, sea ice, ocean and land topography and they will be analyzed in a similar fashion as it was reported in Gardner 1992, and Harding et al., 1994.

The algorithm described in the theory section and the analytical expression presented in this section are valid in cases of horizontal, linear sloping, isotropic, and stationary rough surfaces, uniform Lambertian reflectivity, and Gaussian laser beam far field pattern and atmospheric effects are neglected. Further research should be undertaken to analyze the errors introduced by the deviations from this ideal case or by distortions caused by the atmosphere.

4.3 Numerical Computation Considerations

The mathematical procedures described in the previous sections were tested on SLA-2 and the large footprint aircraft laser configuration (Bigfoot) waveforms. The results are discussed in section 4.3.2. This section describes the problem in more detail and suggests references to check for prototyping different numerical methods for solving the non-linear estimation problem.

The problem is to fit an equation of the form

$$y = a + \sum b_i G_i \quad [64]$$

where the G_i are functions which also contain parameters, subject to the constraints

1. $a > 0$
2. $b_i > 0$
3. For each G_i , bounds on the location of the peak and the width of the function.

In addition, there is information available on the uncertainties in the estimates of the parameters. The code used at GSFC for analysis of radar altimetry data incorporates this information by doing Bayesian least squares analysis (Zwally et al, 1990). Without the Bayesian constraints, the calculation frequently did not converge.

The Shuttle Laser Altimeter group is using a Levenberg-Marquardt (LM) algorithm (Press et al, 1986) with constraints, coded in IDL (Interactive Data Language) (Harding et al, 1998). The constraints are handled as follows: at the end of an iteration, if any parameters are outside the acceptable region, do the following before continuing with the next iteration:

1. Determine the minimum linear interpolation step that takes any one parameter from its value at the start of the iteration to its limiting value. Assume this is the step size rather than the step size used and scale all changes in the parameters to this value.
2. Compute the derivatives of all parameters that are at their limits. If the derivative tends to move the parameter out of the acceptable region, set it to zero. In optimization terminology, this has the effect of removing the variable from the "active set."

The GLAS code was written in Fortran, with some subroutines written in C for efficiency, and the derivatives were computed using the known form of the fitting function for both efficiency and accuracy (SLA code uses a numerical derivative).

Initial estimates

A high-quality initial estimate of the parameters is important to reduce the time it takes the nonlinear least squares procedure to converge.

4.3.1 Programmer/Procedural Considerations

Though we have data from several aircraft and SLA data sets with which to test our algorithms, we did not have test waveforms that emulated all the expected performance characteristics of the GLAS instrument. Test data was available from the airborne lidar (LVIS) for testing of GLAS processing algorithms. Prior to the availability of these test data, the GLAS simulator was used to exercise processing algorithms. However, it must be recognized that the GLAS instrument was different from any previously flown, and therefore the algorithms needed to be programmed so that changes could be incorporated easily. To allow for this the following was taken into consideration.

- The parameter estimation procedure had to be written in distinct modules so that it could accept a change in the fitting function or the technique used to solve for the function parameters with minimal code changes.
- The algorithms had to be run off of a parameter file which could contain different values for the same parameter based on region. This was with the expectation that the land parameters would be different from those used for the other three surface types.
- The program had to be able to process data from all four surface types or to select and process only ice sheet and sea ice data.

NOTE: all calculations were done in double precision arithmetic.

4.3.2 Calibration and Validation

4.3.2.1 Ice Sheet Validation with Existing Data

The waveform assessment algorithms and fitting procedure described in section 4.1 were tested with over 800,000 Bigfoot aircraft laser waveforms over Greenland, 159,800 SLA-2 waveforms from observation 3 (an assigned ID from the mission) over land and water, and around 70 GLAS simulated forward scattering waveforms, and 270 2D simulated waveforms. The fitting process converged more than 99% of the time for reasonably good waveforms. Bigfoot data were acquired by NASA's airborne laser altimeter over Greenland in 1993 using the instrument in a configuration that produced a GLAS size footprint. Most of the waveforms are single peaked pulses. A single Gaussian function fits these waveform very well as shown in Figure 7.

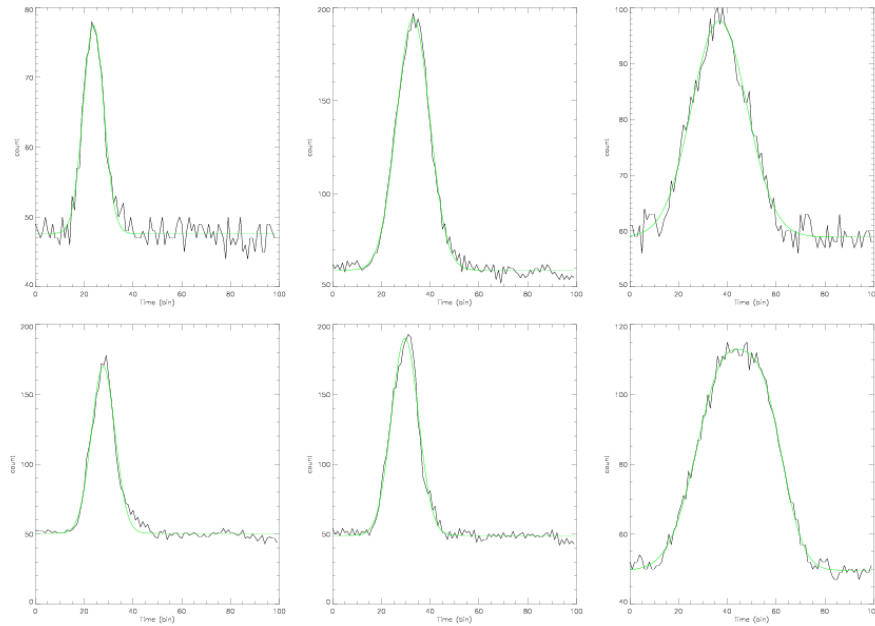


Figure 7 - Bigfoot waveforms over Greenland Fit with a Gaussian Function

SLA02 data cover both land and ocean. Most of the waveforms are single peaked and can be fit by a single Gaussian function. Sometimes the waveforms over land are multi-peaked and need to be fit by multi-Gaussian-functions as shown in Figure 8. This may be caused by multiple elevation levels within the laser footprint caused by buildings, vegetation or terrain. The ringing in the SLA02 data after the peak is caused by the instrument and is not expected in the GLAS data.

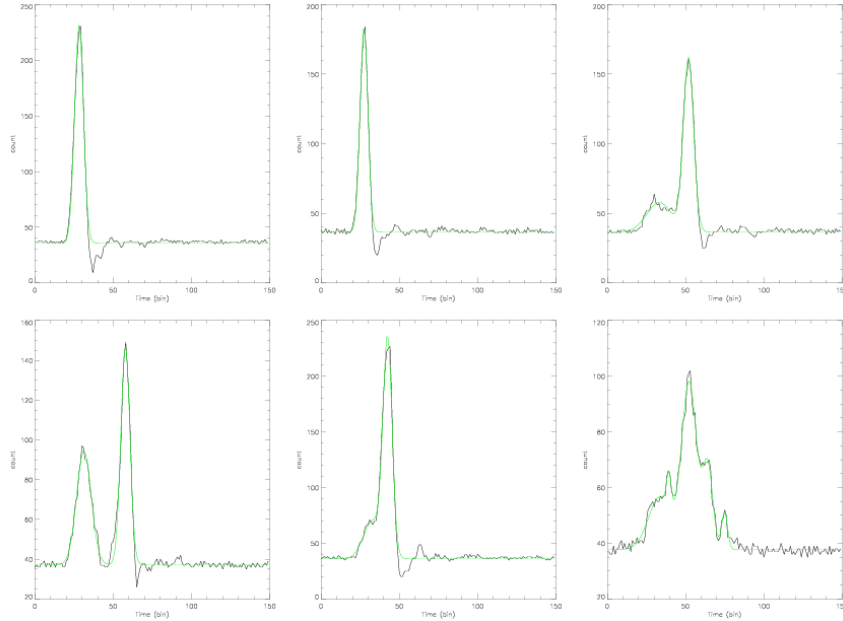


Figure 8 - SLA02 data fit with a Gaussian function

Atmosphere forward scattering changes the shape of the return waveforms. Over flat surfaces this portrays itself as a rise in the tail over the leading edge. David Duda and Jim Spinhirne (personal communications 1998) provided simulated waveforms for various cloud conditions that are expected to cause forward scattering. For these non-symmetrical returns, calculating the range to the centroid of the fitted Gaussian gives better agreement with the actual surface than using the centroid of the received waveform. Figure 9 shows the forward scattering waveform, its non-forward scattering component, its forward scattering component, and a Gaussian fit to the forward scattering waveform. The centroid of the non-scattering component at 14.95 ns is the known surface position. The centroid of the forward scattering waveform is at 16.88 ns, which gives a bias of 1.93 ns (equals to 28.95 cm in elevation) compare to the known surface. The centroid of the fitted Gaussian ($\pm 3\sigma$ edited Gaussian fit) is at 15.41ns, which gives a bias of 0.46 ns (equals to 6.9 cm in elevation) compare to the known surface. This result shows that the difference between the centroid of the fitted Gaussian pulse and the forward scattering waveform is 1.5 ns (equals to 22.5 cm in elevation) which is a significant decrease in elevation bias introduced by forward scattering.

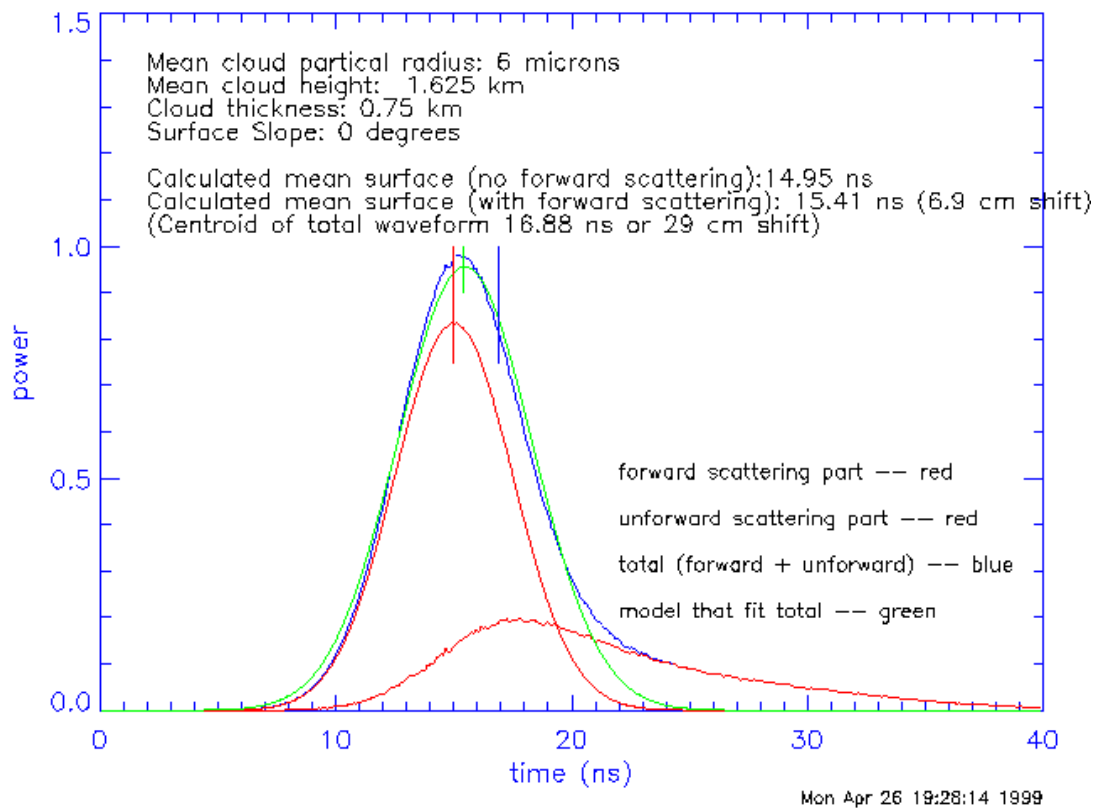


Figure 9 - Forward Scattering Effect on the Laser Return Waveform

Figure 10 shows the biases incurred in the calculation of the surface elevation from the return when the centroid of the Gaussian fit and the centroid of the received return are used as the position on the return which pertains to the mean surface for various cloud heights, particle size and cloud thickness. Using the centroid of the Gaussian fit always decreases the effect of forward scattering on the calculated elevation. Significant decreases are shown for low clouds where the forward scattering bias is high. Using the centroid of the Gaussian fit can reduce the forward scattering bias, but cannot eliminate it.

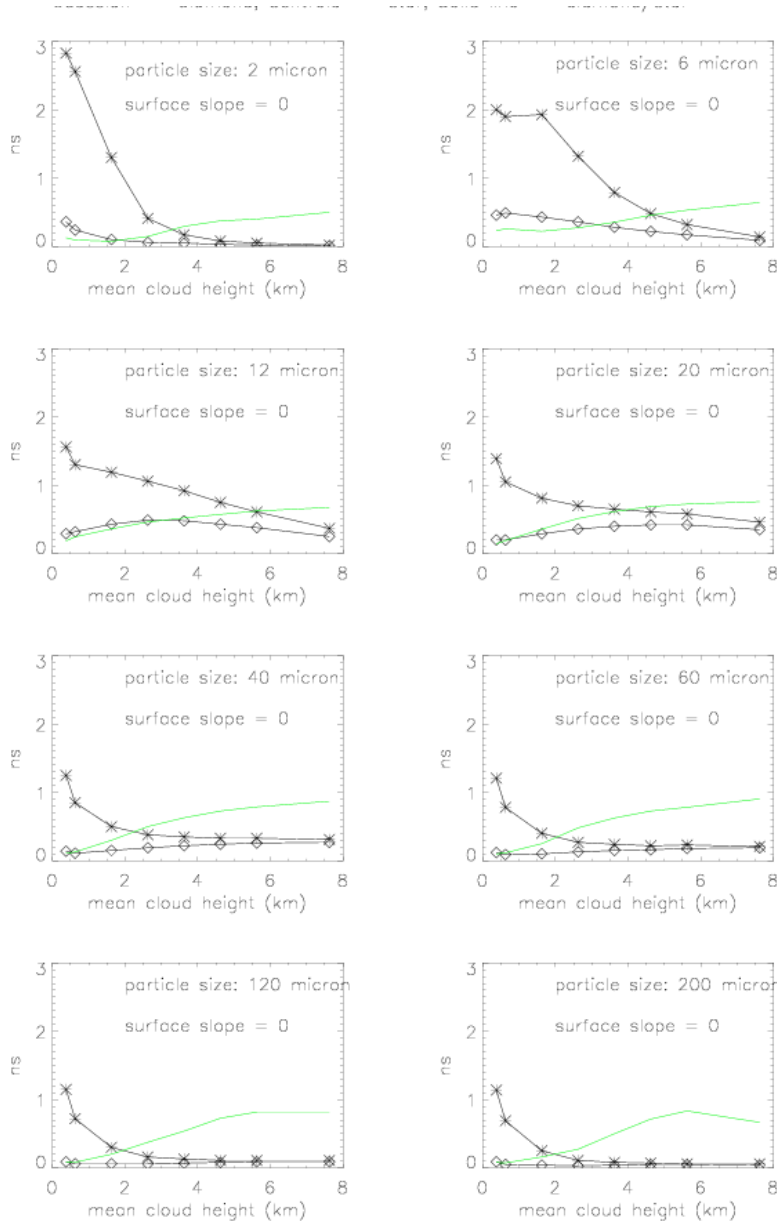


Figure 10 - Bias in ns from surface elevation; star - centroid of the return, diamond - centroid of the Gaussian fit

As a test of the algorithm, a simulation was carried out by using a real surface elevation profile over Greenland. The data were collected on the Jakobshavns glacier by the NASA ATM system. The profile is about 50 km along with 10 cm spacing between data. The surface profile was put into a 2D simulator to generate waveforms. The generated waveforms were analyzed with the retracking algorithm. The calculated surface elevation agrees with the known surface elevation very well. For the 270 simulated waveforms, the error is 5 cm without three points in a very rough zone (Figure 11). The calculated surface slope and surface roughness were compared with known surface roughness and surface slope (Figure 12). Figure 13 and Figure 14 are two examples that show surface elevations within the footprint and their waveforms. The waveform in these figures shows the simulated return. The elevation profiles show the elevation over the footprint with the x denoting the mean elevation calculated from the surface and the rectangle denoting the mean elevation calculated from using the algorithms described in section 4. In

figure 13, the return is a single peak Gaussian and the mean elevation from the algorithms agrees with the actual value. In figure 14, the return is a sum of two Gaussians due to the different elevations in the footprint and the calculated value (which corresponds to the centroid of the last Gaussian) is lower than the actual mean elevation because it represents the mean from the lower surface.

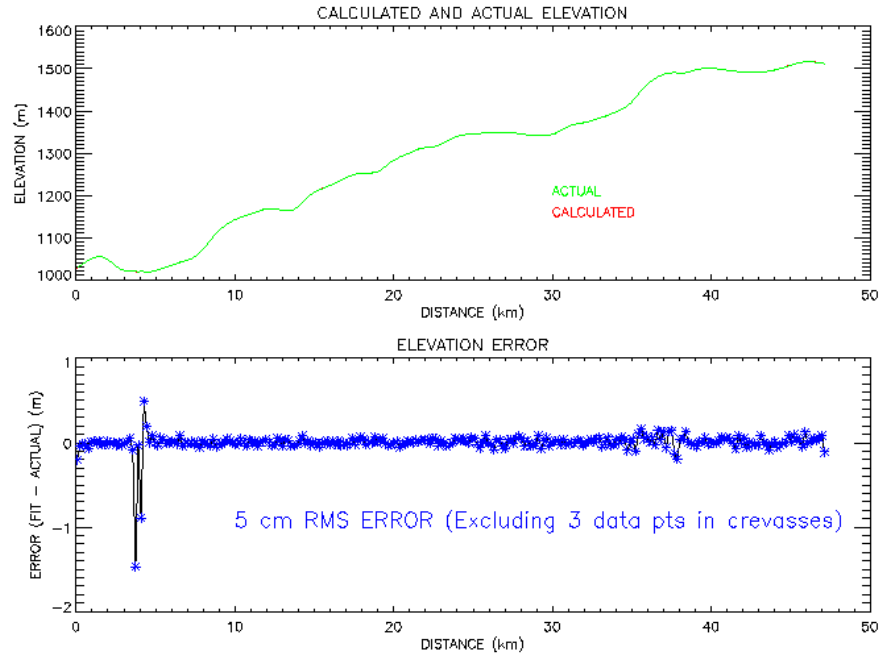


Figure 11 - Comparison of simulated and actual surface and resultant GLAS elevation algorithm error

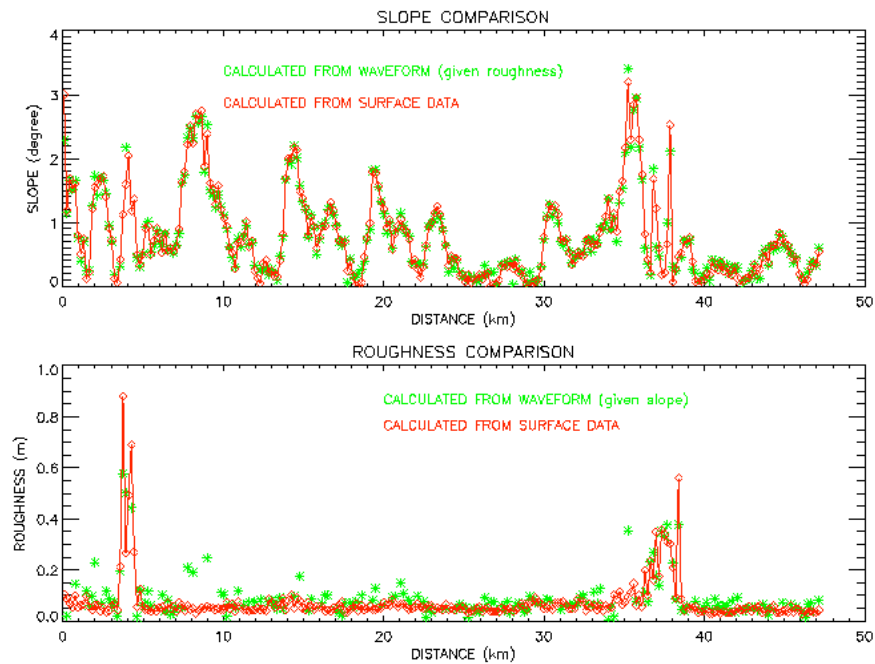


Figure 12 - Comparison of actual vs calculated surface roughness and slope (no longer calculated).

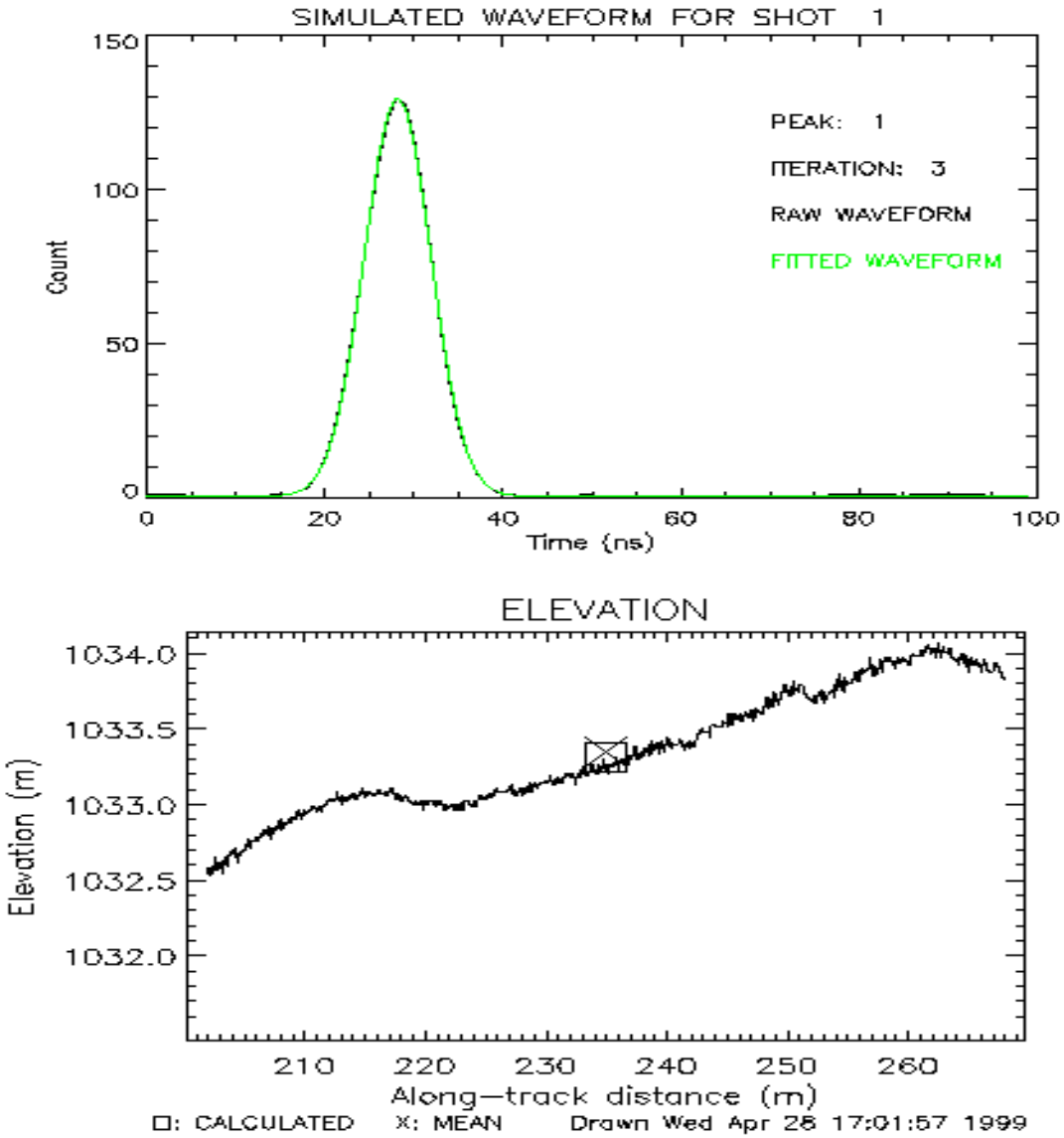


Figure 13- Simulated elevation and corresponding waveform using real ice sheet profile

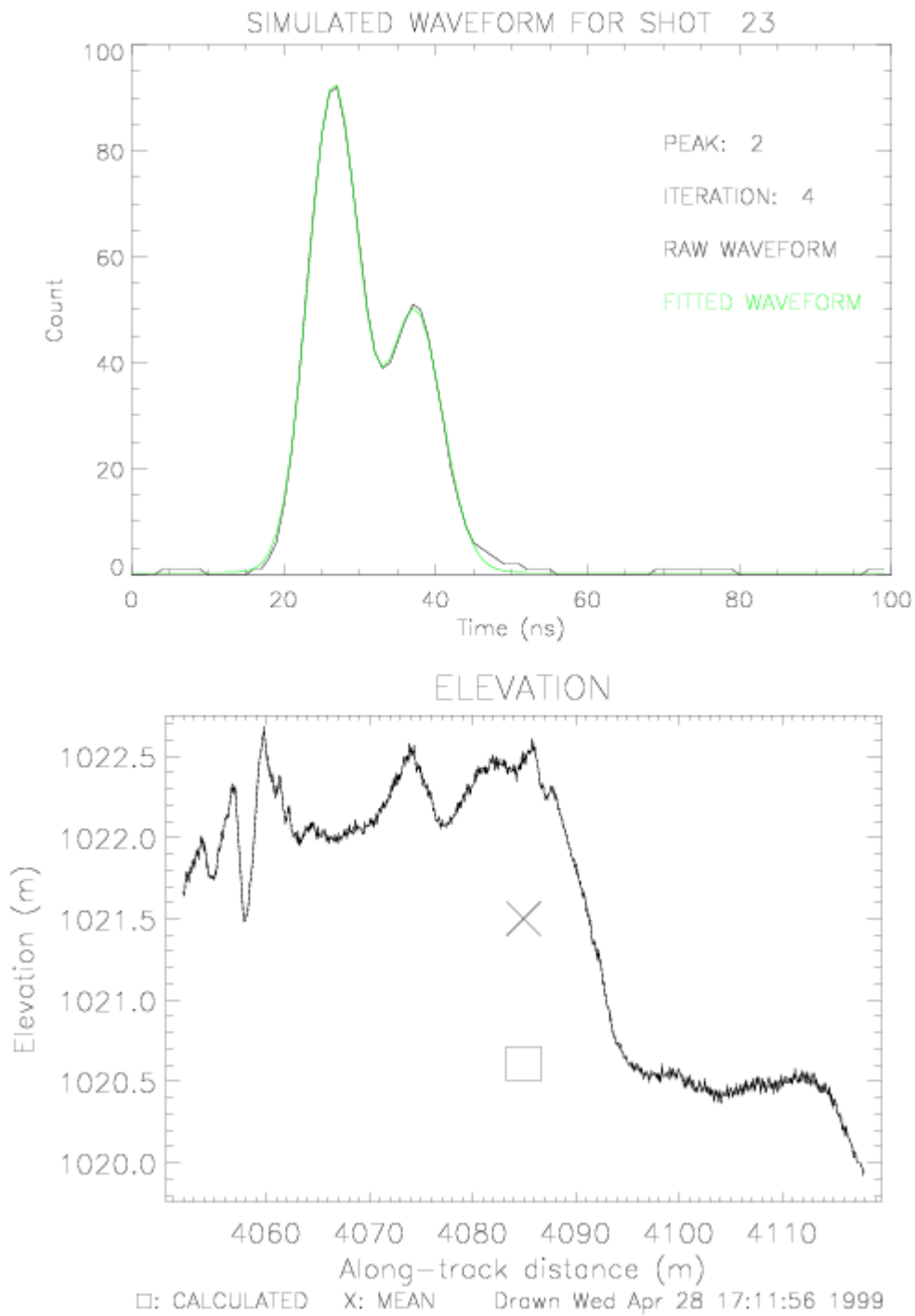


Figure 14 - Simulated elevation and corresponding waveform using real ice sheet profile

4.3.2.2 Validation of Sea Ice Algorithm

The algorithm was tested by computing laser waveforms for various sea ice models using the Goddard Laser Altimeter Simulator (Version 3.8). The simulator program derived altimeter return-pulse waveforms in a simplified two-dimensional (height versus along-track distance) measurement geometry. The waveform was computed as it propagated to the terrain surface and back to the altimeter receiver. The simulator's receiver included a telescope, an optical bandpass filter, either a photomultiplier or an avalanche photodiode optical detector (Si APD), a low pass filter, a timing discriminator, a time interval unit and a waveform digitizer. Simulation did not model the effects of atmospheric refraction or scattering. The terrain surface was assumed to be a Lambertian reflector, and its reflectivity and height was specified for every centimeter of along-track distance. For details on the operation of the simulator see Abshire et al, 1994. Examples of computed waveforms are presented in Figure 15 and in Csathó and Thomas (1995).

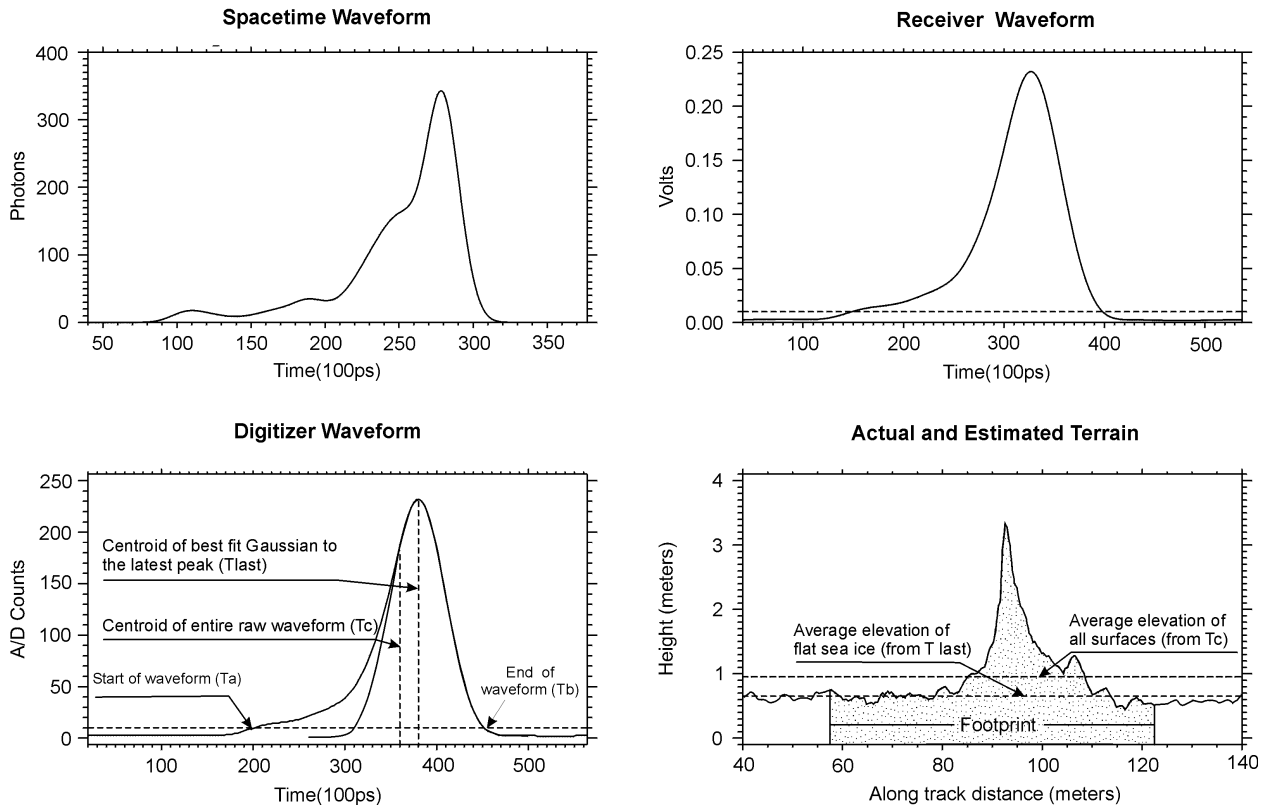


Figure 15 - Simulated laser altimetry waveforms

For evaluating the surface roughness algorithm we used the icex.dat sea-ice data set distributed with the GLAS simulator software (Abshire et al, 1994). The surface elevations were measured by an airborne laser altimeter every 1 m along a 110-km profile on May 20, 1987, north of Greenland. Surface roughness was computed from surface elevations and from simulated GLAS waveforms for several different flight segments to evaluate the performance of the estimator. The different stages of the simulation are illustrated in Figure 15. The spacetime waveform (Figure 15, upper left) shows the laser pulse shape after it was reflected back from the terrain to the receiver. The largest peak was caused by the photons reflected from the nearly horizontal sea ice comprising most of the footprint (Figure 15, lower right). The small peaks and ‘shoulders’ on its left were associated with the photons reflected back from the ridges. The spacetime waveform was further processed by the simulator to model the influence of the receiver and the background noise. The smooth electrical waveform (upper right) emerging from the receiver has an asymmetric shape and a single peak associated with the flat sea ice. The digitized

waveform (Figure 15, lower left) was used as input for the range and surface roughness computation. The average surface elevation was estimated from the centroid time delay, while the centroid of the last Gaussian shaped peak provides a very precise measure of the elevation of the flat sea ice (Figure 15, lower right).

The surface roughness computed from the laser-altimeter waveforms compares well with the surface roughness derived directly from the elevation (Figure 16). However, it generally underestimated the roughness of highly ridged areas, where surface was not “stationary”. This is because most of the ridges on this profile were located in the outer part of simulated footprints, and pulse spreading was determined by the within-footprint elevation profile weighted by the normalized cross section of the laser beam (Gardner, 1982). Ridges located away from the footprint center have smaller weight and therefore produce less pulse spreading.

Soon after the ICESat launch, aircraft measurements of sea-ice topography at very high spatial resolution (using the conical-scanning Airborne Topographic Mapper (ATM)) were made, which provided a detailed description of the sea-ice surface within many GLAS footprints. Data products derived by the GLAS sea-ice algorithm were compared with equivalent products derived from the detailed mapping. These flights were conducted out of Thule Air Force Base in northern Greenland in conjunction with underflights to validate GLAS performance over the ice sheet (see appendix 1 for an explanation for the removal of slope and roughness from the products).

4.3.2.3 Land Validation with Existing Data

The validity of the GLAS waveform processing algorithms for determination of land topography parameters (elevation, slope and roughness, vegetation height) was evaluated using airborne laser data. ICESat emulation data with 70 m diameter footprints were compared to higher resolution data (contiguous, 12 m diameter footprints in a narrow swath). Both data sets were acquired by the airborne SLICER instrument along a common transect in the southern part of Gifford Pinchot National Forest in southeastern Washington (state). The transect crossed a diverse landscape with a variety of slope and vegetation cover conditions. The smaller footprint data permitted accurate separation of lidar backscatter returns from canopy layers and the underlying ground, and thus characterization of canopy structure and ground elevation and slope. The large diameter footprints were compared as a function of slope to coincident aggregates of the higher resolution footprints in order to establish the amount of mixing between canopy and ground returns at the scale of ICESat footprints. Initial comparisons showed that the large-diameter backscatter returns from sites with low slope were typically bimodal with separate canopy and ground returns but, as expected, increasing slope caused increased mixing and resulting ambiguity in establishing canopy structure and underlying ground elevations. These effects were quantified by applying the GLAS waveform processing algorithms.

4.3.2.4 Validation of Ocean Algorithm

The ocean algorithm was tested, using the same approach as described in Section 4.3.3.2, by using waveforms from airborne laser-altimeter measurements of ocean topography. First the surface elevation was estimated from each individual waveform. Then the average surface elevation was computed from the “composite” waveforms (Section 3.1.2.2.5).

After launch, GLAS ocean products were validated against equivalent products derived from satellite radar-altimeter data at locations where the orbits cross at approximately the same time.

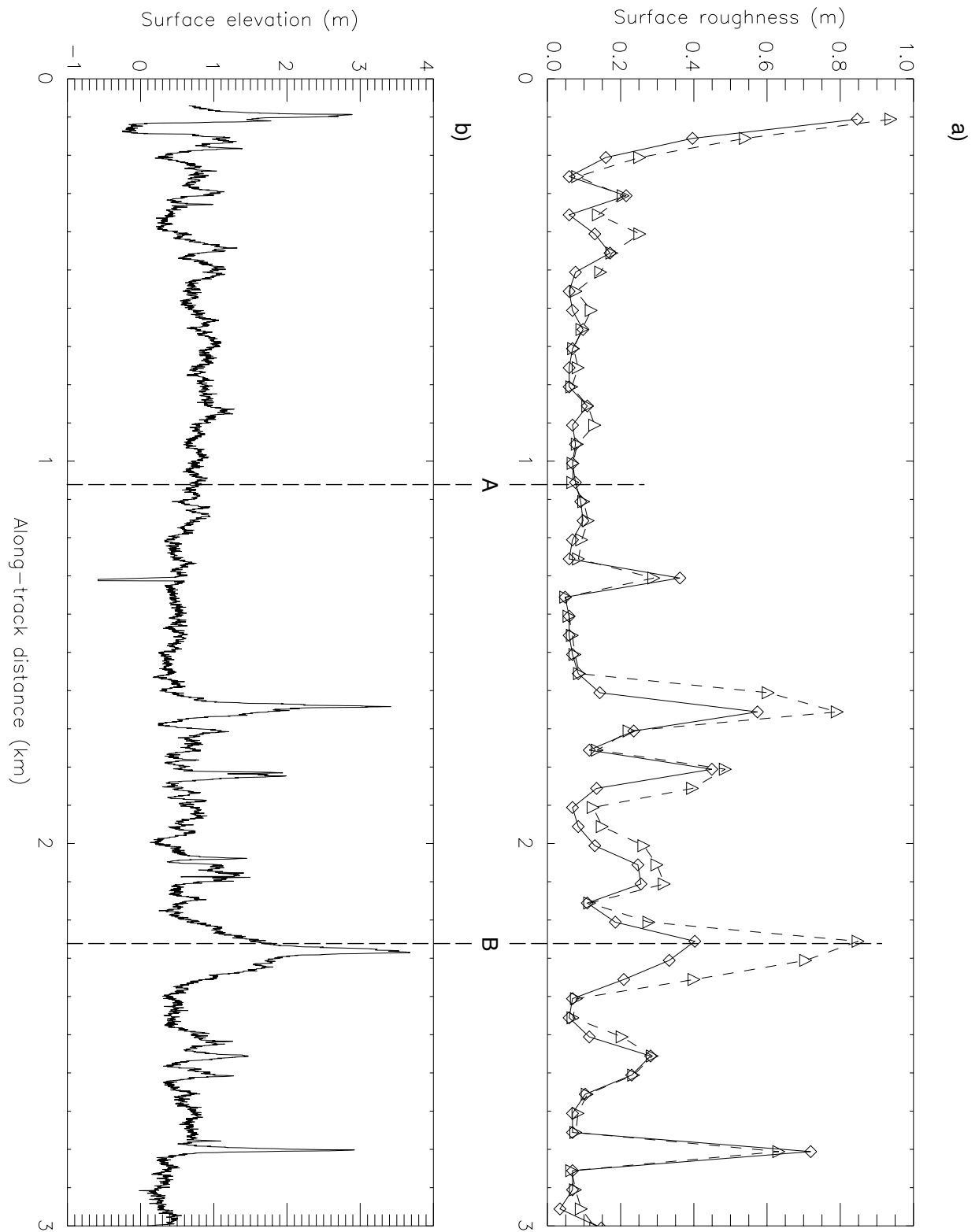


Figure 16 a) Comparison of surface roughness computed from laser-altimeter waveforms (solid line with diamonds) and from surface elevation (dashed line with triangles), b) Surface elevation profile from airborne laser-altimeter data (reflectivity = 0.8)

4.3.2.5 Validation During The 90 Day Cal/Val Period

The first 90 days of the ICESat mission were designated as a validation period. This was the first time the algorithms presented in section 4.1 were tested on real GLAS data. There were several assumptions upon which the algorithms depended, the validity of which were tested using real data. The first of these was the assumption that the transmitted pulse was Gaussian in shape. 48 gates defining the transmitted pulse was telemetered each measurement. Plots of the transmitted pulse, the Gaussian fit, and the difference between the two were interrogated to determine any significant non-Gaussian features.

The return pulse over flat surfaces looked like an impulse response. The validation period orbit took the satellite over salt flats and desert regions that could be used to determine the nature of this response. Interrogating the return pulse, the Gaussian fit to it and the difference between the two would show any fundamental problems that would have forced us to drop the assumptions that we could fit to a Gaussian.

During this period we also kept statistics as described in section 4.3.3 to determine how well the algorithm performed with real data. The fitting procedure was fine-tuned to minimize failures (where the waveform fit would not converge) and optimize the accuracy of the surface elevation measurement. One of the biggest unknowns was how the atmosphere would affect the return and how much forward scattering would cause errors in the calculated elevation. The satellite was in an 8-day repeat cycle during this period and we compared data over known terrain in different atmospheric conditions to get a better handle on the actual effect. For ice sheet validation, we underflew the satellite with an aircraft laser altimeter that was able to verify the surface elevation and roughness characteristics. These were compared with those calculated from the GLAS data and we were able to tune the algorithm to minimize the effect of the forward scattering.

Validation of the roughness algorithm for the ice sheet was provided by underflights of the GLAS track in Greenland by the Airborne Topographic Mapper. We investigated the possibilities of underflights with an airborne laser altimeter in Antarctica as well. The algorithm for slope was tested by off-nadir pointing (by several degrees) onto one or more of the flat, smooth test areas (White Sands, Bonneville Salt Flats) discussed in the GLAS validation plan.

4.3.3 Quality Control and Diagnostics

As part of the production process, statistics are calculated that allow us to determine the overall data quality and the quality of the physical properties calculated from the data.

4.3.3.1 Quality Control and Diagnostics for Ice Sheet Products

The following information was provided to allow the scientist to assess the quality of the data and related products.

- The percent of ice sheet measurements for which no signal was found
- For the subset of measurements for which a signal was found the following will be tabulated
 - The percentage of measurements for which the fitting procedure did not converge
 - The percent of measurements that could not be processed due to saturation
 - When a signal was found and the fitting procedure was successful, the following statistics were tabulated in such a manner that a histogram showing the distribution of these values could be generated. Except for the number of peaks, where the histogram bins were integers from 1 to 6, the number of histogram bins were 100. There was one set of histograms created for each granule of data.
 - The differences between the centroid of the received waveform and the centroid of the Gaussian fit to the maximum amplitude peak.
 - The number of peaks found in each smoothed waveforms.
 - The standard deviation of the fit to the received waveform
 - The skewness of each single peak return.

- The kurtosis of each single peak return.
- The percent of saturated signal compared to real signal within the signal region (from sig_beg to sig_end)
- For the subset of measurements for which a signal was found and successfully processed, the mean and standard deviation of the following quantities were calculated for each 100km strip (adjustable) along the ground track and color coded plots overlaid on maps showing these results were generated for Greenland and Antarctica.
- The number of peaks in the smoothed waveform
- The number of peaks in the gaussian fit
- The standard deviation of the fit to the received waveform for each measurement.
- The skewness of each single pulse return
- The differences between the centroid of the received waveform and the centroid of the Gaussian fit to the maximum amplitude peak
- The maximum smoothed amplitude
- The reflectance
- The surface elevation

For the same 100km strips (adjustable), the number of problem flags were calculated and displayed, and the map was marked if the surface ID (land, ocean, ice sheet, sea ice) had changed.

4.3.3.2 Quality Control and Diagnostics for Sea-Ice Products

For each sea-ice footprint not obscured by cloud, the following information was provided on each data record to allow the user to assess data quality: RMS wave height.

T_{max} = time delay of center of peak from the Gaussian fit to the maximum amplitude peak

T_c = time delay of the centroid of the received waveform from sig_beg to sig_end

T_a = the time delay to sig_beg

T_b = the time delay to sig_end

Goodness of fit of the Gaussian approximating the maximum amplitude peak;

From this information the following can be calculated.

- Number of peaks, and $(T_{max} - T_c)$, indicating complexity of topography in the footprint;
- $(T_{max} - T_a)$, and $(T_b - T_{max})$, expressed as distances, indicating the symmetry of the waveform and the possibility of forward scattering;

Browse products are separate for Arctic and Antarctic, and refer to all data from within the sea-ice mask.

The following were provided per granule:

- percent bad data, or instrument off
- histogram of freeboard (GLAS sea-ice elevation - tide-corrected local geoid elevation)

Weekly (adjustable) statistics were compiled during data processing of “successful” sea-ice data acquisitions (i.e. acquired elevations) and expressed as percentages of possible sea-ice footprints within the sea-ice masks for each 30 degrees of longitude.

Per several granules (adjustable - approximately one week), maps were made of the Arctic and of the Antarctic, showing along each orbit:

1. cloud cover in gray
2. average freeboard over approximately 1 km (adjustable)

Item 2 was presented in colors with five classes (adjustable) between 0 and the maximum value. As the mission progressed the maximum value was replaced by the upper-limit maximum value.

Before averaging, values of freeboard more than N times standard deviation were rejected. Averages were taken for any M km of data containing 90% (adjustable) coverage, to take account of spotty cloud cover.

4.3.3.3 Quality Control and Diagnostics for Ocean Products

For each ocean footprint not obscured by cloud, the following information was provided to allow the user to assess data quality:

- $(T_c - T_a)$, and $(T_b - T_c)$, expressed as distances, indicating the symmetry of the waveform and the possibility of forward scattering;
- Goodness of fit of the Gaussian fit to the waveform.

In addition, (GLAS ocean elevation - tide-corrected local geoid elevation) should be provided as a "reasonableness" check.

Weekly statistics were compiled during data processing of "successful" ocean data acquisitions (i.e. acquired elevations) expressed as percentages of possible ocean footprints for each 30 degrees longitude x 30 degrees latitude.

4.3.3.4 Quality Control and Diagnostics for Land Products

Quality control and diagnostic products for the land utilized the same methods as for ice sheets.

5.0 Waveform, Waveform Analysis and Elevation Output Products

GLAS standard output products, GLA05, 6, and 12-15 were generated based on this ATBD. The actual waveform is present on GLA01, a level 1A product, which also has a predicted orbit at the accuracy of 0.1 deg. GLA05 is a level 1B waveform parameter product. This product contains the parameters calculated from the waveforms, but the waveforms were not repeated here. GLA06 is a level 1b global elevation product and is similar to the existing geodetic data records from the radar altimetry satellites

There is one level 2 product for each region; ice sheet (GLA12), sea ice (GLA13), land (GLA14), and ocean (GLA15). Conforming to NASA's definition of level 2 products these will have the full rate data in a form usable by the science community. For GLAS this means that there are region-specific surface elevations with all required parameters necessary for it to be useable by a scientist. Masks are provided that define which data go on each product by location on the earth. These masks can overlap so that one measurement may be contained on multiple level 2 products. All GLAS output products are archived at the NSIDC (National Snow and Ice Data Center) DAAC, which is also responsible for their distribution. After the initial calibration period of 90 days, the operational mission data products were sent regularly to the NSIDC where they will be distributed upon request.

In addition to being able to correlate the products using time, there is a unique index assigned to each 1 sec frame of data as it is processed from the level 0 products. That index remains with that frame of data on every product for which information on that frame of data exists. Therefore, if one wants to find a specific waveform frame that corresponds to a level 2 elevation frame, one needs only to line up these indices. This is done to circumvent the confusion that occurs in trying to align products using time when a time correction has been applied to the higher level products but not the lower level ones. In accordance with the EOSDIS design, each product was distributed by granules. The final definition of the granule sizes for the waveform and elevation products are as follows: GLA01, 05, and 06 granule sizes are defined to be $\frac{1}{4}$ revolution of data where the granules are split at 50 deg latitude, both North and South. This keeps the polar regions on separate granules and should simplify distribution of the lower level data. The level 2 elevation product granules (GLA12-15) each contain data from 14 revolutions of the spacecraft. The following sections describe parameters that are on each of the GLAS products covered by this ATBD.

5.1 Level 1b Waveform Parameter Product –GLA05

The waveform parameter product has all of the parameters from the waveform characterization procedure and other parameters required to calculate physical properties of the surface. These include the parameters listed in appendix 4.5. Section 4.1 gives all algorithms for calculating these parameters.

Table 5-1 Parameters required to calculate physical properties of the surface for level 1b waveform product

#	Parameter	Precision
1	UTC time of laser pulse corrected for system delay, transit delay using the preliminary range, and timing bias from Jan 0 2000.	μsec
2	Range from the peak position of the transmit pulse to the telemetered gate farthest from the spacecraft (reference range).	.01 ns
3	Time increment from the reference range to the location on the waveform corresponding to the threshold retracker, t_{TH}	.01 ns
4	Maximum amplitude of the smoothed waveform	0.01 counts
5	Satellite position from the best available POD as a vector in ITRF at the ground bounce time of the measurement	mm
6	Off-nadir pointing direction (unit vector) in ITRF from the Precision attitude calculation	1.5 arc sec
7	Geodetic latitude and longitude calculated using the preliminary range with no atmospheric corrections.	μdeg
8	Surface elevation calculated using the preliminary range with no atmospheric corrections or tides applied.	mm
9	Surface identifier flags from regional ID grid –All 4: l_ocean, l_ice, l_seaice, l_land.	N/A
10	Noise level from telemetry.	.0001 volts
11	Received pulse Gain value.	N/A
12	Received Energy.	N/A
13	Transmitted Energy.	N/A
14	Transmitted gain value.	N/A
15	Low gain saturation flag	N/A
16	High gain saturation flag	N/A
17	High gain saturation with forward scattering flag	N/A
	<i>There needs to be two sets of items 18-32 one for land and one for other surfaces for each received waveform.</i>	
18	Kurtosis of the received waveform from signal begin to signal end	.01
19	Skewness of the received waveform from signal begin to signal end	.01
20	Initial number of peaks	N/A

21	Noise level from the functional fit	.0001 volts
22	Amplitude of each Gaussian peak from the functional fit	.0001 volts
23	Sigma of each Gaussian from the functional fit	.01 ns
24	Centroid position of each Gaussian from the functional fit as offset from last telemetered gate	.01 ns
25	Standard deviation from the covariance matrix for each fit parameter to the same accuracy as the parameter	
26	Flags indicating 1) successful functional fit, 2) fit convergence criteria met	N/A
27	χ^2 of the functional fit	.001 volts
28	Ranks of each peak in the solution	N/A
29	Area under the received waveform from signal begin to signal end	.01 volts x ns
30	Time increment from reference range to Centroid of the received signal using only the portion of the return between sig_beg and sig_end	.01 ns
31	Time increment from reference range to sig_beg	.01 ns
32	Time increment from reference range to sig_end (used to calculate preliminary range)	.01 ns
	<i>The following 33-39 are from the transmitted waveform</i>	
33	Amplitude of the Gaussian fit	.0001 volts
34	Sigma of Gaussian fit	.01 ns
35	Centroid position of Gaussian fit as offset from gate 1 of transmitted waveform	.01 ns
36	Skewness of transmitted pulse	.01
37	Centroid of transmitted pulse	.01 ns
38	Area under the transmitted pulse	.01 volts x ns
39	Maximum amplitude of the signal	.0001 volts

5.2 Level 1b Global Elevation Product-GLA06

The global elevation product will contain information to calculate surface elevations and associated parameters and geodetic corrections required to calculate physical quantities associated with the surface. This product is intended as a research product and a stepping stone from which the region-specific level 2 elevation products are generated. Since this is a level 1 product, the corrections need to be available on the product with enough corresponding information to calculate a new surface elevation if users want to supply their own correction(s). For this same reason all elevations are given relative to a reference ellipsoid and a geoid elevation is provided for users to reference the elevations to sea level. Information is also given here to calculate basic region-specific elevations based on the results of the waveform assessment. The geoid, and tides are quantities that vary at long wavelengths and only need to be calculated once per second (approximately 7 km along the ground). Users can linearly interpolate between the one second values for the value associated with the individual measurement. Table 5-2 lists

parameters that are to be output for every measurement. Table 5-3 lists parameters that are to be output every second.

5.2.1 Region Specific Range Increments

Based on current knowledge, for ice sheets, sea ice and ocean, the range increments are defined to the position on the waveform corresponding to the centroid of the maximum amplitude peak, as calculated from the functional fit. For the land range correction the centroid of the raw return is used. For the ocean, sea ice, and ice sheet range correction the standard parameters are used in the fitting procedure. More research needs to be done with data that more closely resemble GLAS output. We hope to achieve this with special aircraft instrumentation flights over the next two years. These tests may show that a different location on the waveform should be used for some regions. To accommodate any changes, this global output product should have distinct parameters for four different region-specific range corrections. Whereas on the waveform parameter product all range values are given in ns, on the elevation products the range values will be given in mm. The values given in ns are a two-way travel time. To convert Range_ref, which is the two-way time in ns, to a one way range in mm use the following:

$$\text{Range_ref}_{\text{mm}} = \text{Range_ref}_{\text{ns}} * c / 2, \text{ where } c \text{ is the speed of light in mm/ns}$$

All other ranges are on the data record as increments to Range_ref_{mm}. These increments are calculated using the following:

$$\text{Range_inc} = (t(\text{inc}) - t_{\text{ngates}}) * c / 2, \text{ where } t(\text{inc}) \text{ is the time (in ns from gate 1) associated with the 1 location on the waveform to which the range increment corresponds.}$$

5.2.2 Calculation of Surface Elevation

Calculating an accurate surface elevation from the altimetry measurement involves accounting for not only the waveform range corrections, which are discussed in section 4.1, but also correcting the range for atmospheric delay. After these corrections are applied to the range, the geolocation needs to be recalculated because of the non-nadir pointing direction. The algorithms for calculating the atmospheric corrections and the tides and how to apply these to calculate the correct geolocation and surface elevation are presented in other ATBDs in the GLAS document series. The mean range calculated from the signal end was used to calculate the geolocation for GLA05. Block diagrams showing the order in which the parameters were calculated are given in Figures 17 and 18.

First, as shown in Figure 17, the mean range, PAD, and POD are used to calculate a more precise geolocation. This geolocation along with time and meteorological data is input to the atmospheric delay algorithms to calculate the range corrections due to the signal interaction with the troposphere (Rcor_{w_{trop}} & Rcor_{d_{trop}}). The geolocation and time are then input to the tidal algorithms to calculate the ocean, load, and solid earth tides. The polar tide correction is included in the PAD. Figure 18 then shows how these corrections are used to correct the range from which a more accurate geolocation and surface elevation are calculated. The value of the geoid is then interpolated to allow the user to reference the elevation to mean sea level.

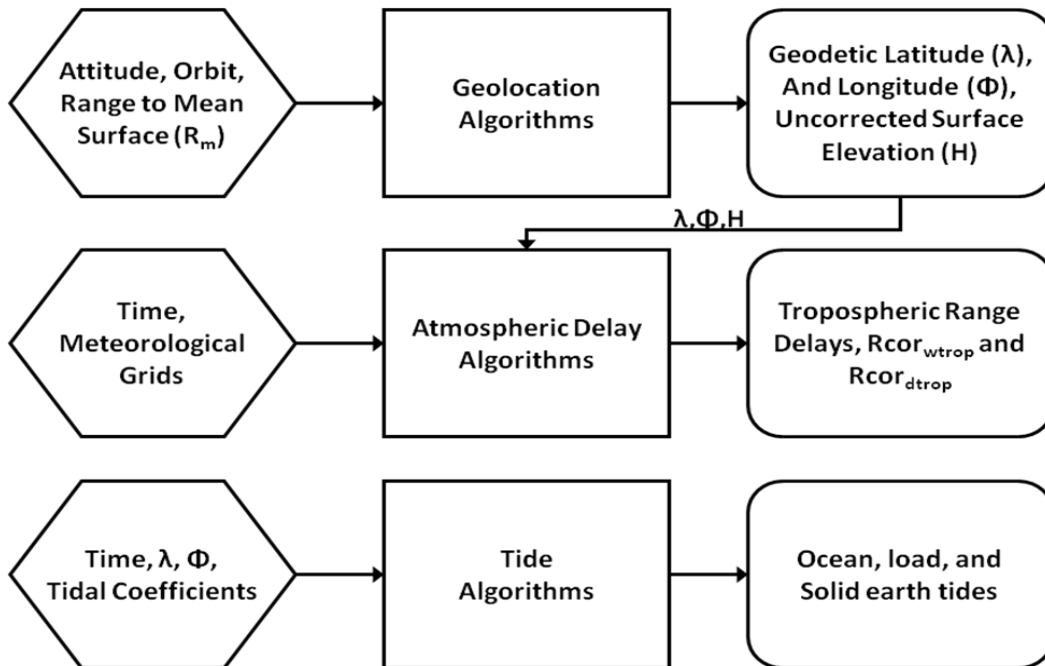


Figure 17 – Calculate Range Corrections and Tides

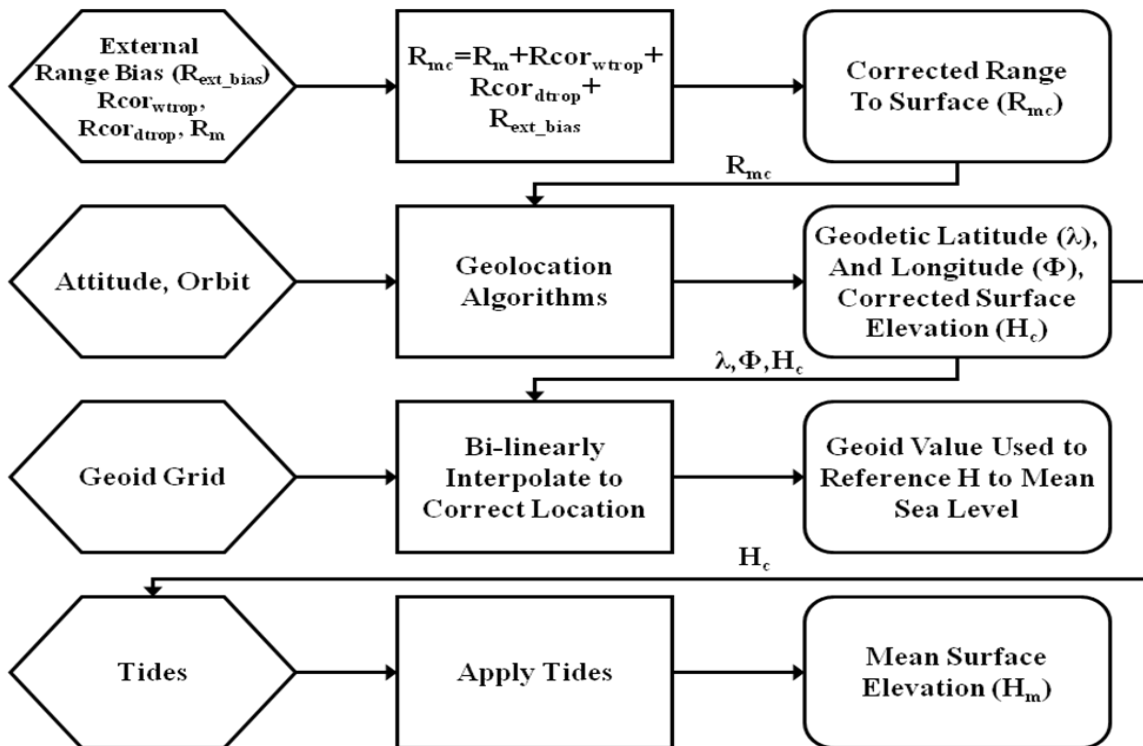


Figure 18 – Correct Range and Calculate Precise Geolocation and Elevation

5.2.3 Calculation of Reflectance

The reflectance is calculated as the ratio of the received energy after it has been scaled for range and the transmitted energy. The unscaled received energy is calculated as the area under the received waveform from sig_beg to sig_end after the noise has been subtracted scaled by the receiver gain and the optical to detector volt efficiency for the receiver pulse. The transmitted energy is calculated as the area under the transmitted waveform scaled by the transmitted gain and the optical to detector volt efficiency for the transmitted pulse.

The equation for the surface reflectivity is:

$$\rho_{surf} = \frac{\rho_{surf_uncor}}{\tau_{RTatm}}$$

$$\rho_{surf_uncor} = \frac{\pi E_{rec} R^2}{E_{trans} A_{telescope} \tau_{opt}} \quad [65]$$

$$\tau_{RTatm} = e^{-2(\tau_c + \tau_a + \tau_m)}$$

where

- ρ_{surf} is the surface reflectivity
- ρ_{surf_uncor} is the uncorrected surface reflectivity
- E_{rec} is the received energy
- R is the range in meters
- E_{trans} is the transmitted energy
- $A_{telescope}$ is the telescope area (0.709 m²)
- τ_{opt} is the optics transmission (67%)
- τ_{RTatm} is the roundtrip atmosphere transmission
- τ_c is the cloud (column) integrated optical depth (one per second)
- τ_a is the aerosol (column) integrated optical depth (once per four seconds)
- τ_m is the molecular optical depth.

The received and transmitted energy are determined by the following procedure:

- Identify the location of the pulse (position of maximum amplitude between signal begin and end).
- Compute the threshold amplitude from the pulse amplitude and the threshold percentage ($thrPcnt_{std}=15\%$, $thrPcnt_{alt}=11\%$).

$$threshold_amp_{rec} = thrPcnt * (pulse_amp_{rec} - mean_noise_{rec}) + mean_noise_{rec} \quad [66]$$

The mean noise for the transmitted pulse is expected to be zero, so:

$$threshold_amp_{trans} = thrPcnt * pulse_amp_{trans} \quad [67]$$

- From the pulse location, find the locations where the waveform amplitude falls below threshold_amp.
- Calculate the sum of the waveform data (A_{pulse} area under waveform above mean noise).
- Calculate the pulse energy as the product of the above sum and a calibration coefficient.

$$E_{pulse} = A_{pulse} * Gain_{pulse} * calib_coef_{pulse} \quad [68]$$

Gain_{trans} will be held constant (over a period of months), and Gain_{rec} will be adjusted every second depending on the maximum received amplitude.

5.2.4 Calculation of the Footprint Orientation

There will be an LCD image of the laser beam for each measurement from which the footprint orientation and shape can be derived. To facilitate further research we request that the shape and orientation of this footprint, calculated as part of the attitude determination process, explained in the GLAS PAD ATBD, be written on the output product for each measurement. Ellipsoid parameters defining the footprint shape and the orientation of the major axis relative to true north are to be saved for this product.

5.2.5 Calculation of Geoid

The EGM96 ellipsoid <http://earth-info.nima.mil/GandG/wgsegm/egm96.html> = File A , is used to calculate the geoid undulation (N) that is put on the products, so the user can convert the ellipsoidal height (h) obtained from altimetry to orthometric height (H), by:

$$H = h - N \quad [69]$$

To implement equation 69 properly, one has to consider:

1. The coordinate frame to which h refers. This is in essence dictated by the orbit determination (station coordinates etc.) which provided the s/c position. The ICESat coordinate system, ITRF, is consistent with the WGS-84 coordinate system origin so there is no correction required due to coordinate origin difference.
2. The permanent tide. Since the altimeter maps the actual crust of the Earth in the presense of Sun and Moon, h is in the Mean-tide system. One should therefore compute N in the same Mean-tide system for use in eq 69.
3. The zero-degree height anomaly. Estimation of this term allows one to convert the height anomaly obtained from EGM96 w.r.t. an "ideal" best-fit mean-Earth ellipsoid (this is "automatically" done when the harmonic summation omits any zero-degree term), to any other ellipsoid and associated normal field.

File A contains geoid undulations from EGM96, in the Tide-free system, with respect to the WGS 84 ellipsoid.

To convert this into the Topex/Poseidon ellipsoid used to reference the elevation on the products, one requires the following.

Let "I" designate "Ideal", "0" designate WGS84, and "1" designate TOPEX/Poseidon (T/P).

Then, the zero-degree height anomaly required to convert from the "Ideal" system to WGS84 is:

$$\xi_z^0 = \frac{GM_I - GM_0}{r\gamma} - \frac{W_I - U_0}{\gamma} \quad [70]$$

Similarly, the zero-degree height anomaly required to convert from the "Ideal" system to the T/P is:

$$\xi_z^1 = \frac{GM_I - GM_1}{r\gamma} - \frac{W_I - U_1}{\gamma} \quad [71]$$

The file: <http://earth-info.nima.mil/GandG/wgsegm/egm96.html> (= File A) contains geoid undulations from EGM96, in the Tide-Free system, with respect to the WGS84 constants. Denote these by N^0 :

$$N^0 = N^I + \xi_z^0 \quad [72]$$

We need the corresponding quantity with respect to the T/P constants. That would be:

$$N^1 = N^I + \xi_z^1 \quad [73]$$

Therefore:

$$N^1 = N^0 + (\xi_z^1 - \xi_z^0) = N^0 + \frac{GM_0 - GM_1}{r\gamma} - \frac{U_0 - U_1}{\gamma} \quad [74]$$

The correction (aside of tide system) to be added to the N^0 that we get from File A is:

$$c = \frac{GM_0 - GM_1}{r\gamma} - \frac{U_0 - U_1}{\gamma} \quad [75]$$

We have:

$$\begin{aligned} GM_0 &= 3.986004418 \times 10^{14} \text{ m}^3 \text{ s}^{-2} \\ GM_1 &= 3.986004415 \times 10^{14} \text{ m}^3 \text{ s}^{-2} \\ U_0 &= 62636851.71 \text{ m}^2 \text{ s}^{-2} \\ U_1 &= 62636858.57 \text{ m}^2 \text{ s}^{-2} \end{aligned} \quad [76]$$

Notice that the value for U_1 ($= 62636858.702 \text{ m}^2 \text{ s}^{-2}$) that is provided in the NASA Pathfinder documentation (NASA/TM-1998-208605) is wrong. From eq 75 and eq 76, one has:

$$c = 70.48 \text{ cm} \quad [77]$$

This correction can also be computed based on geometric principles, as:

$$c = (\xi_z^1 - \xi_z^0) = (a_0 - a_1) - \frac{1}{3}a(f_0 - f_1) \quad [78]$$

We have:

$$\begin{aligned} a_0 &= 6378137.0 \text{ m} \\ a_1 &= 6378136.3 \text{ m} \\ f_0 &= 1/298.257223563 \\ f_1 &= 1/298.257 \end{aligned} \quad [79]$$

Therefore:

$$c = 70.53 \text{ cm} \quad [80]$$

Within the spherical approximation underlying eq 78, the two values eq 77 and eq 80 for the correction c are in agreement. One may adopt:

$$c = 70.5 \text{ cm} \quad [81]$$

The total correction (including the conversion from Tide-Free to Mean-Tide system) required to the values of File A becomes:

$$c_{total} = 70.5 + 1.3(9.9 - 29.6 \sin^2 \varphi) \text{ cm} \quad [82]$$

This c_{total} is to be added to the N^0 values that we get from File A.

$$N_{total} = N^0 + c_{total} \quad [83]$$

This has been done in ground processing from release 18 onward and the geoid value on the products is equal to in the above equation.

5.2.6 Ancillary Information

The science team will provide the 1 km resolution land DEM from the Global 30 Arc-Second Elevation Data Set (GTOPO30) and geoid grids from TBD source for reference on the elevation products. These products will be provided on a latitude and longitude grid and bi-linear interpolation to the location of the footprint is to be used to calculate the specific value associated with each measurement. The LIDAR will provide some information concerning cloud coverage as explained in the GLAS atmospheric ATBDs. Several flags will be set based on this information:

- Flag indicating no cloud layers found
- Flag indicating no aerosol layers found
- Flag indicating that the LIDAR data give evidence of good conditions for forward scattering to occur. This will be based on the lowest cloud layer boundary falling within TBD km of the surface as indicated by the DEM and the optical depth associated with the cloud layer being within TBD bounds. Research is ongoing to try to determine how to set this flag.

5.2.7 Quality Information

- To aid in using this as a research product, there needs to be some indication of whether there was a problem in calculating any of the parameters on the product. For the following parameters this indication is to be a flag set to 0 if there was no problem and set to 1 if any problem occurred in the calculation. Quantities calculated and flags set once per second:
 - Solid earth tides
 - Ocean tides
 - Load tides
 - Geoid interpolation

Quantities calculated and flags set once per measurement:

- Wet troposphere correction
- Dry troposphere correction
- Off-nadir pointing direction
- Satellite position
- Range increments based on the waveform for land
- Range increments based on the waveform for ice sheet
- Range increments based on the waveform for sea ice
- Range increments based on the waveform for ocean

Table 5-2 Parameters to be output every measurement –level 1b elevation product

Parameter Description	Precision
UTC time of laser pulse corrected for system and transit delay from Jan 0 2000	μsec
Altimeter range to the telemetered gate farthest from the spacecraft - reference range = Range_ref (ns) * c/2	mm
Satellite position from the best available POD as a vector in ITRF at the ground bounce time of the measurement	mm
Off-nadir pointing direction (unit vector) in ITRF from the Precision attitude calculation	1.5 arc sec
Geodetic Latitude and longitude calculated using range increment to centroid of maximum amplitude peak with all atmospheric corrections applied	μdeg
Surface Elevation calculated using range increment to centroid of maximum amplitude peak with all atmospheric corrections applied. Tides are applied to the elevation.	mm
Surface Identifier flags from regional ID grid – All 4: l_ocean, l_ice, l_seaice, l_land	N/A
Range increment from reference range to threshold retracker range	mm
Range increment from reference range to signal begin	mm
Range increment from reference range to signal end	mm
Range increment from reference range to ice sheet specific range.	mm
Range increment from reference range to sea ice specific range	mm
Range increment from reference range to land specific range	mm
Range increment from reference range to ocean specific range	mm
Number of peaks from smoothed waveform	N/A
Peak Amplitude from smoothed waveform	counts
Range increment from reference range to centroid of received waveform from signal begin to signal end	mm
Solar incidence angle	.01 deg

Reflectance corrected for round trip atmospheric transmission	
A set of flags indicating problems with any of the parameters to include: waveform-based range corrections, orbit, attitude, and atmospheric delay corrections	N/A
Surface elevation from DEM	cm
Orientation of the laser footprint measured clockwise from true north from attitude determination system	.01 deg
Wet troposphere atmospheric delay correction	mm
Dry troposphere atmospheric delay correction	mm
Length of the major axis of the laser footprint from attitude determination system	cm
Eccentricity of the laser footprint	cm

Table 5-3 Parameters to be output once per second level 1b elevation product

Parameter Description	Precision
Cloud coverage flag from LIDAR products	N/A
Solid earth tide elevation	mm
Ocean tide elevation	mm
Load tide elevation	mm
A set of flags indicating problems with any of the parameters to include: geoid, load tides, solid tides, and ocean tides	N/A
For the atmospheric corrections a flag indicating what source was used.	N/A
Flag indicating aerosol layer (s) were detected in LIDAR data	N/A
Flag indicating conditions for forward scattering to occur were detected in LIDAR data	N/A
Flag indicating cloud layer (s) were detected in LIDAR data	N/A
Geoid	mm

5.3 Ice Sheet Product – GLA12

The level 2 ice sheet product is generated for the ice sheet community with the intent that it be usable by glaciologists as a source of ice sheet elevation and surface characteristics within the limitations of the GLAS system. To this extent, the surface elevation will be calculated using a pre-determined “best” algorithm for ice sheets applying all pertinent corrections and accounting for the time-varying tidal effects. Since this is a level 2 product, the corrections need to be available on the product with enough corresponding information to calculate a new surface elevation if users want to supply their own correction(s). For this same reason all elevations are given relative to a reference ellipsoid and a geoid

elevation is provided for users to reference it to sea level. As with the level 1b elevation product, the corrections and tides that vary at a long wavelength need to be calculated every second and can be linearly interpolated for the correct value to correspond to the 40/sec measurement.

Over most of the ice sheets the return waveform will resemble a simple Gaussian with one peak. There will be exceptions over crevasses and near cliffs and other features where the return will have multiple peaks. Multiple peaks can also occur due to low clouds or ice fog. The main requirement of ICESat is to measure elevation changes. This requires that a mean elevation be associated with each ice sheet measurement. Therefore when there are multiple peaks, the range will be calculated based on the position of the centroid of the maximum amplitude peak. The increment in range between the maximum amplitude and first peaks needs to be tabulated also so users can recalculate the surface elevation based on the first peak if conditions warrant it. The number of peaks needs to be indicated so the user can tell how complicated the surface was. This product should also contain X^2 of the received waveform to the functional fit as an indication of surface or transmit pulse irregularities that the user may want to research further using the lower level products. The range to the centroid of the received waveform and the ranges to the beginning and end of signal, and the skewness and kurtosis of the received waveform need also be supplied so the user can use these to look for surface characteristics specific to their research.

All flags present in the level 1b elevation product that affect the ice sheet surface elevations need also be provided along with the ancillary information discussed in 5.2. Table 5-5 lists the parameters to be supplied every measurement. The parameters to be output every second are the same as those listed in Table 5-3.

Table 5-4 Offset Used For Latitude, Longitude and Elevation Calculations

	Maximum Amplitude Peak	Centroid
GLA06	X	
GLA12	X	
GLA13	X	
GLA14		X
GLA15	X	

Table 5-5 Parameters to be output every measurement-level 2 ice sheet product

Parameter Description	Precision
UTC time of laser pulse corrected for system and transit delay from Jan 0 2000	μsec
Altimeter range to telemetered gate farthest from the spacecraft - reference range	mm
Range increment from reference range to threshold retracker range	mm
Satellite position from the best available POD as a vector in ITRF at the ground bounce time of the measurement	mm
Off-nadir pointing direction (unit vector) in ITRF from the Precision attitude calculation	1.5 arc sec

Geodetic Latitude and longitude calculated using ice sheet-specific range with all atmospheric corrections and tides applied	μdeg
Surface Elevation calculated using the ice sheet-specific range with all atmospheric corrections and tides applied	mm
Surface Identifier flags from regional ID grid – All 4: l_ocean, l_ice, l_seaice, l_land	N/A
Range increment from reference range to signal begin	mm
Range increment from reference range to signal end	mm
Range increment from reference range to produce ice sheet specific range based on the maximum amplitude peak in the return	mm
Range increment from reference range to produce ice sheet specific range based on the first peak in the return	mm
Standard deviation of received waveform to fit using ice sheet parameters	.01 counts
Solar Incidence Angle	.01 deg
Number of peaks from Gaussian fit	N/A
Peak Amplitude from smoothed waveform	counts
Kurtosis of the received waveform from signal begin to signal end	.01
Skewness of the received waveform from signal begin to signal end	.01
Range increment from reference range to centroid of received waveform	Mm
Uncorrected Reflectance	.000001
Reflectivity Correction Factor (corrects for atmospheric effects)	.000001
A set of flags indicating problems with any of the parameters to include: waveform-based range corrections, orbit, attitude, and atmospheric delay corrections	N/A
Surface elevation from DEM	cm
Orientation of the laser footprint measured clockwise from true north from attitude determination system	.01 deg
Wet troposphere atmospheric delay correction	mm
Dry troposphere atmospheric delay correction	mm
Length of the major axis of the laser footprint from attitude determination system	cm
Eccentricity of the laser footprint from attitude determination system	cm

5.4 Level 2 Sea Ice Product – GLA13

The sea-ice algorithm is designed to provide estimates of:

- a. Average range to the surface of smooth or randomly rough ice or of open water within the footprint will be inferred from the time delay of the centroid of the best-fit Gaussian associated with the maximum amplitude peak in the return pulse. For sea ice, this elevation will be slightly above the local sea surface, and time series of such data might provide an indication of the temporal variability of sea-ice freeboard during the period of the mission if we also have information on temporal variability of sea-surface elevation in the same regions. For orbit tracks crossing open-water leads and polynas, it should be possible to estimate the freeboard of surrounding sea ice, giving an indication of sea-ice thickness (Wadhams et al, 1992), as proposed by Peacock et al, (1998) using satellite radar-altimeter data.
- b. Average range to all surfaces in the footprint will be inferred from the time delay of the centroid of return waveform above noise threshold. For smooth and randomly rough sea ice and for open water, this should be almost identical to (a). The difference between (a) and (b) gives an indication of whether a significant fraction of the footprint is occupied by a large ice ridge or an iceberg, causing an asymmetric, non-Gaussian return waveform.
- c. Sea-ice surface roughness estimates were to have been obtained from the RMS width of the whole return pulse as well as from the RMS width of best-fit Gaussian associated with its latest peak. The first is a measure of the total surface elevation variation, and the latter a measure of the roughness of the smooth ice or of open ocean surface within the footprint. See appendix 1 for information on why this could not be accomplished.
- d. Range to the highest surface in the footprint will be inferred from the time delay of the centroid of the best-fit Gaussian associated with the first peak in the return waveform. This indicates the highest large roughness element, or surface of iceberg, floating glacier tongue, or land within the footprint.
- e. Average reflectivity within the footprint will be obtained from the total energy in the return pulse, taking account of the transmitted energy, height of spacecraft, receiver characteristics etc.

Table 5-6 Level 2 sea-ice parameters to be output every measurement

Parameter Description	Precision
UTC time of laser pulse corrected for system and transit delay from Jan 0 2000	μsec
Altimeter range to telemetered gate farthest from the spacecraft - reference range	mm
Range increment from reference range to threshold retracker range	mm
Satellite position from the best available POD as a vector in ITRF at the ground bounce time of the measurement	mm
Off-nadir pointing direction (unit vector) in ITRF from the Precision attitude calculation	1.5 arc sec
Geodetic latitude and longitude calculated using sea ice-specific range with all atmospheric corrections and tides applied	μdeg
Sea-ice surface elevation calculated using the maximum amplitude peak of the waveform, with all atmospheric corrections and tides applied	mm

For waveforms with more than one peak, 'iceberg' elevation calculated using the first peak in the waveform, with all atmospheric corrections and tides applied	mm
Average elevation of all surfaces in the footprint from the centroid of the received waveform, with all atmospheric corrections and tides applied	mm
Surface Identifier flags from regional ID grid – All 4: l_ocean, l_ice, l_seaice, l_land	N/A
Range increment from reference range to signal begin	mm
Range increment from reference range to signal end	mm
Range increment from reference range to produce sea ice specific range based on the maximum amplitude peak in the return	mm
Range increment from reference range to produce sea ice specific range based on the first peak in the return	mm
Standard deviation of received waveform to fit using sea ice parameters	.0001 volts
Solar incidence angle	.01 deg
Number of peaks from smoothed waveform	N/A
Peak amplitude from smoothed waveform	.0001 volts
Skewness of the received waveform from signal begin to signal end	.01
Range increment from reference range to centroid of received waveform between signal begin and signal end	mm
Reflectance corrected for round trip atmospheric transmission	.000001
A set of flags indicating problems with any of the parameters to include: DEM, waveform-based range corrections, orbit, and attitude	N/A
DEM	cm
Orientation of the laser footprint measured clockwise from true north from attitude determination system	.01 deg
Length of the major axis of the laser footprint from attitude determination system	cm
Length of the minor axis of the laser footprint from attitude determination system	cm

5.4.1 Ancillary Information

In addition to the information needed to correct measured ranges for atmospheric effects, and to locate the footprint, these sets of information will be required:

- a. Sea-ice mask, defined from the GSFC SMMR-SSM/I ice concentration data
- b. Land mask, to include most recent estimates of the seaward margins of icebergs and glaciers. For Greenland and Antarctica, this could probably best be obtained from available SAR imagery. For

other land masses, the best-available sources should be used. Sea-ice products should be produced for all ocean and lake areas included within a mask bounded by the lowest latitude of sea-ice extent plus 50 km, and excluding land areas.

Users may find it useful if the following parameters are archived with each GLAS sea-ice product: Mean sea surface and geoid for high latitudes, with best estimates of sea-surface height variability. For much of the Arctic, this can probably be obtained from work done by S. Laxon and his group at Mullard Space Science Laboratory (Personal communication from S. Laxon, November, 1998).

5.5 Level 2 Land Product – GLA14

Because of the potential complexities of land returns, the level 2 land product is intended to describe the waveform in a way that, in combination with independent knowledge of, or assumptions about, local relief and land cover interpretations can be made regarding elevation, slope, roughness, and vegetation and/or cultural feature height. To this end, a land-specific range is defined which is the centroid of the received waveform signal between the defined signal start and signal end. This land-specific range is used for computation of the final Geolocated Latitude and Longitude and Footprint Elevation. Absent independent information this is the best, most representative elevation for the land. Range offsets from this land-specific range to the start and end of signal are to be provided that, in combination with the provided laser pointing vector, can be used to compute the elevation of the highest and lowest detected features within the footprint. For the most common orientation (nadir pointing) the range offsets are equivalent to elevation offsets. Similarly range offsets from the land-specific range to the centroid for each of the Gaussian distributions fit to the waveform peaks is to be provided. This includes up to 6 Gaussian fits. Where more than 6 peaks were fit to the waveform (anticipated to be rare), the fit to the 6 most significant fits (based on the area of the Gaussian distributions) are to be used. The one sigma width of each Gaussian fit, converted to units of range, and the amplitude and area of each of the Gaussian fits is also to be provided. From these data the Gaussian fit approximation of the waveform can be recreated along the laser pointing vector positioned with respect to the geolocated land-specific range. Inferences can then be made, in conjunction with independent knowledge or assumptions, about how, and if, the return signal is separated into surface, vegetation and cultural feature components. With these inferences, measures of surface elevation and relief and vegetation and/or building height can be derived. In order for the user to know how robust the Gaussian fits conformed to the waveform, χ^2 and standard deviation measures of the fit to the waveform should be provided. For cases of 6 or fewer fits these measures will be equivalent. In order to provide model measures of slope and roughness, the ice sheet algorithms assuming no-roughness and no-slope end-members was to have been applied. These algorithms were to have been applied to the Gaussian fit to the last (lowest) peak. See appendix 1 for an explanation for the removal of slope and roughness from the products. Last peak model results are provided for those cases where it is inferred that the last peak corresponds to the surface beneath vegetation and/or cultural features. Full peak model results are also provided for those cases where it is decided that no vegetation and/or cultural features are present, or where it is decided that multiple components in the footprint have not been reliably separated in the waveform. Additional parameters are provided analogous to those provided for the ice sheet product.

Table 5-7 Lists the Level 2 land parameters to be output for every measurement. In addition, the same parameters as found in Table 5-3 for ice sheets need to be output once per second.

Table 5-7 Parameters to be output every measurement for level 2 land product

Parameter Description	Precision
UTC time of laser pulse corrected for system and transit delay from Jan 0 2000	μsec

Altimeter range to farthest telemetered gate from the spacecraft-reference range	mm
Range increment from reference range to threshold retracker range	mm
Satellite position from the best available POD as a vector in ITRF at the ground bounce time of the measurement	mm
Off-nadir pointing direction (unit vector) in ITRF from the Precision attitude calculation	1.5 arc sec
Geodetic Latitude and longitude calculated using land-specific range with all atmospheric corrections and tides applied	μ deg
Surface Elevation calculated using the land-specific range with all atmospheric corrections and tides applied	mm
Surface Identifier flags from regional ID grid – All 4: l_ocean, l_ice, l_seaice, l_land	N/A
Range increment from reference range to signal begin	mm
Range increment from reference range to signal end	mm
Range increment from reference range to land- specific range	mm
Range increment from reference range to centroid of Gaussian fits (6 elements)	mm
One-sigma width of Gaussian fits (6 elements)	mm
Amplitude of Gaussian fits (6 elements)	.0001 volts
Area of Gaussian fits (6 elements)	.01 volts x ns
Standard deviation of received waveform using all fits	.01 counts
Standard deviation of received waveform using stored fits	.01 counts
Solar Incidence Angle	.01 deg
Number of peaks from smoothed waveform	N/A
Peak Amplitude from smoothed waveform	.0001 volts
Skewness of the received waveform from signal begin to signal end	.01
Reflectance corrected for round trip atmospheric transmission	.000001
A set of flags indicating problems with any of the parameters to include: DEM, waveform-based range corrections, orbit, and attitude	N/A
DEM	cm
Orientation of the laser footprint measured clockwise from true north from attitude determination system	.01 deg
Length of the major axis of the laser footprint from attitude determination system	cm
Length of the minor axis of the laser footprint from attitude determination system	cm

5.6 Level 2 Ocean Product – GLA15

The ocean algorithm is designed to provide estimates of:

- a. Average elevation of each footprint.
- b. Highest and lowest elevations within each footprint.
- c. The product of reflectance and the roundtrip atmospheric transmission of each footprint.
- d. Mean elevation over 1 sec segment.

‘Ocean’ data will be as determined from the global DEM, to include all regions larger than, say 1000 sq km that are at sea level. Thus, ‘ocean’ tracking will be implemented over large lakes and over sea ice, in addition to the special tracking appropriate to these areas.

Table 5-8 lists the ocean parameters to be provided every measurement; parameters listed in Table 5-3 will be provided every second.

Table 5-8 Level 2 ocean parameters to be output every measurement

Parameter Description	Precision
UTC time of laser pulse corrected for system and transit delay from Jan 0 2000	μsec
Altimeter range to farthest telemetered gate from the spacecraft-reference range	mm
Range increment from reference range to threshold retracker range	mm
Satellite position from the best available POD as a vector in ITRF at the ground bounce time of the measurement	mm
Off-nadir pointing direction (unit vector) in ITRF from the Precision attitude calculation	1.5 arc sec
Geodetic latitude and longitude calculated using ocean-specific range with all atmospheric corrections and tides applied	μdeg
Ocean surface elevation calculated using the centroid of the waveform, with all atmospheric corrections and tides applied	mm
Highest elevation in the footprint, with all atmospheric corrections and tides applied (corresponds to signal begin)	mm
Lowest elevation in the footprint, with all atmospheric corrections and tides applied (corresponds to signal end)	mm
Elevation associated with maximum amplitude Gaussian	mm
1-sec Elevation calculated using a linear filter to the full rate (40/sec) ocean elevations with all atmospheric corrections and tides applied	mm
RMS of the full rate elevations that went into calculation of the 1-sec elevation	mm
Surface Identifier flags from regional ID grid – All 4: l_ocean, l_ice, l_seaice, l_land	N/A

Range increment from reference range to signal begin	mm
Range increment from reference range to signal end	mm
Range increment from reference range to produce ocean specific range based on the maximum amplitude peak in the return	mm
Range increment from reference range to produce ocean specific range based on the first peak in the return	mm
Standard deviation of received waveform to fit using ocean parameters	.01 counts
Solar incidence angle	.01 deg
Number of peaks from smoothed waveform	N/A
Peak amplitude from smoothed waveform	counts
Skewness of the received waveform between signal begin and signal end	.01
Range increment from reference range to centroid of the received waveform between signal begin and signal end	mm
Reflectance	.000001
A set of flags indicating problems with any of the parameters to include: DEM, waveform-based range corrections, orbit, and attitude	N/A
DEM	cm
Orientation of the laser footprint measured clockwise from true north from attitude determination system	.01 deg
Length of the major axis of the laser footprint from attitude determination system	cm
Length of the minor axis of the laser footprint from attitude determination system	cm

5.6.1 Ancillary Information

In addition to the information needed to correct measured ranges for atmospheric effects, and to locate the footprint, these sets of information will be required:

- a. Ocean mask, including sea-ice covered areas
- b. Geoid elevation, with a tidal model to permit correction of geoid elevation to a sea-surface elevation appropriate to the time of GLAS footprints

6.0 Constraints, Limitations, and Assumptions

This section speaks to the effect on the derived physical surface properties and elevation of the constraints, limitations, and assumptions that have been used to develop the algorithms presented in this document. Also discussed are research studies that need to be carried out to better understand the effect of these assumptions on the products.

6.1 Surface Characteristics

All the algorithms presented assume a Gaussian distribution of the surface undulations. Over the ice sheets the slope algorithm assumes a linear slope within the footprint and over sea ice the roughness algorithm assumes no slope. Actual ice sheet, sea ice and land surfaces do not behave as assumed though to first order these assumptions are valid over the ice sheets and sea ice. In addition to non-Gaussian uniform undulations there are many sudden irregularities in the surface all of which contribute to errors in the slope, roughness, and surface elevation calculated using our algorithms.

6.1.1 Effect on Slope Calculations

The algorithm for calculating the slope within the laser footprint was based on the assumption that the slope is linear at the 70m level and therefore the maximum and minimum surface heights lie on opposite edges of the footprint. The error in the slope calculated using this algorithm could be as great as 100% if, for example, a uniform mound is centered in the footprint. We rely here on an assertion that the spectrum of surface irregularities has a minimum at wavelengths of a few hundred meters. For ice sheets, this theoretically appears to be valid, since these wavelengths are too long for wind-caused features and too short to reflect subglacial topography. We need to study the existing aircraft laser data over Greenland for information on the spectrum of surface irregularities that exist over the ice sheets and use the results in the GLAS simulator to obtain realistic error envelopes for this calculation. See appendix 1 for an explanation for the removal of slope and roughness from the products.

6.1.2 Effect on Roughness Calculations

The algorithm used to calculate the roughness over the sea ice and ice sheet surfaces assumed a pure Gaussian distribution. The actual surface has roughness characteristics that presumably lie somewhere between a Gaussian distribution of irregularities and a uniform distribution of linear wave-like features with a single amplitude. As mentioned previously, surface roughness and slope cannot be empirically solved for from the information provided in one measurement.

Over ice sheets, crevasses introduce a disturbance of the surface that can affect the roughness calculation. In most crevassed regions most of the illuminated spots on the surface will fall between individual crevasses and will therefore not be affected at all. Where the spot overlaps the edge of an open crevasse there are multiple returns from different levels of a discontinuous surface. In cases where crevasses, ridges, vegetation or buildings (as could occur over land) cause multiple peaks in the return, no meaningful value for roughness could be calculated. However, it should be possible to devise an algorithm to filter out such returns. The existence of multiple peaks and or large discrepancies between the functional fit and the waveform, both of which are carried on the level 1 and 2 elevation products, can be used to filter out regions where these surface irregularities are present. This can also be used by glaciologists to point them to crevasse regions where the waveforms and other products from GLAS may be used to better understand the crevasse distribution (see appendix 1 for an explanation for the removal of slope and roughness from the products).

The roughness calculation over sea ice assumes a horizontal surface. This is not always locally the case, causing similar problems to those encountered over grounded ice: pulse broadening caused by roughness and that caused by the slope of the surface cannot be separated without additional information. However, large slopes are rare, and a sloping sea-ice surface within the footprint will be caused by some larger-scale undulation that can reasonably be included as a roughness feature.

Real surfaces exhibit anisotropy and non-stationarity. Our algorithms assume isotropy and stationarity. Isotropy means that the statistics of the surface is independent of the direction along the surface. Stationarity means translational invariance, so that the statistics of one section of the surface will be the same as the statistics determined from a different section of the same surface. As the laser beam has a Gaussian or near-Gaussian far field pattern, the central part of the footprint receives more

energy. Pulse spreading is determined by weighting the elevations with the normalized intensity cross section of the laser beam as described by Gardner (1982). Thus, surface roughness computed from the waveform is most representative of conditions near the middle of the footprint. This should not have any significant impact on roughness statistics derived from many footprints.

A non-uniform reflectivity distribution could affect sea ice roughness calculations. Sea ice reflectivity may vary greatly inside the laser footprint, especially during the summer melting season. Initial results (Csathó and Thomas, 1995) suggest that although the reflectivity distribution has a profound influence on the shape of the waveform, its RMS width is the same for models with different reflectivity distribution but the same topography.

The effect of other factors, such as non-Lambertian reflectivity, non-Gaussian far field pattern etc. requires further study, but is not expected to be large.

Penetration of the beam will also affect the roughness calculation. Although the light signal does not penetrate the ice-sheet signal nearly as deeply as the signal from a radar altimeter, there nevertheless may be penetration that must be evaluated. Experiments in Greenland show that there is still measurable 1064-nm energy from sunlight at a depth of 50 mm below the surface in Greenland (A. Nolin, personal communication, 1996). This effect has not yet been evaluated quantitatively, but at a first guess we can estimate that volume scattering from within the upper 0.1 m of the firn will broaden the return pulse by an amount comparable to that produced by a 0.1 m roughness. This is another error source that the GLAS Team will be evaluating further. See appendix 1 for an explanation for the removal of slope and roughness from the products.

6.1.3 Effect on Surface Elevation

Small amplitude roughness and slopes will cause a broadening of the return pulse. Multiple surface elevations within the footprint will cause the return waveform to be a sum of the Gaussian-type distribution from each surface elevation present within the footprint. Most of the ice sheet surface returns will contain a single pulse. No matter what the shape of the return, if we ignore forward scattering, which is discussed in Section 6.3, the mean surface within the footprint is calculated using the centroid of the return waveform. However, the main mission requirement is to calculate elevation changes over the ice sheets. Therefore we need to take into account how the calculation of the elevation for each measurement affects our ability to calculate elevation change.

Measuring elevation changes requires comparing multiple elevation measurements over the same location at different times. The ICESat ground track passes over the same location for two types of circumstances; 1) when an ascending pass crosses a descending pass, referred to as crossovers and 2) when the orbit repeats itself (for GLAS the main mission will consist of six repeat cycles of 183 days each). Due to instrument characteristics and laser pointing accuracy and knowledge, even when the ICESat ground track overpasses a previous ground track, the portion of the surface illuminated will be different.

For repeat passes, the project is considering dynamic pointing control to maintain the footprint as close as possible to footprints from corresponding repeats. The precision of the pointing control is 30 arc sec or 87 m on the ground with post-processing expecting to improve the knowledge of the pointing to 1.5 arc sec or 4.4 m. The footprint is expected to look like an irregularly shaped ellipse with a major axis of 70m. The irregularities and the orientation of the major axis of the ellipse are expected to change slowly with time. Therefore for repeat passes, the footprints may overlap some, but still will not be illuminating the exact same portion of the surface.

At crossover locations, it will be necessary to interpolate between measurements that are approximately 175 m apart and have an error in location of 4.4m due to the accuracy of the pointing knowledge. In addition, crossovers on the same tracks from different repeats will be calculated from footprints that are offset from each other.

The main challenge in calculating elevation changes from GLAS is to find a method to calculate the surface elevation from the measurement that is as insensitive as possible to small-scale topography at the shot spacing level. Several different methodologies can be used to decide where to calculate the range. These include 1) for multiple peaks taking the average of the centroid positions of the multiple Gaussian fit, 2) for single peaks taking the centroid of the Gaussian fit, 3) taking the centroid of the peak closest to the ground, and 4) taking the centroid of the received or smooth return. More research needs to be carried out to test what method will give the most repeatable results for repeat groundtracks and crossovers.

6.2 Instrument Effects

One effect the instrument will have on the algorithms is in the shape of the transmitted pulse. The engineers (J. Abshire and X. Sun personal communication 1999) have told us that after it comes through the detector for all practical purposes it will be Gaussian. If this pulse is not circularly symmetric, the returned pulse-shape will contain a bias toward the part of the footprint illuminated by an excess of energy. This bias would cause an error in the surface elevation calculated using our centroid algorithm over sloping surfaces. J. Abshire (personal communication, 1995) has calculated as an extreme case that a side lobe containing 10% of the outgoing energy on one edge of the beam would cause an error in a centroid detector of surface height of 18 cm on a surface with a 3deg slope. This is about 5% of the height difference across the footprint.

For a flat surface of uniform roughness the error in the roughness calculation would be extremely small, because the entire footprint is illuminated at essentially the same instant.

Detector saturation has also been shown during the calibration period to be a problem. It sometimes caused clipping of the main return and always causes ringing after the main signal. The centroid of the maximum amplitude gaussian has been chosen to represent the mean elevation in order to offset the problem of picking the ringing due to saturation as a peak. Tuning the fitting procedure to fit the leading edge is also done to reduce the effect of clipping.

6.3 Atmospheric Effects

When there are thin clouds or aerosols in the atmosphere such that there is atmospheric interference with the light beam, yet a significant fraction of the signal is transmitted through the atmosphere so that a return is received at the GLAS telescope, there may be a broadening of the return pulse due to forward scattering of the light. Forward scattering produces ray paths that are slightly longer than the straight-line path and thus produces a delayed arrival of some energy. This has the effect of broadening the pulse and causing the tail to be longer and higher than the leading edge.

Our surface-slope/roughness algorithm is based on pulse broadening, so forward scattering, if not recognized, will lead to overestimates of the roughness and/or slope. Preliminary calculations by J. Spinhirne (personal communication, 1996) suggest that the broadening could be on the order of 1 ns. An error of this magnitude would lead to an overestimate of the roughness by 0.15 m, a figure that is comparable to the expected real values. The error in the slope from a 1-ns broadening would be about 0.1, again a significant factor in the central parts of the ice sheets where the actual slopes are of the same order.

The elevation calculation can also be significantly affected. As presented in the section 4.3.2, this effect can be minimized by using the centroid of the Gaussian fit to calculate the range.

Forward scattering will have to be dealt with, either by correcting for its effects or deleting data that are affected. The GLAS Science Team is supporting research in the area. Results to date show that there is insufficient atmospheric information from the LIDAR to model the forward scattering effect. However, we can tell from the LIDAR when conditions are present that could cause forward scattering and a flag is placed on the level 1 and 2 elevation products indicating this.

APPENDIX 1, INABILITY TO COMPUTE SLOPE AND ROUGHNESS

A study performed by the GLAS Precision Range Determination (PRD) group demonstrated that the theoretical algorithm would not work without actively measured parameters for previously constant values that were found to change with time and laser. The PRD group (led by David Harding/GSFC) modified the algorithm. After implementation it was found that low slopes were overestimated and the theoretical algorithm was limited to perfect returned echoes of a perfect transmit pulse. For GLAS it was observed that the slope and roughness computations in areas of low slope were dominated by a unexplained slight return pulse broadening. So the PRD recommended: “**Do not report slope and roughness in Level 2 GLA products.**” Therefore the parameters are set to invalid and were removed from product structures in later releases. Slope and roughness should be viewed as R&D for interested users to pursue.

The problems are intractable. The error sources make quantitative estimates suspect and the complexities make meaning of quantitative estimates obscure. Below is a list of some of the prime issues/concerns that are unresolved.

- Convolved broadening is due to both within-footprint slope and roughness
- Footprint shape and orientation effect slope calculation
- Field-of-view shadowing effects slope calculation
- Waveform saturation effects slope and roughness calculations
- Atmospheric forward scattering effects slope and roughness calculations
- Slope calculation very sensitive to Gaussian fit width errors for low slope surfaces
- Unknown cause of pulse broadening is introducing bias for flat, smooth surfaces

APPENDIX 2, REL 33 PARAMETERS INPUT FROM ANCILLARY FILE

Numerical Program Parameters		Alternate (Land) Rel 33 values	Standard (Ice sheet, sea ice, ocean) Rel 33 values
$\delta\sigma$ _check (dSgmCk)	Change in width of Gaussian in %; check for convergence in functional fit	0.02	0.02
δ Amp_check (dAmpCk)	Amplitude of peak of Gaussian in %; check for convergence in functional fit	0.02	0.02
δ tm_check (dTmCk)	Change in location of peak of Gaussian in %; check for convergence in functional fit	0.02	0.07
$\delta\epsilon$ (dNoise)	Change in noise level in %; check for convergence in functional fit	0.02	0.02
absMinAmp	Absolute minimum amplitude	0.05	0.05
beg_nSig end_nSig	Noise thresholds for the beginning and ending of the signal in the received waveform threshold = nsig * σ noise_ob	3.5 - 7.5 4.5 - 7.5 (see appendix 3)	9.5 - 15.0 9.5 - 15.0
dprox	Fraction of peak sigma proximity to signal_begin or signal_end allowed during fit	0.0	0.25
fltrWdBeg	Recommended starting width for filter used to smooth the waveform (ns)	14	33
intv_min	Peaks that are closer together than intv_min will be merged/combined.	15	30
maxDeltas_a	max change in amplitude during fit = this value * amplitude parameter	0.5	0.5
maxDeltas_l	max change in peak location during fit = this value	15.0	15.0
maxDeltas_n	max change in noise during fit = this value * noise parameter	0.0	0.0
maxDeltas_s	max change in sigma during fit = this value * sigma parameter	0.5	0.5
maxfit	Max number of fits allowed	6	2
maxGoodSDev	Max value for good standard deviation of fit – one value Used for standard fit, if the standard deviation of the fit is greater than this, then another try is made using a different estimate for the a priori fit parameters	0.06	0.04
maxiter	Maximum number of iterations for fit	12	12

maxNdxNSat	When estimating sigma, if i_satNdx <= this value, then sigma is not recalculated as one saturated peak.	20	0
N_peak_min	A peak in the waveform is considered as possibly real if its peak amplitude is > N_peak_min * σ noise_ob + Noise_ob	4.5	4.5
nGates2use	The number of gates used to calculate the noise value for the received waveform, if nscal is set.	20	20
offsetb	The offset to subtract from the beginning of the waveform before the first threshold crossing if slctregn is set (ns)	50	50
offsete	The offset to add to the end of the waveform after the last threshold crossing if slctregn is set (ns)	50	50
Stdev(σ_m) (V0sgm)	The aprioi standard deviation of the σ_m parameter in functional fit	0.001	0.001
Stdev(Amp) (V0amp)	The aprioi standard deviation of the amplitude in the functional fit	0.001	0.001
Stdev(noise) (V0ns)	The aprioi standard deviation of the noise in functional fit	1000000.0	1000000.0
Stdev(tm) (V0loc)	The aprioi standard deviation of the peak position in functional fit	0.1	0.1
Thresh_lvl	The % of the maximum amplitude to use for defining the threshold retracker location.	0.11	0.15
wfFitSDevThr	chi threshold for convergence of fit if convsw is set	0.001	0.00001
wt_sgm	Measurement uncertainty for computing weights for LsqFit	0.03	0.001
Not Surface Dependent			
areaTele, optTrans	area of telescope and optical transmission. Used to compute reflectance	0.78539816 0.67	
cmb(2)	Used to combine peaks (0,1)=weighted by area, (1,0)=straight average	(0,1)	
f_BSS	array of factors (multiply d_reflectUncorr by this)	0.95 - 1.70 (see appendix 3)	
fltrWdMax	The maximum width of the filter used to smooth the waveform (ns)	129	
fltrWdMin	The minimum width of the filter used to smooth the waveform (ns)	4	
GainAlertLevel	set gain flag in i_ElvFlg if gain is >= this value	30	
maxAmp	Maximum amplitude of Gaussian – one value	2.5	
maxSDev	Maximum value for d_wfFitSDev and d_sDevFitTr - one value	0.3	

maxSigma	Maximum value allowed for Gaussian sigma – one value	300.0
maxSmBins	Maximum number of bins in the smoothing filter	129
minIter	Min number of iterations during functional fit – one value	3
minNG2use	The minimum number of gates to use if the signal is within ngates2use of the beginning or ending of the waveform - one value	10
minNG2useTr	The minimum number of gates to use to calculate noise if the transmitted pulse is within ngates2usetr of the begin or end.	10
minNoise	Min noise	0.5
minPk2ns	Minimum peak to noise ratio ((maxAmp - noise)/sDevNoiseOb) - one value if not met, WFqual(gwi_suspect) is set	5.0
minSigWdth	Minimum signal width (signal_end - signal_begin) for a good fit - one value if not met, WFqual(gwi_suspect) is set	5.0
n_BSS	number of entries in BSS (Boresight Shift Shadowing) Table	15
nGates2useTr	The number of gates used to calculate noise for the transmitted pulse.	10
nlgc	non-linear gain calibration constants	0.72807d0 0.008543d0 -9.6905d-5 4.7896d-7 -8.621d-10
nSigTx	The noise threshold for the transmitted pulse is d_nsigTx * sDevNsTx (one value)	1.5
ovrCalib	ground calibration for reflectance	0.0d0 0.862068965d0
QA_dump_time	along track dumping interval in seconds	16
satNdxTh	Used for counting the saturation index - one value If the raw amplitude of a gate is >= this value, then i_satNdx is incremented	30 - 239 (see SAT_TH in appendix 3)
sigmaMInit	Min value for peak sigma	2.5
t_BSS	array of effective time in ns	see D_T_BSS in appendix 3

Program Switches		Alternate (Land) Rel 33 values	Standard (Ice sheet, sea ice, ocean) Rel 33 values
convSw	Method of convergence switch (0: parameter change, 1: chi change)	1	0
estSw	0: recompute estimated peak amplitudes by subtracting contribution from other pks 1: don't recompute	0	1
keepAllPks	1: don't remove peaks if too narrow, too small, or too close	1	0
keepPk1	1=keep peak #1 in estimates even if its rank is more than i_maxfit	1	0
Noisecal (nsCal)	1: calculate noise level and σ from waveform 0: use noise level and σ telemetered	0	0
normWF	1: normalize WF during fit	1	0
normType	Type of normalization if normWF is set (0: area, 1: max peak amplitude)	1	0
slctRegn	1: select region of waveform from which to do evaluation 0: use all the gates telemetered in waveform evaluation	1	0
stopAt6	1: during the estimating process, stop combining close peaks when the number of peaks is ≤ 6	0	0
throwOutZA	1: remove peak if zero amplitude and keepallpks==1	1	0
tmCkSw	0: use dTmCk as percent, 1: use dTmCk as ns	0	1
Instrument Parameters (1 each)			
filterWdMax (d_fltrWdMax)	The maximum width of the filter used to smooth the waveform (ns)	129	
ΔT_{hires} (dTHiRes)	Time between gates for the highest resolution gate – nominally 1 ns	in anc33 0.999999988647 27d0 to 1.0000000325d0	

Parameters Input From the Data Stream (GLA01)

APID_AvFlg	0=data is present
comp_type	0 = N, P, and Q compression; 1 = R compression
d1_pred_lat	Predicted latitude
d1_pred_lon	Predicted longitude
EchoLandType	0=ocean, 1=land, 2=seaice, 3=icesheet

engineering	Temperatures
Filter_ob (filtnum)	on board filter used to find signal
Gain_rec (gainSet1064)	the receiver gain
Gain_trans (ADdetOutGn)	Gain on the transmitted pulse
GPSshotTime	GPS shot time
InstState	Which detector, digitizer & laser
N (N_val)	the number of samples using the P compression ratio
Ngates	number of gates telemetered – nominally 544 for land and ice sheet, 200 for ocean and sea ice
Noise_ob (4nsBgMean)	background noise level as measured by the instrument
P (compRatio)	the compression ratio used on board for the last N Wf(t) samples when comp_type is 0
Q (compRatio)	the compression ratio used on board for Wf(t) samples 1 to Ngates-N when comp_type is 0
R (R_val)	The compression ratio applied to all samples when comp_type is 1
RecNRGAll_EU, RecNrgLast_EU	Received energy for all of the signal above threshold, received energy for the peak with the maximum amplitude
samp_pad	Surface echo padding
Time _{FC} (I) (TxWfStart)	Fire Cmd time for shot I linked to internal GLAS clock – time the digitizer is commanded to begin
T _{ngates} (RespEndTime)	Digitizer address (ns) of last gate telemetered of the return pulse (farthest from spacecraft)
T _p (TxWfStart)	Digitizer address (ns) of the location of the peak of the transmitted pulse
TxFlg	0=the transmitted pulse was telemetered
TxNrg_EU	Transmitted energy
Wf (t) (rng_wf)	the received waveform (544 samples in land or ice sheet mode, 200 samples in ocean or sea ice mode)
Wf_trans(t) (tx_wf)	Transmitted pulse waveform

APPENDIX 3, REL 33 ANC07, WAVEFORM CONSTANTS

```
# anc07_001_01_0004.dat          Version 33
# Waveform Constants Mod Entries
#
BEG_OF_WF = -----
WF_VERS = ANC07 WF V6.0 2011-03-08
#
# Select Region "0==use all gates, 1==use selected region"
I_SLCTREGN1 = 1
I_SLCTREGN2 = 0
#
# "If i_slctRegn? is set, indexSignalBegin? = indexSignalBegin? - i_offsetb?"
I_OFFSETB1 = 50
I_OFFSETB2 = 50
#
# "If i_slctRegn? is set, indexSignalEnd? = indexSignalEnd? + i_offsete?"
I_OFFSETE1 = 50
I_OFFSETE2 = 50
#
# Min # of gates equal to 255 to set the clipped flag in l_WFqual
I_MIN4CLIP=2
#
# Min number of iterations during functional fit
I_MINITER = 3
#
# Max number of iterations during functional fit
I_MAXITER1 = 12
I_MAXITER2 = 12
#
# Max number of peaks to fit - alternate & standard parameters
I_MAXFIT1 = 6
I_MAXFIT2 = 2
#
# Min filter width used by WFMgr for sanity checking
D_FLTRWDMIN =4.0d0
#
# Min filter width used by W_Smooth1
#   D_FLTRWDBEG1 is the two sigma filter used to make the alt smoothed WF
#   D_FLTRWDBEG2 is the two sigma filter used to make the std smoothed WF
#   both smoothed WFs are passed to W_FunctionalFt & used for estimates.
D_FLTRWDBEG1 =14.0d0
D_FLTRWDBEG2 =33.0d0
D_FLTRWDMAX = 129.0d0
#   max num bins to use for smoothing in W_Smooth1
I_MAXSMBINS = 129
#
# Absolute minimum amplitude (volts)
D_ABSMINAMP1 = 0.05d0
D_ABSMINAMP2 = 0.05d0
#
# Min peak amplitude = d_Npeak_min? * (sDevNoise)+ noise
D_NPEAK_MIN1 = 4.5d0
D_NPEAK_MIN2 = 4.5d0
#
# Max peak amplitude (volts)
D_MAXAMP = 2.5d0
```

```

#
# Min & max peak sigma (ns)
D_SIGMAMINIT = 2.5d0
D_MAXSIGMA = 300.0d0
#
# Max value for d_wfFitSDev and d_sDevFitTr
D_MAXSDEV = 0.3d0
#
# Noise threshold TransPulse = d_nsigTx * sDevNsTx
D_NSIGTX = 1.5d0
#
#
# D_T_NSIG      YYYYMMDD HHMMSS
# 000000000.0d0 20030220 000000 L1A
# 117782220.0d0 20030925 171700 L2A
# 130326180.0d0 20040217 214300 L2B
# 138171420.0d0 20040518 165700 L2C
# 150111000.0d0 20041003 213000 L3A
# 161928480.0d0 20050217 160800 L3B
# 169878900.0d0 20050520 163500 L3C
# 183207360.0d0 20051021 225600 L3D
# 193912620.0d0 20060222 203700 L3E
# 201764580.0d0 20060524 174300 L3F
# 215052540.0d0 20061025 124900 L3G
# 226937100.0d0 20070312 020500 L3H
# 244631400.0d0 20071002 211000 L3I
# 256549920.0d0 20080217 195200 L3J
# 276401580.0d0 20081004 141300 L3K
# 280907280.0d0 20081125 174800 L2D
# 289879560.0d0 20090309 140600 L2E
#
# Noise threshold = d_nsig? * sDevNoise
#
# NSIG Table Fields:
#
GI_NUM_NSIG = 8
#
# Table History
#
# 7/31/2009 Change Std fit Nsig to 9.5 for L2C 5/17/2004 to 6/22/2004
# 7/31/2009 Change std fit Nsig to 15 for L3A to L3G
# 7/31/2009 Change Std fit Nsig to 9.5 for L3G and all periods afterward
# 10/24/2006 table end
# 7/31/2009 Change Alt fit Nsig to 7.5 for L2E 3/8/2009 table end
# 2011-03-03 Changed entry#4 from time 280900000 to 244631000
#
#
#           TIME           B_NSIG1 E_NSIG1 B_NSIG2 E_NSIG2
#
D_NSIG_TABLE = 000000000.0d0  3.5D0  4.5D0  15.0D0  15.0D0
D_NSIG_TABLE = 138024000.0d0  3.5D0  4.5D0  15.0D0  15.0D0
D_NSIG_TABLE = 141134400.0d0  3.5D0  4.5D0  15.0D0  15.0D0
D_NSIG_TABLE = 244631000.0d0  3.5D0  4.5D0   9.5D0   9.5D0
D_NSIG_TABLE = 289742400.0d0  7.5D0  7.5D0   9.5D0   9.5D0
D_NSIG_TABLE = 999999999.0d0  7.5D0  7.5D0   9.5D0   9.5D0
D_NSIG_TABLE = 999999999.0d0  7.5D0  7.5D0   9.5D0   9.5D0
D_NSIG_TABLE = 999999999.0d0  7.5D0  7.5D0   9.5D0   9.5D0
#

```

```

# Min interval between peaks
D_INTV_MIN1 = 15.0d0
D_INTV_MIN2 = 30.0d0
#
# fraction of peak sigma proximity to sigB or sigE allowed during fit
D_DPROX1 = 0.0d0
D_DPROX2 = 0.25d0
#
# 1=don't remove peaks if too small, too narrow, or too close.
I_KEEPALLPKS1 = 1
I_KEEPALLPKS2 = 0
#
# 1=remove peaks if zero amplitude and if I_KEEPALLPKSn == 1
I_THROWOUTZA1 = 1
I_THROWOUTZA2 = 0
#
# d_maxDeltas = max delta during fit
#   _N multiply by noise parm
#   _A multiply by amplitude parm
#   _L absolute number for max loc delta in ns
#   _S multiply by sigma parm
D_MAXDELTAS_N1 = 0.0d0
D_MAXDELTAS_A1 = 0.5d0
D_MAXDELTAS_L1 = 15.0d0
D_MAXDELTAS_S1 = 0.5d0
#
D_MAXDELTAS_N2 = 0.0d0
D_MAXDELTAS_A2 = 0.5d0
D_MAXDELTAS_L2 = 15.0d0
D_MAXDELTAS_S2 = 0.5d0
#D_MAXDELTAS_A2 = 10000.0d0
#D_MAXDELTAS_L2 = 10000.0d0
#D_MAXDELTAS_S2 = 10000.0d0
#
# Switch used during estimates (for secondary peaks)
# 0=Recompute peak sigmas
# 1=Do not recompute sigmas
#The loop is going from the largest area to the smallest.
# If i_estswN=1, then it only does the highest ranking peak (largest area).
# If i_estswN=0, then it recomputes the sigma for all of the peaks.
#When the sigma is recomputed, instead of computing the sigma from the second
# derivative, the locations to either side of the peak location are found
# where the amplitude is a percentage of the peak amplitude:
# At T where W = 80% AMPm, |T-Tm| = 0.668045 * SGMm.
# so, find T1 before Tm and T2 after Tm where W = 80% AMPm
# SGMm = |dT2_80 - dT1_80| / 1.33609d0
# At T where W = 60.653% AMPm, |T-Tm| = SGMm.
# so, find T1 before Tm and T2 after Tm where W = 60.653% AMPm
# SGMm = |dT2_61 - dT1_61| / 2.0d0
I_ESTSW1 = 0
I_ESTSW2 = 1
#
# Combine peaks switch
# "(0,1) => weight peaks by area when combining"
# "(1,0) => use straight average when combining peaks"
D_CMB1 = 0.0d0
D_CMB2 = 1.0d0

```

```

#
# min signal width for a good fit
#   if sigE-sigB < this value, l_WFqual(gwi_suspect,iWF) is set
D_MINSIGWIDTH = 5.0d0
#
# min peak to noise ratio for a good fit
#   if (maxAmp-d_bgNoiseOb)/d_sDevNsOb < this value,
#     l_WFqual(gwi_suspect,iWF) is set
D_MINPK2NS = 5.0d0
#
# max value of standard deviation of fit for a good fit
#   if d_wfFitSDev(iWF,?) > this value, l_WFqual(gwi_poorFit?,iWF) is set
D_MAXGOODSDEV1 = 0.06d0
D_MAXGOODSDEV2 = 0.04d0
#
# chi threshold for convergence of fit in W_CkConvRMS
#   when sDevFit changes by <= this value during an iteration of the fit,
#     then the fit has converged
D_WFFITSDEVTHR1 = 0.001d0
D_WFFITSDEVTHR2 = 0.00001d0
#
# Switch to normalize WF during fit
# 0 => don't normalize
# 1 => normalize
I_NORMWF1 = 1
I_NORMWF2 = 0
#
# Switch to convergence method
# 0 => use W_CkConv      (parameter change)
# 1 => use W_CkConvRMS  (chi change)
I_CONVSW1 = 1
I_CONVSW2 = 0
#
# Iterated parameter change indicating convergence in W_CkConv
# 0.02 == 2% or less change => convergence
D_DNOISE1 = 0.02d0
D_DNOISE2 = 0.02d0
#
D_DAMPCK1 = 0.02d0
D_DAMPCK2 = 0.02d0
#
D_DTMCK1 = 0.02d0
D_DTMCK2 = 0.07d0
#
D_DSGMCK1 = 0.02d0
D_DSGMCK2 = 0.02d0
#
# Switches
# 1==use D_DTMCK as a number of ns
# 0==use D_DTMCK as percent for W_CkConv
#
I_TMCKSW1 = 0
I_TMCKSW2 = 1
#
# Calculate noise switch
# "0==use observed noise & sDevNoise, 1==calculate noise & sDevNoise"
I_NSCAL1 = 0

```

```

I_NSCAL2 = 0
#
# Number of gates to use to calculate noise (beginning & ending of WF)
INGATES2USE1 = 20
INGATES2USE2 = 20
#
# Min number of gates to use to calculate noise (in case signal_begin or
#   signal_end occurs within INGATES2USE? gates of the beginning or ending
#   of the WF)
IMINNG2USE = 10
#
# Number of gates to use to calculate noise for the transmitted pulse
INGATES2USETR = 10
#
# Min number of gates to use to calculate noise for the transmitted pulse
IMINNG2USETR = 5
#
# Min i_satNdx to be counted as saturated for QA purposes
IMINSATNDX = 2
#
# Threshold for saturation index.  If the gate amplitude is >=
#   this value, then i_satNdx is incremented (max value is 126).
# -- changed to array of 256 per mantis 2324
#I_SATNDXTH = 220
I_SAT_TH_1= 30, 30, 30, 30, 30, 30, 30, 30, 30,109,149,177,196,209,218,224,228
I_SAT_TH_2= 231,232,233,234,234,234,235,235,236,237,238,239,239,239,239,239
I_SAT_TH_3= 239,239,239,239,239,239,239,239,239,239,239,239,239,239,239
I_SAT_TH_4= 239,239,239,239,239,239,239,239,239,239,239,239,239,239,239
I_SAT_TH_5= 239,239,239,239,239,239,239,239,239,239,239,239,239,239,239
I_SAT_TH_6= 239,239,239,239,239,239,239,239,239,239,239,239,239,239,239
I_SAT_TH_7= 239,239,239,239,239,239,239,239,239,239,239,239,239,239,239
I_SAT_TH_8= 239,239,239,239,239,239,239,239,239,239,239,239,239,239,239
I_SAT_TH_9= 239,239,239,239,239,239,239,239,239,239,239,239,239,239,239
I_SAT_TH_10=239,239,239,239,239,239,239,239,239,239,239,239,239,239,239
I_SAT_TH_11=239,239,239,239,239,239,239,239,239,239,239,239,239,239,239
I_SAT_TH_12=239,239,239,239,239,239,239,239,239,239,239,239,239,239,239
I_SAT_TH_13=239,239,239,239,239,239,239,239,239,239,239,239,239,239,239
I_SAT_TH_14=239,239,239,239,239,239,239,239,239,239,239,239,239,239,239
I_SAT_TH_15=239,239,239,239,239,239,239,239,239,239,239,239,239,239,239
I_SAT_TH_16=239,239,239,239,239,239,239,239,239,239,239,239,239,239,239
#
# Used in W_Estimates and W_EstNew.  If I_SATNDX <= this value, then
#   Sigma is not recal'd as if the whole signal was one saturated peak
I_MAXNDXNSAT1 = 20
I_MAXNDXNSAT2 = 0
#
# Used in W_Estimates and W_EstNew.  If I_stopat6_1=1 then stop combining
#   peaks in spite of being close to other peaks if 6 or less
I_STOPAT6_1 = 0
I_STOPAT6_2 = 0
#
# Used in W_Estimates and W_EstNew.  If i_keepPk1_1=1 then keep peak #1
#   even if its rank is more than i_maxfit
I_KEEPPK1_1 = 1
I_KEEPPK1_2 = 0
#
# non-linear gain calibration for reflectivity

```

```

# Y=NLGC(1)+NLGC(2)*gain+NLGC(3)*gain^2+NLGC(4)*gain^3+NLGC(5)*gain^4
# f = 1 / Y
# E_norm = f * E
#
D_NLGC = 0.72807d0, 0.008543d0, -9.6905d-5, 4.7896d-7, -8.621d-10
#
# BSS (Boresight Shift Shadowing)
#
# D_T_BSS      YYYYMMDD HHMMSS      D_F_BSS
# 000000000.0d0 20030220 000000 L1A 1.00d0
# 117782220.0d0 20030925 171700 L2A 1.83d0
# 119340000.0d0 20031013 180000 L2A 1.95d0
# 119348940.0d0 20031013 202900 L2A 1.15d0
# 119443920.0d0 20031014 225200 L2A 1.30d0
# 120648000.0d0 20031028 212000 L2A 1.55d0
# 120735000.0d0 20031029 213000 L2A 1.35d0
# 130326180.0d0 20040217 214300 L2B 1.30d0
# 138171420.0d0 20040518 165700 L2C 1.40d0
# 138348060.0d0 20040520 180100 L2C 1.23d0
# 150111000.0d0 20041003 213000 L3A 1.00d0
# 161928480.0d0 20050217 160800 L3B 0.95d0
# 183207360.0d0 20051021 225600 L3D 1.00d0
# 256554496.0d0 20080217 000000 L3J 1.00d0
# 276405992.0d0 20081004 000000 L3K 1.00d0
# 280907280.0d0 20081125 174800 L2D 1.23d0 -> 1.7d0
# 289879560.0d0 20090309 140600 L2E 1.23d0 -> 1.7d0
# 307623923.0d0 20090930 000000 L2F 1.23d0 -> 1.7d0
# 999999999.0d0 ----- ----- --- 1.00d0
#
# number of actual values in table
I_N_BSS = 15
#
# effective time
D_T_BSS1 = 000000000.0d0, 117782220.0d0, 119340000.0d0, 119348940.0d0
D_T_BSS2 = 119443920.0d0, 120648000.0d0, 120735000.0d0, 130326180.0d0
D_T_BSS3 = 138171420.0d0, 138348060.0d0, 150111000.0d0, 161928480.0d0
D_T_BSS4 = 183207360.0d0, 280907280.0d0, 999999999.0d0, 999999999.0d0
D_T_BSS5 = 999999999.0d0, 999999999.0d0, 999999999.0d0, 999999999.0d0
D_T_BSS6 = 999999999.0d0, 999999999.0d0, 999999999.0d0, 999999999.0d0
#
# Calibration factor
D_F_BSS1 = 1.00d0, 1.83d0, 1.95d0, 1.15d0
D_F_BSS2 = 1.30d0, 1.55d0, 1.35d0, 1.30d0
D_F_BSS3 = 1.40d0, 1.23d0, 1.00d0, 0.95d0
D_F_BSS4 = 1.00d0, 1.70d0, 1.00d0, 1.00d0
D_F_BSS5 = 1.00d0, 1.00d0, 1.00d0, 1.00d0
D_F_BSS6 = 1.00d0, 1.00d0, 1.00d0, 1.00d0
#
# Overall calibration for reflectivity
# d_ovrCalib(2)==1/1.16
D_OVRCALIB = 0.0d0, 0.862068965d0
#
# retracker threshold = d_thresh_lvl * maxSmoothAmp(WF)
D_THRESH_LVL1 = 0.11d0
D_THRESH_LVL2 = 0.15d0
#
# Measurement uncertainty for computing weights for LsqFit

```

```

#   wt = 1/(D_WT_SGM)^2
D_WT_SGM1 = 0.03d0
D_WT_SGM2 = 0.001d0
#
# a priori fit-matrix-sigma for noise = 1/SQRT(d_V0ns)
D_VONS1 = 1000000.0d0
D_VONS2 = 1000000.0d0
#
# a priori fit-matrix-sigma for amplitude = 1/SQRT(d_V0amp)
D_VOAMP1 = 0.001d0
D_VOAMP2 = 0.001d0
#
# a priori fit-matrix-sigma for location = 1/SQRT(d_V0loc)
D_V0LOC1 = 0.1d0
D_V0LOC2 = 0.1d0
#
# a priori fit-matrix-sigma for peak-sigma = 1/SQRT(d_V0sgm)
D_V0SGM1 = 0.001d0
D_V0SGM2 = 0.001d0
#
# Minimum noise (raw counts)
D_MINNOISE = 0.5d0
#
# Area of telescope ... changed from 0.709 to pi/4
D_AREATELE = 0.78539816d0
#
# Optics transmission ... changed from .555 to .67 see mantis 671
D_OPTTRANS = 0.67d0
#
# QA along-track dumping interval time [seconds]
I_QA_DUMP_TME = 16
#
#   Set gain flag in i_ElvFlg = 1 if gain >= this value, = 0 otherwise
i_GainAlertLevel = 30
#
END_OF_WF = -----
#
END_OF_ANC07_FILE = -----

```

```

# anc07_001_01_0003.dat          Version 33
# Elevation Constants Mod Entries
#
BEG_OF_ELEV = -----
ELEV_VERS = ANC07 Elev Globals V6.0 2008-02-29
#
# gravity effect in milligals
#
gravEffTide = 9.8d0
#
# Constants used in calc of earth tide
#
earthTdH2 = 0.609d0
#
# Constants used in calc of earth tide
#
earthTdH3 = 0.291d0
#
# Beam Divergence Angle
#
#DIVANGLE = 0.00011d0
#
# QAP Track length (in secs)
#
QAPTRKLEN = 16.0d0
#
# Estimated Roundtrip Atmosphere Transmission
#
GD_T_RTATM = 0.98d0
#
# Filtering Ground Track Azimuth Parameters
GT_AZIMUTH_STDEV = 200.0D0
GT_AZIMUTH_NUM_VALS = 4
# min GLA05%i_satNdx to be counted as saturated
GI_MIN4SAT = 2
#
# percent saturation threshold for computing the saturation correction
GD_PCTSATTH = 2.0d0
# full width threshold for setting i_satCorrFlg
GD_FULLLWDTH = 100.0d0
#
END_OF_ELEV = -----
#
END_OF_ANC07_FILE = -----

```

APPENDIX 4.5, REL 33 WAVEFORM-BASED ELEVATION

i4b = four byte integer r4b = four byte real
 i2b = two byte integer r8b = eight byte real (double precision)
 i1b = one byte integer l4b = four byte logical

GLA05_prod_type			GLA05_alg_type		
i_rec_ndx	i4b	-	i_rec_ndx	i4b	-
i_UTCTime	i4b(2)	sec, μ sec	d_UTCTime	r8b	sec
i_transtime	i2b	μ sec	d_transtime	r8b	sec
i_spare1	i2b	-	-	-	-
i_deltagpstmcor	i4b	ns	d_deltagpstmcor	r8b	sec
i_dShotTime	i4b(39)	μ sec	d_dShotTime	r8b(39)	sec
i_lat	i4b(40)	μ deg	d_lat	r8b(40)	degN
i_lon	i4b(40)	μ deg	d_lon	r8b(40)	degE
i_elev	i4b(40)	mm	d_elev	r8b(40)	m
i_spare43	i4b(12,40)	-	-	-	-
i_sigmaatt	i2b(40)	unitless	i_sigmaatt	i2b(40)	unitless
i_gval_rcv	i2b(40)	counts	i_gval_rcv	i4b(40)	counts
i_wfnoiseOb1	i2b(40)	10^{-4} volts	d_wfnoiseOb1	r8b(40)	volts
i_wfnoiseOb2	i2b(40)	10^{-4} volts	d_wfnoiseOb2	r8b(40)	volts
i_sDevNsOb1	i2b(40)	10^{-4} volts	d_sDevNsOb1	r8b(40)	volts
i_sDevNsOb2	i2b(40)	10^{-4} volts	d_sDevNsOb2	r8b(40)	volts
i_refRngNs	i4b(40)	10^{-2} ns	d_refRngNs	r8b(40)	ns
i_thRtkRngOff1	i4b(40)	10^{-2} ns	d_thRtkRngOff1	r8b(40)	ns
i_thRtkRngOff2	i4b(40)	10^{-2} ns	d_thRtkRngOff2	r8b(40)	ns
i_minRngOff1	i4b(40)	10^{-2} ns	d_minRngOff1	r8b(40)	ns
i_minRngOff2	i4b(40)	10^{-2} ns	d_minRngOff2	r8b(40)	ns
i_preRngOff1	i4b(40)	10^{-2} ns	d_preRngOff1	r8b(40)	ns
i_preRngOff2	i4b(40)	10^{-2} ns	d_preRngOff2	r8b(40)	ns
i_centroid1	i4b(40)	10^{-2} ns	d_centroid1	r8b(40)	ns
i_centroid2	i4b(40)	10^{-2} ns	d_centroid2	r8b(40)	ns
i_centroidInstr	i4b(40)	10^{-2} ns	d_centroidInstr	r8b(40)	ns
i_areaRecWF1	i2b(40)	10^{-2} ns*volts	d_areaRecWF1	r8b(40)	ns*volts
i_areaRecWF2	i2b(40)	10^{-2} ns*volts	d_areaRecWF1	r8b(40)	ns*volts
i_maxRecAmp	i2b(40)	10^{-4} volts	d_maxRecAmp	r8b(40)	volts
i_maxSmAmp	i2b(40)	10^{-4} volts	d_maxSmAmp	r8b(40)	volts
i_reflctUncorr	i4b(40)	10^{-6} unitless	d_reflctUncorr	r8b(40)	unitless
i_reflctuncmxpk	i4b(40)	10^{-6} unitless	d_reflctuncmxpk	r8b(40)	unitless
i_tpCentX	i2b(40)	10^{-1} arcsec	d_tpCentX	r8b(40)	arcsec
i_tpCentY	i2b(40)	10^{-1} arcsec	d_tpCentY	r8b(40)	arcsec
i_nPeaks1	i1b(40)	-	i_nPeaks1	i4b(40)	-
i_nPeaks2	i1b(40)	-	i_nPeaks2	i4b(40)	-
i_parm1	i4b(19,40)	10^{-4} v, $6*(10^{-4}$ v,	d_parm1	r8b(19,40)	v, $6*($
i_parm2	i4b(19,40)	10^{-2} ns, 10^{-2} ns)	d_parm2	r8b(19,40)	v, ns,
i_solnSigmas1	i2b(19,40)	" "	d_solnSigmas1	r8b(19,40)	ns)
i_solnSigmas2	i2b(19,40)	" "	d_solnSigmas2	r8b(19,40)	" "
i_wfFitSDev_1	i2b(40)	10^{-5} unitless	d_wfFitSDev_1	r8b(40)	unitless
i_wfFitSDev_2	i2b(40)	10^{-5} v	d_wfFitSDev_2	r8b(40)	v
i_tpintensity	i4b(40)	counts	d_tpintensity	r8b(40)	counts
i_tpazimuth	i2b(40)	10^{-1} deg	d_tpazimuth	r8b(40)	deg
i_tpeccentricity	i2b(40)	10^{-3} e	d_tpeccentricity	r8b(40)	e
i_tpmajoraxis	i2b(40)	cm	d_tpmajoraxis	r8b(40)	m
i_skew1	i2b(40)	10^{-2} unitless	d_skew1	r8b(40)	unitless
i_kurt1	i2b(40)	10^{-2} unitless	d_kurt1	r8b(40)	unitless
i_skew2	i2b(40)	10^{-2} unitless	d_skew2	r8b(40)	unitless
i_kurt2	i2b(40)	10^{-2} unitless	d_kurt2	r8b(40)	unitless

i_WFqual	i4b(40)	-	l_WFqual	i4b(32,40)	-
i_TxNrg	i2b(40)	10^{-5} Joules	d_TxNrg	r8b(40)	J
i_tpOrX	i2b(40)	10^{-1} deg	d_tpOrX	r8b(40)	deg
i_locTr	i4b(40)	10^{-2} ns	d_locTr	r8b(40)	ns
i_parmTr	i4b(4,40)	10^{-4} v, 10^{-4} v, 10^{-2} ns, 10^{-2} ns	d_parmTr	r8b(4,40)	v,v, ns,ns
i_sDevFitTr	i2b(40)	10^{-5} v	d_sDevFitTr	r8b(40)	v
i_skewTr	i4b(40)	10^{-2} unitless	d_skewTr	r8b(40)	unitless
i_maxTrAmp	i2b(40)	10^{-4} v	d_maxTrAmp	r8b(40)	v
i_gval_tx	i2b	counts	i_gval_tx	i4b	counts
i_compRatio	i2b(2)	-	i_compRatio	i4b(2)	-
i_N_val	i2b	gates	i_N_val	i4b	gates
i_r_val	i2b	-	i_r_val	i4b	-
i_ElvuseFlg	i1b(5)	-	i_ElvuseFlg	i4b(40)	-
i_spare3	i1b(1)	-	-	-	-
i_elvflg	i1b(40)	-	i_elvflg	i4b(8,40)	-
i_spare49	i1b(10)	-	-	-	-
i_timecorflg	i2b	-	l_timecorflg	l4b(16)	-
i_APID_AvFlg	i1b(8)	-	i_APID_AvFlg	i4b(32)	-
i_AttFlg2	i1b(20)	-	i_padUseFlg	i4b(40)	-
			i_calcPadFlg	i4b(40)	-
			i_LPAProbFlg	i4b(40)	-
			i_TBD_Flg	i4b(40)	-
			-	-	-
i_spare4	i1b	-	i_altFrmFlg	i4b(4)	-
i_FrameQF	i1b	-	i_podFlg	i4b(6)	-
i_OrbFlg	i1b(2)	-	i_rngCorrFlg	i4b(7)	-
i_rngCorrFlg	i1b(2)	-	-	-	-
i_spare5	i1b(2)	-			
i_beam_coelev	i4b	10^{-2} deg	d_beam_coelev	r8b	deg
i_beam_azimuth	i4b	10^{-2} deg	d_beam_azimuth	r8b	deg
i_AttFlg1	i2b	-	i_AttFlg	i4b(8)	-
i_RMSpulseWd	i2b(40)	10^{-2} ns	d_RMSpulseWd	r8b(40)	ns
i_satNdx	i1b(40)	-	i_satNdx	i4b(40)	-
i_RecNrgAll	i2b(40)	10^{-2} fJ	d_RecNrgAll	r8b(40)	J
i_numIters	i1b(40)	-	i_numIters	i4b(40,2)	-
i_spare6	i1b(70)	-	-	-	-

APPENDIX 4.6, REL 33 ELEVATION

i4b = four byte integer c1 = one byte character
 i2b = two byte integer r8b = eight byte real (double precision)
 i1b = one byte integer l4b = four byte logical

GLA06_prod_type			GLA06_alg_type		
i_rec_ndx	i4b	-	i_rec_ndx	i4b	-
i_UTCTime	i4b(2)	sec,usec	d_UTCTime	r8b	sec
i_transtime	i2b	usec	d_transtime	r8b	sec
i_spare1	i2b	-	-	-	-
i_deltagpstmcor	i4b	ns	d_deltagpstmcor	r8b	sec
i_dShotTime	i4b(39)	usec	d_dShotTime	r8b(39)	sec
i_lat	i4b(40)	udeg	d_lat	r8b(40)	degN
i_lon	i4b(40)	udeg	d_lon	r8b(40)	degE
i_elev	i4b(40)	mm	d_elev	r8b(40)	m
i_campaign	i1b(2)	-	c_campaign	c1(2)	-
i_spare40	i2b	-	-	-	-
i_cycTrk	i4b	-	i_cycle	i4b	-
			i_track	i4b	-
i_localSolarTime	i4b	10 ⁻³ sec	d_localSolarTime	r8b	sec
i_spare41	i4b(7)	-	-	-	-
i_deltaEllip	i2b(40)	mm	d_deltaEllip	r8b(40)	m
i_beamCoelv	i4b(40)	10 ⁻³ deg	d_beamCoelv	r8b(40)	deg
i_beamAzimuth	i4b(40)	10 ⁻³ deg	d_beamAzimuth	r8b(40)	deg
i_d2refTrk	i4b(40)	mm	d_d2refTrk	r8b(40)	m
i_SigBegOff	i4b(40)	mm	d_SigBegOff	r8b(40)	m
i_DEM_hires_src	i1b(40)	-	i_DEM_hires_src	i1b(40)	-
i_DEMhiresArElv	i2b(9,40)	m	d_DEMhiresArElv	r8b(3,3,40)	m
i_ElevBiasCorr	i2b(40)	mm	d_ElevBiasCorr	r8b(40)	m
i_spare42	i2b(4,40)	-	-	-	-
i_sigmaatt	i2b(40)	unitless	i_sigmaatt	i2b(40)	-
i_Azimuth	i4b	10 ⁻³ deg	d_Azimuth	r8b	deg
i_SolAng	i4b	udeg	d_SolAng	r8b	deg
i_tpintensity_avg	i4b	count	d_tpintensity_avg	r8b	count
i_tpazimuth_avg	i2b	10 ⁻¹ deg	d_tpazimuth_avg	r8b	deg
i_tpeccentricity_avg	i2b	10 ⁻³ unitless	d_tpeccentricity_avg	r8b	-
i_tpmajoraxis_avg	i2b	10 ⁻² m	d_tpmajoraxis_avg	r8b	m
i_poTide	i2b	10 ⁻³ m	d_poTide	r8b	m
i_gdHt	i2b(2)	10 ⁻² m	d_gdHt	r8b(2)	m
i_erElv	i2b(2)	10 ⁻³ m	d_erElv	r8b(2)	m
i_spElv	i2b(4)	10 ⁻³ m	d_spElv	r8b(4)	m
i_ldElv	i2b(4)	10 ⁻³ m	d_ldElv	r8b(4)	m
i_spare12	i2b(2)	-	-	-	-
i_wTrop	i2b(2)	10 ⁻³ m	d_wTrop	r8b(2)	m
i_dTrop	i2b(40)	10 ⁻³ m	d_dTrop	r8b(40)	m
i_surfType	i1b	-	l_surfType	l4b(4)	-
i_spare11	i1b(3)	-	-	-	-
i_DEM_elv	i4b(40)	10 ⁻² m	d_DEM_elv	r8b(40)	m
i_refRng	i4b(40)	10 ⁻³ m	d_refRng	r8b(40)	m
i_TrshRngOff	i4b(40)	10 ⁻³ m	d_TrshRngOff	r8b(40)	m
i_spare47	i4b(40)	-	-	-	-
i_SigEndOff	i4b(40)	10 ⁻³ m	d_SigEndOff	r8b(40)	m
i_cntRngOff	i4b(40)	10 ⁻³ m	d_cntRngOff	r8b(40)	m
i_reflctUC	i4b(40)	10 ⁻⁶ unitless	d_reflctUC	r8b(40)	-
i_reflCor_atm	i4b	10 ⁻⁶ unitless	d_reflCor_atm	r8b	-
i_maxSmAmp	i2b(40)	10 ⁻⁴ v	d_maxSmAmp	r8b(40)	v

i_ocElv	i2b(40)	10 ⁻³ m	d_ocElv	r8b(40)	m
i_numPk	i1b(40)	-	i_numPk	i4b(40)	-
i_kurt2	i2b(40)	10 ⁻² unitless	d_kurt2	r8b(40)	-
i_skew2	i2b(40)	10 ⁻² unitless	d_skew2	r8b(40)	-
i_spare4	i1b(160)	-	-	-	-
i_isRngOff	i4b(40)	10 ⁻³ m	d_isRngOff	r8b(40)	m
i_siRngOff	i4b(40)	10 ⁻³ m	d_siRngOff	r8b(40)	m
i_ldRngOff	i4b(40)	10 ⁻³ m	d_ldRngOff	r8b(40)	m
i_ocRngOff	i4b(40)	10 ⁻³ m	d_ocRngOff	r8b(40)	m
i_nPeaks1	i1b(40)	-	i_nPeaks1	i4b(40)	-
i_ElvuseFlg	i1b(5)	-	i_ElvuseFlg	i4b(40)	-
i_atm_avail	i1b	-	i_atm_avail	i4b	-
i_spare16	i2b(4)	-	-	-	-
i_cld1_mswf	i1b	-	i_cld1_mswf	i4b	-
i_MRC_af	i1b	-	i_MRC_af	i4b	-
i_spare9	i1b(40)	-	-	-	-
i_elvflg	i1b(40)	-	i_elvflg	i4b(8,40)	-
i_rng_UQF	i2b(40)	-	i_RngOffQF	i4b(16,40)	-
i_spare49	i1b(10)	-	-	-	-
i_timecorflg	i2b	-	l_timecorflg	l4b(16)	-
i_APID_AvFlg	i1b(8)	-	i_APID_AvFlg	i4b(32)	-
i_AttFlg2	i1b(20)	-	i_padUseFlg	i4b(40)	-
			i_calcPadFlg	i4b(40)	-
			i_LPAProbFlg	i4b(40)	-
i_spare5	i1b	-	-	-	-
i_FrameQF	i1b	-	i_altFrmFlg	i4b(4)	-
i_OrbFlg	i1b(2)	-	i_podFlg	i4b(6)	-
i_rngCorrFlg	i1b(2)	-	i_rngCorrFlg	i4b(7)	-
i_CorrStatFlg	i1b(2)	-	i_corrStatFlg	i4b(3)	-
i_spare15	i1b(8)	-	-	-	-
i_AttFlg1	i2b	-	i_AttFlg	i4b(8)	-
i_spare6	i1b(2)	-	-	-	-
i_spare44	i1b(120)	-	-	-	-
i_satNdx	i1b(40)	ns	i_satNdx	i4b(40)	ns
i_satElevCorr	i2b(40)	10 ⁻³ m	d_satElevCorr	r8b(40)	m
i_satCorrFlg	i1b(40)	-	i_satCorrFlg	i4b(40)	-
i_satNrgCorr	i2b(40)	10 ⁻¹⁷ J	d_satNrgCorr	r8b(40)	J
i_spare13	i2b(40)	-	-	-	-
i_gval_rcv	i2b(40)	counts	i_gval_rcv	i4b(40)	cnts
i_RecNrgAll	i2b(40)	10 ⁻¹⁷ J	d_RecNrgAll	r8b(40)	J
i_FRir_cldtop	i2b(40)	10m	d_FRir_cldtop	r8b(40)	m
i_FRir_qaFlag	i1b(40)	-	i_FRir_qaFlag	i4b(40)	-
i_atm_char_flag	i2b	-	i_atm_char_flag	i2b	-
i_atm_char_conf	i2b	-	i_atm_char_conf	i2b	-
i_spare48	i1b(36)	-	-	-	-
i_FRir_intsig	i2b(40)	10 ⁻⁷ /(m-sr)	d_FRir_intsig	r8b(40)	1/(m-sr)
i_spare14	i1b(120)	-	-	-	-
i_Surface_temp	i2b	10 ⁻² degC	d_Surface_temp	r8b	degC
i_Surface_pres	i2b	10 ⁻¹ hPa	d_Surface_pres	r8b	hPa
i_Surface_relh	i2b	10 ⁻² %	d_Surface_relh	r8b	%
i_pctSAT	i1b(40)	%	d_pctSAT	r8b(40)	%
i_maxRecAmp	i2b(40)	10 ⁻⁴ v	d_maxRecAmp	r8b(40)	v
i_sDevNsOb1	i2b(40)	10 ⁻⁴ v	d_sDevNsOb1	r8b(40)	v
i_TxNrg	i2b(40)	10 ⁻⁵ J	d_TxNrg	r8b(40)	J
i_eqElv	i2b(2)	10 ⁻³ m	d_eqElv	r8b(2)	m
i_spare7	i1b(282)	-	-	-	-

APPENDIX 4.12, REL 33 ICE SHEET ELEVATION

i4b = four byte integer c1 = one byte character
 i2b = two byte integer r8b = eight byte real (double precision)
 i1b = one byte integer l4b = four byte logical

GLA12_prod_type			GLA12_alg_type		
i_rec_ndx	i4b	-	i_rec_ndx	i4b	-
i_UTCTime	i4b(2)	sec,µsec	d_UTCTime	r8b	sec
i_transtime	i2b	µsec	d_transtime	r8b	sec
i_spare1	i2b	-	-	-	-
i_deltagpstmcor	i4b	ns	d_deltagpstmcor	r8b	sec
i_dShotTime	i4b(39)	µsec	d_dShotTime	r8b(39)	sec
i_lat	i4b(40)	µdeg	d_lat	r8b(40)	degN
i_lon	i4b(40)	µdeg	d_lon	r8b(40)	degE
i_elev	i4b(40)	10 ⁻³ m	d_elev	r8b(40)	m
i_campaign	i1b(2)	-	c_campaign	c1(2)	-
i_spare40	i2b	-	-	-	-
i_cycTrk	i4b	-	i_cycle	i4b	-
			i_track	i4b	-
i_localSolarTime	i4b	10 ⁻³ sec	d_localSolarTime	r8b	sec
i_spare41	i4b(7)	-	-	-	-
i_deltaEllip	i2b(40)	10 ⁻³ m	d_deltaEllip	r8b(40)	m
i_beamCoelv	i4b(40)	10 ⁻³ deg	d_beamCoelv	r8b(40)	deg
i_beamAzimuth	i4b(40)	10 ⁻³ deg	d_beamAzimuth	r8b(40)	deg
i_d2refTrk	i4b(40)	10 ⁻³ m	d_d2refTrk	r8b(40)	m
i_SigBegOff	i4b(40)	10 ⁻³ m	d_SigBegOff	r8b(40)	m
i_DEM_hires_src	i1b(40)	-	i_DEM_hires_src	i1b(40)	-
i_DEMhiresArElv	i2b(9,40)	m	d_DEMhiresArElv	r8b(3,3,40)	m
i_ElevBiasCorr	i2b(40)	10 ⁻³ m	d_ElevBiasCorr	r8b(40)	m
i_spare42	i2b(4,40)	-	-	-	-
i_sigmaatt	i2b(40)	-	i_sigmaatt	i2b(40)	-
i_Azimuth	i4b	10 ⁻³ deg	d_Azimuth	r8b	deg
i_SolAng	i4b	10 ⁻⁶ deg	d_SolAng	r8b	deg
i_tpintensity_avg	i4b	counts	d_tpintensity_avg	r8b	cnt
i_tpazimuth_avg	i2b	10 ⁻¹ deg	d_tpazimuth_avg	r8b	deg
i_tpeccentricity_avg	i2b	10 ⁻³ unitless	d_tpeccentricity_avg	r8b	-
i_tpmajoraxis_avg	i2b	10 ⁻² m	d_tpmajoraxis_avg	r8b	m
i_poTide	i2b	10 ⁻³ m	d_poTide	r8b	m
i_gdHt	i2b(2)	10 ⁻² m	d_gdHt	r8b(2)	m
i_erElv	i2b(2)	10 ⁻³ m	d_erElv	r8b(2)	m
i_spElv	i2b(4)	10 ⁻³ m	d_spElv	r8b(4)	m
i_ldElv	i2b(4)	10 ⁻³ m	d_ldElv	r8b(4)	m
i_spare12	i2b(2)	-	-	-	-
i_wTrop	i2b(2)	10 ⁻³ m	d_wTrop	r8b(2)	m
i_dTrop	i2b(40)	10 ⁻³ m	d_dTrop	r8b(40)	m
i_surfType	i1b	-	l_surfType	l4b(4)	-
i_spare11	i1b(3)	-	-	-	-
i_DEM_elv	i4b(40)	10 ⁻² m	d_DEM_elv	r8b(40)	m
i_refRng	i4b(40)	10 ⁻³ m	d_refRng	r8b(40)	m
i_TrshRngOff	i4b(40)	10 ⁻³ m	d_TrshRngOff	r8b(40)	m
i_isRngOff	i4b(40)	10 ⁻³ m	d_isRngOff	r8b	m
i_SigEndOff	i4b(40)	10 ⁻³ m	d_SigEndOff	r8b(40)	m
i_cntRngOff	i4b(40)	10 ⁻³ m	d_cntRngOff	r8b(40)	m
i_reflctUC	i4b(40)	10 ⁻⁶ unitless	d_reflctUC	r8b(40)	-
i_reflCor_atm	i4b	10 ⁻⁶ unitless	d_reflCor_atm	r8b	-
i_maxSmAmp	i2b(40)	10 ⁻⁴ v	d_maxSmAmp	r8b(40)	v

i_ocElv	i2b(40)	10 ⁻³ m	d_ocElv	r8b(40)	m
i_numPk	i1b(40)	-	i_numPk	i4b(40)	-
i_kurt2	i2b(40)	10 ⁻² unitless	d_kurt2	r8b(40)	-
i_skew2	i2b(40)	10 ⁻² unitless	d_skew2	r8b(40)	-
i_spare4	i1b(160)	-	-	-	-
i_IsRngLast	i4b(40)	10 ⁻³ m	d_IsRngLast	r8b(40)	m
i_IsRngFst	i4b(40)	10 ⁻³ m	d_IsRngFst	r8b(40)	m
i_IceSVar	i2b(40)	10 ⁻⁵ v	d_IceSVar	r8b(40)	v
i_ElvuseFlg	i1b(5)	-	i_ElvuseFlg	i4b(40)	-
i_atm_avail	i1b	-	i_atm_avail	i4b	-
i_spare16	i1b(4)	-	-	-	-
i_cld1_mswf	i1b	-	i_cld1_mswf	i4b	-
i_MRC_af	i1b	-	i_MRC_af	i4b	-
i_spare9	i1b(40)	-	-	-	-
i_elvflg	i1b(40)	-	i_elvflg	i4b(8,40)	-
i_rng_UQF	i2b(40)	-	i_rngOffQF	i4b(16,40)	-
i_spare49	i1b(10)	-	-	-	-
i_timecorflg	i2b	-	i_timecorflg	i4b(16)	-
i_APID_AvFlg	i1b(8)	-	i_APID_AvFlg	i4b(32)	-
i_AttFlg2	i1b(20)	-	i_padUseFlg	i4b(40)	-
			i_calcPadFlg	i4b(40)	-
			i_LPaproflg	i4b(40)	-
i_spare5	i1b	-	-	-	-
i_FrameQF	i1b	-	i_altFrmFlg	i4b(4)	-
i_OrbFlg	i1b(2)	-	i_podFlg	i4b(6)	-
i_rngCorrFlg	i1b(2)	-	i_rngCorrFlg	i4b(7)	-
i_CorrStatFlg	i1b(2)	-	i_CorrStatFlg	i4b(3)	-
i_spare15	i1b(8)	-	-	-	-
i_AttFlg1	i2b	-	i_AttFlg	i4b(8)	-
i_spare6	i1b(2)	-	-	-	-
i_spare44	i1b(120)	-	-	-	-
i_satNdx	i1b(40)	ns	i_satNdx	i4b(40)	ns
i_satElevCorr	i2b(40)	10 ⁻³ m	d_satElevCorr	r8b(40)	m
i_satCorrFlg	i1b(40)	-	i_satCorrFlg	i4b(40)	-
i_satNrgCorr	i2b(40)	10 ⁻¹⁷ J	d_satNrgCorr	r8b(40)	J
i_spare13	i2b(40)	-	-	-	-
i_gval_rcv	i2b(40)	counts	i_gval_rcv	i4b(40)	cnts
i_RecNrgAll	i2b(40)	10 ⁻¹⁷ J	d_RecNrgAll	r8b(40)	J
i_FRir_cldtop	i2b(40)	10m	d_FRir_cldtop	r8b(40)	m
i_FRir_qaFlag	i1b(40)	-	i_FRir_qaFlag	i4b(40)	-
i_atm_char_flag	i2b	-	i_atm_char_flag	i2b	-
i_atm_char_conf	i2b	-	i_atm_char_conf	i1b	-
i_spare48	i1b(36)	-	-	-	-
i_FRir_intsig	i2b(40)	10 ⁻⁷ /(m-sr)	d_FRir_intsig	r8b(40)	1/(m-sr)
i_spare14	i1b(120)	-	-	-	-
i_Surface_temp	i2b	10 ⁻² degC	d_Surface_temp	r8b	degC
i_Surface_pres	i2b	10 ⁻¹ hPa	d_Surface_pres	r8b	hPa
i_Surface_relh	i2b	10 ⁻² %	d_Surface_relh	r8b	%
i_maxRecAmp	i2b(40)	10 ⁻⁴ v	d_maxRecAmp	r8b(40)	v
i_sDevNsOb1	i2b(40)	10 ⁻⁴ v	d_sDevNsOb1	r8b(40)	v
i_pctSAT	i1b(40)	%	d_pctSAT	r8b(40)	%
i_TxNrg	i2b(40)	10 ⁻⁵ J	d_TxNrg	r8b(40)	J
i_eqElv	i2b(2)	10 ⁻³ m	d_eqElv	i2b(2)	m
i_spare7	i1b(282)	-	-	-	-

APPENDIX 4.13, REL 33 SEA ICE ROUGHNESS

i4b = four byte integer c1 = one byte character
 i2b = two byte integer r8b = eight byte real (double precision)
 i1b = one byte integer l4b = four byte logical

GLA13_prod_type			GLA13_alg_type		
i_rec_ndx	i4b	-	i_rec_ndx	i4b	-
i_UTCTime	i4b(2)	sec, μ sec	d_UTCTime	r8b	sec
i_transtime	i2b	μ sec	d_transtime	r8b	sec
i_spare1	i2b	-	-	-	-
i_deltagpstmcor	i4b	ns	d_deltagpstmcor	r8b	sec
i_dShotTime	i4b(39)	μ sec	d_dShotTime	r8b(39)	sec
i_lat	i4b(40)	μ deg	d_lat	r8b(40)	degN
i_lon	i4b(40)	μ deg	d_lon	r8b(40)	degE
i_elev	i4b(40)	mm	d_elev	r8b(40)	m
i_campaign	i1b(2)	-	c_campaign	c1(2)	-
i_spare40	i2b	-	-	-	-
i_cycTrk	i4b	-	i_cycle	i4b	-
			i_track	i4b	-
i_localSolarTime	i4b	10^{-3} sec	d_localSolarTime	r8b	sec
i_spare41	i4b(7)	-	-	-	-
i_deltaEllip	i2b(40)	10^{-3} m	d_deltaEllip	r8b(40)	m
i_beamCoelv	i4b(40)	10^{-3} deg	d_beamCoelv	r8b(40)	deg
i_beamAzimuth	i4b(40)	10^{-3} deg	d_beamAzimuth	r8b(40)	deg
i_d2refTrk	i4b(40)	10^{-3} m	d_d2refTrk	r8b(40)	m
i_SigBegOff	i4b(40)	10^{-3} m	d_SigBegOff	r8b(40)	m
i_DEM_hires_src	i1b(40)	-	i_DEM_hires_src	i1b(40)	-
i_DEMhiresArElv	i2b(9,40)	m	d_DEMhiresArElv	r8b(3,3,40)	m
i_ElevBiasCorr	i2b(40)	10^{-3} m	d_ElevBiasCorr	r8b(40)	m
i_spare42	i2b(4,40)	-	-	-	-
i_sigmaatt	i2b(40)	-	i_sigmaatt	i2b(40)	-
i_Azimuth	i4b	10^{-3} deg	d_Azimuth	r8b	deg
i_SolAng	i4b	10^{-6} deg	d_SolAng	r8b	deg
i_tpintensity_avg	i4b	counts	d_tpintensity_avg	r8b	cnt
i_tpazimuth_avg	i2b	10^{-1} deg	d_tpazimuth_avg	r8b	deg
i_tpeccentricity_avg	i2b	10^{-3} unitless	d_tpeccentricity_avg	r8b	-
i_tpmajoraxis_avg	i2b	10^{-2} m	d_tpmajoraxis_avg	r8b	m
i_poTide	i2b	10^{-3} m	d_poTide	r8b	m
i_gdHt	i2b(2)	10^{-2} m	d_gdHt	r8b(2)	m
i_erElv	i2b(2)	10^{-3} m	d_erElv	r8b(2)	m
i_spElv	i2b(4)	10^{-3} m	d_spElv	r8b(4)	m
i_ldElv	i2b(4)	10^{-3} m	d_ldElv	r8b(4)	m
i_spare12	i2b(2)	-	-	-	-
i_wTrop	i2b(2)	10^{-3} m	d_wTrop	r8b(2)	m
i_dTrop	i2b(40)	10^{-3} m	d_dTrop	r8b(40)	m
i_surfType	i1b	-	l_surfType	l4b(4)	-
i_spare11	i1b(3)	-	-	-	-
i_DEM_elv	i4b(40)	10^{-2} m	d_DEM_elv	r8b(40)	m
i_refRng	i4b(40)	10^{-3} m	d_refRng	r8b(40)	m
i_TrshRngOff	i4b(40)	10^{-3} m	d_TrshRngOff	r8b(40)	m
i_siRngOff	i4b(40)	10^{-3} m	d_siRngOff	r8b(40)	m
i_SigEndOff	i4b(40)	10^{-3} m	d_SigEndOff	r8b(40)	m
i_cntRngOff	i4b(40)	10^{-3} m	d_cntRngOff	r8b(40)	m
i_reflctUC	i4b(40)	10^{-6} unitless	d_reflctUC	r8b(40)	-
i_reflCor_atm	i4b	10^{-6} unitless	d_reflCor_atm	r8b	-
i_maxSmAmp	i2b(40)	10^{-4} v	d_maxSmAmp	r8b(40)	v

i_ocElv	i2b(40)	10 ⁻³ m	d_ocElv	r8b(40)	m
i_numPk	i1b(40)	-	i_numPk	i4b(40)	-
i_kurt2	i2b(40)	10 ⁻² unitless	d_kurt2	r8b(40)	-
i_skew2	i2b(40)	10 ⁻² unitless	d_skew2	r8b(40)	-
i_spare4	i1b(160)	-	-	-	-
i_BergElev	i4b(40)	10 ⁻³ m	d_BergElev	r8b(40)	m
i_spare10	i1b(160)	-	-	-	-
i_SiRngFst	i4b(40)	10 ⁻³ m	d_SiRngFst	r8b(40)	m
i_SeaIceVar	i2b(40)	10 ⁻³ v	d_SeaIceVar	r8b(40)	v
i_ElvuseFlg	i1b(5)	-	i_ElvuseFlg	i4b(40)	-
i_atm_avail	i1b	-	i_atm_avail	i4b	-
i_spare16	i1b(4)	-	-	-	-
i_cld1_mswf	i1b	-	i_cld1_mswf	i4b	-
i_MRC_af	i1b	-	i_MRC_af	i4b	-
i_spare9	i1b(40)	-	-	-	-
i_elvflg	i1b(40)	-	i_elvflg	i4b(8,40)	-
i_rng_UQF	i2b(40)	-	i_rngOffQF	i4b(16,40)	-
i_spare49	i1b(10)	-	-	-	-
i_timecorflg	i2b	-	i_timecorflg	i4b(16)	-
i_APID_AvFlg	i1b(8)	-	i_APID_AvFlg	i4b(32)	-
i_AttFlg2	i1b(20)	-	i_padUseFlg	i4b(40)	-
			i_calcPadFlg	i4b(40)	-
			i_LPaproflg	i4b(40)	-
i_spare5	i1b	-	-	-	-
i_FrameQF	i1b	-	i_altFrmFlg	i4b(4)	-
i_OrbFlg	i1b(2)	-	i_podFlg	i4b(6)	-
i_rngCorrFlg	i1b(2)	-	i_rngCorrFlg	i4b(7)	-
i_CorrStatFlg	i1b(2)	-	i_CorrStatFlg	i4b(3)	-
i_spare15	i1b(8)	-	-	-	-
i_AttFlg1	i2b	-	i_AttFlg	i4b(8)	-
i_spare6	i1b(2)	-	-	-	-
i_spare44	i1b(120)	-	-	-	-
i_satNdx	i1b(40)	ns	i_satNdx	i4b(40)	ns
i_satElevCorr	i2b(40)	10 ⁻³ m	d_satElevCorr	r8b(40)	m
i_satCorrFlg	i1b(40)	-	i_satCorrFlg	i4b(40)	-
i_satNrgCorr	i2b(40)	10 ⁻¹⁷ J	d_satNrgCorr	r8b(40)	J
i_spare13	i2b(40)	-	-	-	-
i_gval_rcv	i2b(40)	counts	i_gval_rcv	i4b(40)	cnt
i_RecNrgAll	i2b(40)	10 ⁻¹⁷ J	d_RecNrgAll	r8b(40)	J
i_FRir_cldtop	i2b(40)	10m	d_FRir_cldtop	r8b(40)	m
i_FRir_qaFlag	i1b(40)	-	i_FRir_qaFlag	i4b(40)	-
i_atm_char_flag	i2b	-	i_atm_char_flag	i2b	-
i_atm_char_conf	i2b	-	i_atm_char_conf	i2b	-
i_spare48	i1b(36)	-	-	-	-
i_FRir_intsig	i2b(40)	10 ⁻⁷ /(m-sr)	d_FRir_intsig	r8b(40)	1/(m-sr)
i_spare14	i1b(120)	-	-	-	-
i_Surface_temp	i2b	10 ⁻² degC	d_Surface_temp	r8b	degC
i_Surface_pres	i2b	10 ⁻¹ hPa	d_Surface_pres	r8b	hPa
i_Surface_relh	i2b	10 ⁻² %	d_Surface_relh	r8b	%
i_maxRecAmp	i2b(40)	10 ⁻⁴ v	d_maxRecAmp	r8b(40)	v
i_sDevNsOb1	i2b(40)	10 ⁻⁴ v	d_sDevNsOb1	r8b(40)	v
i_pctSAT	i1b(40)	%	d_pctSAT	r8b(40)	%
i_TxNrg	i2b(40)	10 ⁻⁵ J	d_TxNrg	r8b(40)	J
i_eqElv	i2b(2)	10 ⁻³ m	d_eqElv	r8b(2)	m
i_spare7	i1b(282)	-	-	-	-

APPENDIX 4.14, REL 33 LAND/CANOPY ELEVATION

i4b = four byte integer c1 = one byte character
 i2b = two byte integer r8b = eight byte real (double precision)
 i1b = one byte integer l4b = four byte logical

GLA14_prod_type			GLA14_alg_type		
i_rec_ndx	i4b	-	i_rec_ndx	i4b	-
i_UTCTime	i4b(2)	sec, μ sec	d_UTCTime	r8b	sec
i_transtime	i2b	μ sec	d_transtime	r8b	sec
i_spare1	i2b	-	-	-	-
i_deltagpstmcor	i4b	ns	d_deltagpstmcor	r8b	sec
i_dShotTime	i4b(39)	μ sec	d_dShotTime	r8b(39)	sec
i_lat	i4b(40)	μ deg	d_lat	r8b(40)	degN
i_lon	i4b(40)	μ deg	d_lon	r8b(40)	degE
i_elev	i4b(40)	mm	d_elev	r8b(40)	m
i_campaign	i1b(2)	-	c_campaign	c1(2)	-
i_spare40	i2b	-	-	-	-
i_cycTrk	i4b	-	i_cycle	i4b	-
			i_track	i4b	-
i_localSolarTime	i4b	10^{-3} sec	d_localSolarTime	r8b	sec
i_spare41	i4b(7)	-	-	-	-
i_deltaEllip	i2b(40)	10^{-3} m	d_deltaEllip	r8b(40)	m
i_beamCoelv	i4b(40)	10^{-3} deg	d_beamCoelv	r8b(40)	deg
i_beamAzimuth	i4b(40)	10^{-3} deg	d_beamAzimuth	r8b(40)	deg
i_d2refTrk	i4b(40)	10^{-3} m	d_d2refTrk	r8b(40)	m
i_SigBegOff	i4b(40)	10^{-3} m	d_SigBegOff	r8b(40)	m
i_DEM_hires_src	i1b(40)	-	i_DEM_hires_src	i1b(40)	-
i_DEMhiresArElv	i2b(9,40)	m	d_DEMhiresArElv	r8b(3,3,40)	m
i_ElevBiasCorr	i2b(40)	10^{-3} m	d_ElevBiasCorr	r8b(40)	m
i_spare42	i2b(4,40)	-	-	-	-
i_sigmaatt	i2b(40)	-	i_sigmaatt	i2b(40)	-
i_Azimuth	i4b	10^{-3} deg	d_Azimuth	r8b	deg
i_SolAng	i4b	10^{-6} deg	d_SolAng	r8b	deg
i_tpintensity_avg	i4b	counts	d_tpintensity_avg	r8b	cnt
i_tpazimuth_avg	i2b	10^{-1} deg	d_tpazimuth_avg	r8b	deg
i_tpeccentricity_avg	i2b	10^{-3} unitless	d_tpeccentricity_avg	r8b	-
i_tpmajoraxis_avg	i2b	10^{-2} m	d_tpmajoraxis_avg	r8b	m
i_poTide	i2b	10^{-3} m	d_poTide	r8b	m
i_gdHt	i2b(2)	10^{-2} m	d_gdHt	r8b(2)	m
i_erElv	i2b(2)	10^{-3} m	d_erElv	r8b(2)	m
i_spElv	i2b(4)	10^{-3} m	d_spElv	r8b(4)	m
i_ldElv	i2b(4)	10^{-3} m	d_ldElv	r8b(4)	m
i_spare12	i2b(2)	-	-	-	-
i_wTrop	i2b(2)	10^{-3} m	d_wTrop	r8b(2)	m
i_dTrop	i2b(40)	10^{-3} m	d_dTrop	r8b(40)	m
i_surfType	i1b	-	l_surfType	l4b(4)	-
i_spare11	i1b(3)	-	-	-	-
i_DEM_elv	i4b(40)	10^{-2} m	d_DEM_elv	r8b(40)	m
i_refRng	i4b(40)	10^{-3} m	d_refRng	r8b(40)	m
i_spare47	i4b(40)	-	-	-	-
i_ldRngOff	i4b(40)	10^{-3} m	d_ldRngOff	r8b(40)	m
i_SigEndOff	i4b(40)	10^{-3} m	d_SigEndOff	r8b(40)	m
i_gpCntRngOff	i4b(6,40)	10^{-3} m	d_gpCntRngOff	r8b(6,40)	m
i_reflctUC	i4b(40)	10^{-6} unitless	d_reflctUC	r8b(40)	-
i_reflCor_atm	i4b	10^{-6} unitless	d_reflCor_atm	r8b	-

i_maxSmAmp	i2b(40)	10 ⁻⁴ v	d_maxSmAmp	r8b(40)	v
i_ocElv	i2b(40)	10 ⁻³ m	d_ocElv	r8b(40)	m
i_numPk	i1b(40)	-	i_numPk	(40)	-
i_kurt1	i2b(40)	10 ⁻² unitless	d_kurt1	r8b(40)	-
i_skew1	i2b(40)	10 ⁻² unitless	d_skew1	r8b(40)	-
i_spare4	i1b(160)	-	-	-	-
i_Gamp	i4b(6,40)	10 ⁻² v	d_Gamp	r8b(6,40)	v
i_Garea	i4b(6,40)	10 ⁻² v*ns	d_Garea	r8b(6,40)	v*ns
i_Gsigma	i4b(6,40)	10 ⁻³ ns	d_Gsigma	r8b(6,40)	ns
i_nPeaks1	i1b(40)	-	i_nPeaks1	i4b(40)	-
i_LandVar	i2b(40)	10 ⁻⁵ unitless	d_LandVar	r8b(40)	-
i_ElvuseFlg	i1b(5)	-	i_ElvuseFlg	i4b(40)	-
i_atm_avail	i1b	-	i_atm_avail	i4b	-
i_spare16	i1b(4)	-	-	-	-
i_cld1_mswf	i1b	-	i_cld1_mswf	i4b	-
i_MRC_af	i1b	-	i_MRC_af	i4b	-
i_spare9	i1b(40)	-	-	-	-
i_elvflg	i1b(40)	-	i_elvflg	i4b(8,40)	-
i_rng_UQF	i2b(40)	-	i_rng_UQF	i4b(16,40)	-
i_spare49	i1b(10)	-	-	-	-
i_timecorflg	i2b	-	l_timecorflg	l4b(16)	-
i_APID_AvFlg	i1b(8)	-	i_APID_AvFlg	i4b(32)	-
i_AttFlg2	i1b(20)	-	i_padUseFlg	i4b(40)	-
			i_calcPadFlg	i4b(40)	-
			i_LPaproflg	i4b(40)	-
i_spare5	i1b	-	-	-	-
i_FrameQF	i1b	-	i_altFrmFlg	i4b(4)	-
i_OrbFlg	i1b(2)	-	i_podFlg	i4b(6)	-
i_rngCorrFlg	i1b(2)	-	i_rngCorrFlg	i4b(7)	-
i_CorrStatFlg	i1b(2)	-	i_CorrStatFlg	i4b(3)	-
i_spare15	i1b(8)	-	-	-	-
i_AttFlg1	i2b	-	i_AttFlg	i4b(8)	-
i_spare6	i1b(2)	-	-	-	-
i_spare44	i1b(120)	-	-	-	-
i_satNdx	i1b(40)	ns	i_satNdx	i4b(40)	ns
i_satElevCorr	i2b(40)	10 ⁻³ m	d_satElevCorr	r8b(40)	m
i_satCorrFlg	i1b(40)	-	i_satCorrFlg	i4b(40)	-
i_satNrgCorr	i2b(40)	10 ⁻¹⁷ J	d_satNrgCorr	r8b(40)	J
i_spare13	i2b(40)	-	-	-	-
i_gval_rcv	i2b(40)	counts	i_gval_rcv	i4b(40)	cnt
i_RecNrgAll	i2b(40)	10 ⁻¹⁷ J	d_RecNrgAll	r8b(40)	J
i_FRir_cldtop	i2b(40)	10m	d_FRir_cldtop	r8b(40)	m
i_FRir_qaFlag	i1b(40)	-	i_FRir_qaFlag	i4b(40)	-
i_atm_char_flag	i2b	-	i_atm_char_flag	i2b	-
i_atm_char_conf	i2b	-	i_atm_char_conf	i2b	-
i_spare48	i1b(36)	-	-	-	-
i_FRir_intsig	i2b(40)	10 ⁻⁷ /(m-sr)	d_FRir_intsig	r8b(40)	1/(m-sr)
i_spare14	i1b(120)	-	-	-	-
i_Surface_temp	i2b	10 ⁻² degC	d_Surface_temp	r8b	degC
i_Surface_pres	i2b	10 ⁻¹ hPa	d_Surface_pres	r8b	hPa
i_Surface_relh	i2b	10 ⁻² %	d_Surface_relh	r8b	%
i_maxRecAmp	i2b(40)	10 ⁻⁴ v	d_maxRecAmp	r8b(40)	v
i_sDevNsOb1	i2b(40)	10 ⁻⁴ v	d_sDevNsOb1	r8b(40)	v
i_spare8	i1b(2)	-	-	-	-
i_isRngOff	i4b(40)	10 ⁻³ m	d_isRngOff	r8b(40)	m
i_pctSAT	i1b(40)	%	d_pctSAT	r8b(40)	%
i_TxNrg	i2b(40)	10 ⁻⁵ J	d_TxNrg	r8b(40)	J

i_eqElv	i2b(2)	10^{-3}m	d_eqElv	r8b(2)	m
i_spare7	i1b(120)	-	-	-	-

APPENDIX 4.15, REL 33 OCEAN ELEVATION

i4b = four byte integer c1 = one byte character
 i2b = two byte integer r8b = eight byte real (double precision)
 i1b = one byte integer l4b = four byte logical

GLA15_prod_type			GLA15_alg_type		
i_rec_ndx	i4b	-	i_rec_ndx	i4b	-
i_UTCTime	i4b(2)	sec, μ sec	d_UTCTime	r8b	sec
i_transtime	i2b	μ sec	d_transtime	r8b	sec
i_spare1	i2b	-	-	-	-
i_deltagpstmcor	i4b	ns	d_deltagpstmcor	r8b	sec
i_dShotTime	i4b(39)	μ sec	d_dShotTime	r8b(39)	sec
i_lat	i4b(40)	μ deg	d_lat	r8b(40)	degN
i_lon	i4b(40)	μ deg	d_lon	r8b(40)	degE
i_elev	i4b(40)	10^{-3} m	d_elev	r8b(40)	m
i_campaign	i1b(2)	-	c_campaign	c1(2)	-
i_spare40	i2b	-	-	-	-
i_cycTrk	i4b	-	i_cycle	i4b	-
			i_track	i4b	-
i_localSolarTime	i4b	10^{-3} sec	d_localSolarTime	r8b	sec
i_spare41	i4b(7)	-	-	-	-
i_deltaEllip	i2b(40)	10^{-3} m	d_deltaEllip	r8b(40)	m
i_beamCoelv	i4b(40)	10^{-3} deg	d_beamCoelv	r8b(40)	deg
i_beamAzimuth	i4b(40)	10^{-3} deg	d_beamAzimuth	r8b(40)	deg
i_d2refTrk	i4b(40)	10^{-3} m	d_d2refTrk	r8b(40)	m
i_SigBegOff	i4b(40)	10^{-3} m	d_SigBegOff	r8b(40)	m
i_spare45	i1b(40)	-	-	-	-
i_spare46	i2b(9,40)	-	-	-	-
i_ElevBiasCorr	i2b(40)	-	d_ElevBiasCorr	r8b(40)	-
i_spare42	i2b(4,40)	-	-	-	-
i_sigmaatt	i2b(40)	-	i_sigmaatt	i2b(40)	-
i_Azimuth	i4b	10^{-3} deg	d_Azimuth	r8b	deg
i_SolAng	i4b	10^{-6} deg	d_SolAng	r8b	deg
i_tpintensity_avg	i4b	counts	d_tpintensity_avg	r8b	cnt
i_tpazimuth_avg	i2b	10^{-1} deg	d_tpazimuth_avg	r8b	deg
i_tpeccentricity_avg	i2b	10^{-3} unitless	d_tpeccentricity_avg	r8b	-
i_tpmajoraxis_avg	i2b	10^{-2} m	d_tpmajoraxis_avg	r8b	m
i_poTide	i2b	10^{-3} m	d_poTide	r8b	m
i_gdHt	i2b(2)	10^{-2} m	d_gdHt	r8b(2)	m
i_erElv	i2b(2)	10^{-3} m	d_erElv	r8b(2)	m
i_spElv	i2b(4)	10^{-3} m	d_spElv	r8b(4)	m
i_ldElv	i2b(4)	10^{-3} m	d_ldElv	r8b(4)	m
i_bathyElv	i4b	10^{-2} m	d_bathyElv	r8b	m
i_wTrop	i2b(2)	10^{-3} m	d_wTrop	r8b(2)	m
i_dTrop	i2b(40)	10^{-3} m	d_dTrop	r8b(40)	m
i_surfType	i1b	-	l_surfType	l4b(4)	-
i_spare3	i1b(3)	-	-	-	-
i_MSS_elv	i4b(40)	10^{-2} m	d_DEM_elv	r8b(40)	m
i_refRng	i4b(40)	10^{-3} m	d_refRng	r8b(40)	m
i_TrshRngOff	i4b(40)	10^{-3} m	d_TrshRngOff	r8b(40)	m
i_ocRngOff	i4b(40)	10^{-3} m	d_ocRngOff	r8b(40)	m
i_SigEndOff	i4b(40)	10^{-3} m	d_SigEndOff	r8b(40)	m
i_cntRngOff	i4b(40)	10^{-3} m	d_cntRngOff	r8b(40)	m
i_reflctUC	i4b(40)	10^{-6} unitless	d_reflctUC	r8b(40)	-
i_reflCor_atm	i4b	10^{-6} unitless	d_reflCor_atm	r8b	-
i_maxSmAmp	i2b(40)	10^{-4} v	d_maxSmAmp	r8b(40)	v

i_ocElv	i2b(40)	10 ⁻³ m	d_ocElv	r8b(40)	m
i_numPk	i1b(40)	-	i_numPk	i4b(40)	-
i_skew2	i2b(40)	10 ⁻² unitless	d_skew2	r8b(40)	-
i_OcRufRMS	i4b	10 ⁻³ m	d_OcRufRMS	r8b	v
i_OcMeanElev	i4b	10 ⁻³ m	d_OcMeanElev	r8b	m
i_lowElev	i4b(40)	10 ⁻³ m	d_lowElev	r8b(40)	m
i_highElev	i4b(40)	10 ⁻³ m	d_highElev	r8b(40)	m
i_OceanVar	i2b(40)	10 ⁻⁵ v	d_OceanVar	r8b(40)	v
i_ElvuseFlg	i1b(5)	-	i_ElvuseFlg	i4b(40)	-
i_atm_avail	i1b	-	i_atm_avail	i4b	-
i_spare16	i1b(4)	-	-	-	-
i_cld1_mswf	i1b	-	i_cld1_mswf	i4b	-
i_MRC_af	i1b	-	i_MRC_af	i4b	-
i_spare9	i1b(40)	-	-	-	-
i_elvflg	i1b(40)	-	i_elvflg	i4b(8,40)	-
i_rng_UQF	i2b(40)	-	i_RngOffQF	i4b(16,40)	-
i_spare49	i1b(10)	-	-	-	-
i_timecorflg	i2b	-	l_timecorflg	l4b(16)	-
i_APID_AvFlg	i1b(8)	-	i_APID_AvFlg	i4b(32)	-
i_AttFlg2	i1b(20)	-	i_padUseFlg	i4b(40)	-
			i_calcPadFlg	i4b(40)	-
			i_LPAProbFlg	i4b(40)	-
i_spare5	i1b	-	-	-	-
i_FrameQF	i1b	-	i_altFrmFlg	i4b(4)	-
i_OrbFlg	i1b(2)	-	i_podFlg	i4b(6)	-
i_rngCorrFlg	i1b(2)	-	i_rngCorrFlg	i4b(7)	-
i_CorrStatFlg	i1b(2)	-	i_corrStatFlg	i4b(3)	-
i_spare15	i1b(8)	-	-	-	-
i_AttFlg1	i2b	-	i_AttFlg	i4b(8)	-
i_spare6	i1b(2)	-	-	-	-
i_satNdx	i1b(40)	ns	i_satNdx	i4b(40)	ns
i_satElevCorr	i2b(40)	10 ⁻³ m	d_satElevCorr	r8b(40)	m
i_satCorrFlg	i1b(40)	-	i_satCorrFlg	i4b(40)	-
i_satNrgCorr	i2b(40)	10 ⁻¹⁷ J	d_satNrgCorr	r8b(40)	J
i_kurt2	i2b(40)	10 ⁻² unitless	d_kurt2	r8b(40)	-
i_gval_rcv	i2b(40)	counts	i_gval_rcv	i4b(40)	cnt
i_RecNrgAll	i2b(40)	10 ⁻¹⁷ J	d_RecNrgAll	r8b(40)	J
i_FRir_cldtop	i2b(40)	10m	d_FRir_cldtop	r8b(40)	m
i_FRir_qaFlag	i1b(40)	-	i_FRir_qaFlag	i4b(40)	-
i_atm_char_flag	i2b	-	i_atm_char_flag	i2b	-
i_atm_char_conf	i2b	-	i_atm_char_conf	i2b	-
i_spare48	i1b(36)	-	-	-	-
i_FRir_intsig	i2b(40)	10 ⁻⁷ /(m-sr)	d_FRir_intsig	r8b(40)	1/(m-sr)
i_spare14	i1b(120)	-	-	-	-
i_Surface_temp	i2b	10 ⁻² degC	d_Surface_temp	r8b	degC
i_Surface_pres	i2b	10 ⁻¹ hPa	d_Surface_pres	r8b	hPa
i_Surface_relh	i2b	10 ⁻² %	d_Surface_relh	r8b	%
i_Surface_wind	i2b	10 ⁻² m/s	d_Surface_wind	r8b	m/s
i_Surface_wdir	i2b	10 ⁻¹ deg	d_Surface_wdir	r8b	deg
i_maxRecAmp	i2b(40)	10 ⁻⁴ v	d_maxRecAmp	r8b(40)	v
i_sDevNsOb1	i2b(40)	10 ⁻⁴ v	d_sDevNsOb1	r8b(40)	v
i_spare4	i1b(160)	-	-	-	-
i_pctSAT	i1b(40)	%	d_pctSAT	r8b(40)	%
i_TxNrg	i2b(40)	10 ⁻⁵ J	d_TxNrg	r8b(40)	J
i_eqElv	i2b(2)	10 ⁻³ m	d_eqElv	r8b(2)	m
i_spare2	i1b(2)	-	-	-	-
i_gASP	i4b	10 ⁻³ Pa	d_gASP	r8b	Pa

i_spare7 ilb(144) - - - -

References

- Abshire, J.B., J.F. McGarry, L. K. Pacini, J.B. Blair, and G.C. Elman (1994) Laser Altimetry Simulator, Version 3.0 User's Guide. NASA Technical Memorandum 104588, NASA/GSFC, Greenbelt, MD, 70 p
- Abshire, J. and X. Sun (1999) Personal communication
- Abshire, J.B. (1995) Personal communication
- Aldred, A., and G. Bonner (1985) Application of Airborne Lasers to Forest Surveys, Canadian Forestry Service, Petawawa National Forestry Centre, Information Report PI-X-51, 62 pp
- Bamber, J.L., and J.P. Muller (1998) Derivation of a global land elevation data set from satellite radar altimeter data for topographic mapping. *J. Geophys. Res.-Atmos.*, Vol. 103, No. D24, 32159-32168
- Bamber, J.L. (1994) Ice sheet altimeter processing scheme. *Int. J. Remote Sensing*, Vol. 15, No. 4, 925-938
- Bamber, J.L., and P. Huybrechts (in press) Geometric boundary conditions for modeling the velocity field of the Antarctic ice sheet. *Annals of Glaciology*, 23
- Bevington, P.R. and D.K. Robinson (1992) *Data Reduction and Error Analysis for the Physical Sciences*, second edition. McGraw-Hill, NY
- Blair, J.B., D.B. Coyle, J.L. Bufton, and D.J. Harding (1994) Optimization of an airborne laser altimeter for remote sensing of vegetation and tree canopies. *Proc. IGARSS'94*, 939-941
- Brenner, A.C., H.V. Frey, and H.J. Zwally (1990) Comparisons between GEOSAT and SEASAT tracking over nonocean surfaces. *Geophys. Res. Lett.*, Vol. 17, No. 10, 1537-1540
- Brenner, A.C., R. Bindshadler, R.H. Thomas, and H.J. Zwally (1983) Slope-induced errors in radar altimetry over continental ice sheets. *J. Geophys. Res.* Vol. 88, 1617-1623
- Brooks, R.L., W.J. Campbell, R.O. Ramseier, H.R. Stanley and H.J. Zwally (1978) Ice sheet topography by satellite altimetry. *Nature*, 274, 539-543
- Brown, G.S. (1977) The average impulse response of a rough surface and its applications. *IEEE Transactions on Antennas and Propagation*, Vol. Ap-25, No. 1, 67-74
- Budd, W.F. (1970) Ice flow over bedrock perturbations. *J. Glaciology*, Vol. 9, No. 55, 29-48
- Budd, W.F., and D.B. Carter (1971) An analysis of the relation between the surface and bedrock profiles of ice caps. *J. Glaciology*, Vol. 10, No. 59, 197-209
- Bufton, J.L., J.B. Garvin, J.F. Cavanaugh, L. Ramosizquierdo, T.D. Clem, and W.B. Krabill (1991) Airborne lidar for profiling of surface topography. *Opt. Eng.*, Vol. 30, No. 1, 72-78
- Bufton, J.L., J.E. Robinson, M.D. Femiano, and F.S. Flatow (1982) Satellite laser altimeter for measurement of ice sheet topography. *IEEE Transactions on Geoscience and Remote Sensing*, GE-20 (4), 544-549

- Bufton, J.L. (1989) Laser altimetry measurements from aircraft and spacecraft. *Proceedings of the IEEE*, 77(3), 463-477
- Carsey, F.D., ed. (1992) *Microwave remote sensing of sea ice*. American Geophysical Union, 462 pages
- Comiso, J.C. (1995) Satellite remote sensing of the Arctic Ocean and adjacent seas. *Arctic Oceanography: Marginal ice zones and continental shelves, Coastal and estuarines studies*, 49, 1-50
- Csathó, B.M. and R.H. Thomas (1995) Determination of sea ice surface roughness from laser altimetry waveform. BPRC Technical Report No. 95-03, Byrd Polar Research Center, The Ohio State University, Columbus, Ohio, 45 pages
- Davis, C.H., and H.J. Zwally (1993) Geographic and seasonal variations in the surface properties of the ice sheets by satellite-radar altimetry. *J. Glaciology*, Vol. 39, No. 133, 687-697
- Davis, C.H., C.A Kluever, and B.J. Haines (1998) Elevation Change of the Southern Greenland Ice Sheet. *Science*, Vol. 279, pp. 2086-2088
- Doumani, G.A., 1967. Surface structures in snow. H. Oura, ed., *Physics of Snow and Ice: Sapporo Conference, 1966*, Inst. of Low Temp. Science, U. Hokkaido, 1119-1136.
- Duda, D. and J. Spinhirne, Personal Communication
- Drewry, D.J., N.F. McIntyre, and P. Cooper (1985) The Antarctic ice sheet: a surface model for satellite altimeter studies. Woldenberg, H. J., ed. *Models in Geomorphology*. Allen and Unwin, Boston, 1-23
- Endo, Y., and K. Fujiwara (1973) Characteristics of the snow cover in East Antarctica along the route of the JARE South Pole traverse and factors controlling such characteristics. *Japanese Antarctic Research Expedition Scientific Reports*, C, 4-11
- Fifield, R. (1987) *International Research in the Antarctic*. Oxford University Press, New York, 146 p
- Frey, H. and A.C. Brenner (1990) Australian topography from SEASAT overland altimetry. *Geophys. Res. Lett.*, Vol. 17, No. 10, 1533-1536
- Furukawa, T., O. Watanabe, K. Seko, and Y. Fujii (1992) Distribution of surface conditions of ice sheet in Enderby Land and East Queen Maud Land, East Antarctica. *Proceeding of NIPR Symposium on Polar Meteorology and Glaciology*, Vol. 5, 140-144
- Gardner, C. S. (1982) Target signatures for laser altimeters: An analysis. *Applied Optics*, 21(3), 448-453
- Gardner, C. S. (1992) Ranging performance of satellite laser altimeters. *IEEE Transactions on Geoscience and Remote Sensing*, 30(5), 1061-1072
- Garvin, J., J. Bufton, J. Blair, D. Harding, S. Luthcke, J. Frawley, and D. Rowlands (1998) Observations of the Earth's topography from the Shuttle Laser Altimeter(SLA): laser-pulse echo-recovery measurements of terrestrial surfaces. *Phys. Chem. Earth*, Vol. 23, No. 9-10, 1053-1068
- Grenfell, T.C., and D.K. Perovich (1984) Spectral albedos of sea ice and incident solar irradiance in the southern Beaufort Sea. *J. Geophys. Res.*, 89(C3), 3,573-3,580

Harding, D.J., J.L. Bufton, and J.J. Frawley (1994) Satellite laser altimetry of terrestrial topography: vertical accuracy as a function of surface slope, roughness, and cloud cover. *IEEE Transactions on Geoscience and Remote Sensing*, 32(2), 329-339

Harding, D., C. Carabajal, and W. Fong (1998) Suggested ICESat Waveform Processing Procedures Based on SLA Methodologies. Input to Waveform ATBD Working Group

Harding, D.J., J.B. Blair, J.B. Garvin, and W.T. Lawrence (1994) Laser altimetry waveform measurement of vegetation canopy structure. *Proc. IGARSS'94*, 1251-1253

Harding, D.J., (1998) Airborne lidar observations of canopy structure at the BOREAS tower flux sites. *Proc. IGARSS '98*, 1550-1552

Herzfeld, U. (1996) Personal communication

Hofton, M.A., J.B. Blair, J.B. Minster, J.R. Ridgway, N.P. Williams, J.L. Bufton, D.L. Rabine (in press) An airborne scanning laser altimetry survey of Long Valley, California. *Int. J. Rem. Sens.*

Hofton, M.A., J.B. Minster, J.R. Ridgway, N.P. Williams, J.B. Blair, D.L. Rabine, J.L. Bufton (in press) Using Airborne

Laser Altimetry to Detect Topographic Change at Long Valley Caldera, California. *Remote*

Sensing of Active Volcanism, ed. P. Mougini Mark, AGU Monograph Series

Hutter, K., F. Legerer, and U. Spring (1981) First-order stresses and deformations in glaciers and ice sheets. *J. Glaciology*, Vol. 27, No. 96, 227-270

Koblinsky, C.J., R.T. Clarke, A.C. Brenner, and H. Frey, (1993) Measurement of river level variations with satellite altimetry. *Water Resour. Res.*, Vol. 29, No. 6, 1839-1848

Kotlyakov, V.M. (1966) The snow cover of the Antarctic and its role in the present-day glaciation of the continent. *Israel Program for Scientific Translation, Jerusalem*, 256 p

Krabill, W., R. Thomas, C. Martin, R. Swift, and E. Frederick (1995) Accuracy of airborne laser altimetry over the Greenland ice sheet, *Int. J. Remote Sensing*, 16, 1211-1222.

Krabill, W., W. Abdalati, E. Frederick, S. Manizade, C. Martin, J. Sonntag, R. Swift, R. Thomas, W. Wright, and J. Yungel (2000) Greenland ice sheet: high-elevation balance and peripheral thinning, *Science*, 289, 428-429.

Laxon, S (1998) Personal communication

Ledroit, M., F. Rémy, and J.F. Minster (1992) Observation of the Antarctic ice sheet by Seasat scatterometer: relation to katabatic wind intensity and direction. *J. Glaciology*, Vol. 39, No. 132, 385-396

Lefsky, M.J. (1997) Application of Lidar Remote Sensing to the Estimation of Forest Canopy Structure. *Univ. of Virginia, Ph.D. Dissertation*, 185 pp

Lefsky, M.A, D.J. Harding, W.B. Cohen, G.G. Parker, and H.H. Shugart (1999) Surface lidar remote sensing of basal area and biomass in deciduous forests of Eastern Maryland, USA. *Rem. Sens. Environ.*, Vol. 67, 83-98

- Lefsky, A., W.B. Cohen, S.A. Acker, T.A. Spies, G.G. Parker, and D.J. Harding (1998) Lidar remote sensing of forest canopy structure and related biophysical parameters at the H.J. Andrews experimental forest, Oregon, USA. Proc. IGARSS'98, 1252-1254
- Martin, T.V., A.C. Brenner, H.J. Zwally, and R.A. Bindschadler (1983) Analysis and retracking of continental ice sheet radar altimeter waveforms. *J. Geophys. Res.*, Vol. 88, 1608-1616
- McGarry, J.F., J.B. Abshire, X. Sun, J. Saba, A. Brenner, and D. Yi, GLAS Flight Science Data Selection Algorithms For The Altimeter (1064nm) Version 4.03, in process
- McIntyre, N. F. (1986) Antarctic ice-sheet topography and surface-bedrock relationships. *Annals of Glaciology*, Vol. 8, 124-128
- Means, J.E., S.A. Acker, D.J. Harding, J.B. Blair, M.A. Lefsky, W.B. Cohen, M.E. Harmon, and W.A. McKee, W.A. (in press) Use of a large-footprint scanning airborne lidar to estimate forest stand characteristics in the western Cascades of Oregon. *Rem. Sens. Environ.* Vol. 67, 298-308
- Menke W. (1989) *Geophysical Data Analysis: Discrete Inverse Theory*, revised edition. International Geophysical Series, Vol. 45, Academic Press, NY
- Nilsson, M. (1996) Estimation of tree heights and stand volume using an airborne lidar system. *Remote Sens. Environ.* Vol. 56, 1-7
- Nolin, A. (1996) Personal communication
- Ogilvy, J. A. (1991) *Theory of Wave Scattering from Random Rough Surfaces*. Adam Hilger, Bristol, England, 277 p
- Partington, K. C., J. K. Ridley, C. G. Rapley, and H. J. Zwally (1989) Observations of the surface properties of the ice sheets by satellite radar altimetry. *J. Glaciology*, Vol. 35, No. 120, 267-275
- Paterson, W. S. B. (1994) *The Physics of Glaciers*. Permagon, Tarrytown, New York, 480 p
- Peacock, N. R., S. W. Laxon, W. Maslowski, D. P. Winebrenner, and R. J. Arthern (1998) Geophysical signatures from precise altimetric height measurements in the Arctic Ocean
- Perovich, D. K. (1996) The optical properties of sea ice. CRREL Monograph 96-1, U.S. Army Corps of Engineers CRREL, Hanover, NH, 24 p
- Press, W.H., B.P. Flannery, S.A. Teuloksky, and W.T. Vettering (1986) *Numerical Recipes*. Cambridge U Press
- Reeh, N., S. J. Johnsen, and D. Dahl-Jensen (1985) Dating of the Dye 3 deep ice core by flow model calculations. C. C. Langway, Jr., H. Oeschger, and W. Dangaard, eds. *Greenland ice core, geophysics, geochemistry, and the environment*, Am. Geophys. Union Geophys. Monograph 33, 57-65
- Rémy, F., P. Mazzega, S Houry, C. Brossier, and J. F. Minster (1989) Mapping of the topography of continental ice by inversion of satellite-altimeter data. *J. Glaciology*, Vol. 35, 38-97
- Rémy, F., C. Brossier, and J. F. Minster (1990) Intensity of satellite radar-altimeter return power over continental ice: a potential measurement of katabatic wind intensity. *J. Glaciology*, Vol. 36, No. 123, 133-142

- Rémy, F., and J.F. Minster (1991) A comparison between active and passive microwave measurements of the Antarctic ice sheet and their association with the surface katabatic winds. *J. Glaciology*, Vol. 37, No. 125, 3-10
- Rémy, F., M. Ledroit, and J.F. Minster (1992) Katabatic wind intensity and direction over Antarctica derived from scatterometer data. *Geophys. Res. Letters*, Vol. 19, 1021-1024
- Robin, G. de Q. (1967) Surface topography of ice sheets. *Nature*, Vol. 189, 1029-1032
- Seko, K., T. Furukawa, and O. Watanabe (1991) The surface condition on the Antarctic ice sheet. G. Weller, ed., *International Conference on the Pole of the Polar Regions in Global Change*, Vol. 1, U. Alaska - Fairbanks, 238-242
- Spinhirne, J (1996) Personal Communication
- Stremler, F. G. (1990) *Introduction to Communication Systems*. Addison-Wesley Publishing Company, Reading, Massachusetts, 757p. East Antarctic ice sheet. *Annals of Glaciology*, 20, 137-142
- Sun X. (1996) unpublished, presented at GLAS Science Team Meeting
- Thomas, R.H., W. Krabill, S. Manizade, R. Swift, and A. Brenner (1994) Comparison of Radar Altimetry Data over Greenland with Surface Topography Derived from Airborne Laser Altimetry. *Proceedings Second ERS-1 Symposium*, 11-14 Oct 1993, ESA SP-361
- Tsai, B. M., and C. S. Gardner (1982) Remote sensing of sea state using laser altimeters. *Applied Optics*, 21(21), 3932-3940
- Tucker, W. B., D. K. Perovich, A. J. Gow, W. F. Weeks, and M. R. Drinkwater (1992) Physical properties of sea ice relevant to remote sensing. F. D. Carsey, ed. *Microwave remote sensing of sea ice*, American Geophysical Union, 9-27
- Wadhams, P., W. B. Tucker III, W. B. Krabill, R. N. Swift, J.C. Comiso, and N. R. Davis (1992) Relationship between sea-ice freeboard and draft in the Arctic basin, and implications for ice-sheet monitoring. *J. Geophys. Res.*, 97(C12), 20,325-20,334
- Watanabe, O. (1978) Distribution of surface features of snow cover in Mizuho Plateau. *Memoirs of National Institute of Polar Research (Japan)*, Special Issue #7, 44-62
- Whillans, I. M., and S. J. Johnsen (1983) Longitudinal variations in glacial flow: theory and test using data from the Byrd Station strain network. *J. Glaciology*, Vol. 29, No 101, 78-97
- Wingham, D.J., A.J. Ridout, R. Scharroo, R.J. Arthern, and C.K. Shum (1998) Antarctic Elevation Change from 1992-1996. *Science*, Vol 282 456-458
- Yi, D., and C. R. Bentley, (1994). Analysis of satellite radar-altimeter return wave forms over the East Antarctic ice sheet. *Annals of Glaciology*, 20, 137-142
- Zuber, M.T., D.E. Smith, S.C. Solomon, J.B. Abshire, R.S. Afzal, O. Aharonson, K. Fishbaugh, P.G. Ford, H.V. Frey, J.B. Garvin, J.W. Head, A.B. Ivanov, C.L. Johnson, D.O. Muhleman, G.A. Neumann, G.H. Pettengill, R.J. Phillips. X. Sun, H.J. Zwally, W.B. Banerdt, T.C. Duxbury (1998) Observations of

the North Polar Region of Mars from the Mars Orbiter Laser Altimeter. *Science*, Vol. 282, pp. 2053-2060

Zuber, M.T., D.E. Smith, S.C. Solomon, D.O. Muhlemen, J.W. Head, J.B. Garvin, J.B. Abshire, J.L. Bufton (1992) The Mars Observer laser altimeter investigation. *J. Geophys. Res.*, Vol 97, No. E5, 7781-7797

Zwally, H. J., R.A. Bindschadler, A.C. Brenner, T.V. Martin, and R.H. Thomas (1983) Surface elevation contours of Greenland and Antarctic Ice sheets. *J Geophysics, Res.*, Feb 28

Zwally, H.J., A.C. Brenner, J.A. Major, R.A. Bindschadler, and J.G. Marsh (1989) Growth of Greenland Ice Sheet: Measurement. *Science*, Vol. 246, pp/1587-1589

Zwally, H.J., A.C. Brenner, J.A. Major, T.V. Martin, and R.A. Bindschadler (1990) Satellite Radar Altimetry Over Ice. Volume 1, NASA Ref Pub 1233, Vol 1

Zwally, H.J., A.C. Brenner, J.P. DiMarzio, and T. Seiss (1994) Ice Sheet Topography from Retracked ERS-1 Altimetry. *Proceedings Second ERS-1 Symposium*, 11-14 Oct 1993, ESA SP-361